The Kubas Interaction in Transition Metal Based Hydrogen Storage Materials

Submitted by:

Claire Victoria Jane Skipper

For the degree of:

Doctor of Philosophy

Supervisor:

Professor Nikolas Kaltsoyannis

University College London, 2012

<u>Declaration</u>

I Claire Victoria Jane Skipper confirm that the work presented in this thesis is my own. Where information has been derived from other sources, I confirm that this has been indicated in the thesis.

Abstract

This PhD is a computational study of the hydrogen storage materials made by the Antonelli group based in Glamorgan using Density Functional Theory (DFT) and the Quantum Theory of Atoms In Molecules (QTAIM). These materials are either silica based or hydrazine linked with transition metal binding sites to which, it is thought, the hydrogen binds through the Kubas interaction. All of the materials display rising hydrogen binding enthalpies with increasing hydrogen coverage. The first QTAIM study of the Kubas interaction was performed on molecules, to which it is agreed the hydrogen binds through the Kubas interaction, in order to benchmark this technique before applying it to the studied materials.

The binding sites were modelled as fragments representing the active sites in the extended structures. Evidence has been found for the hydrogen binding through the Kubas interaction and the results were benchmarked against the available experimental data. The transition metals of the binding sites and their associated ancillary ligands were altered in order to probe the possible effect that this could have on the experimental system. It was found that poor π-acceptor ancillary ligands increase the strength of the interaction between the metal and the hydrogen and that changing the metal from Ti to V to Cr to Mn reduces the number of the H_2 molecules that can be bound. Cr and Mn are considered to be poor choices for incorporation as binding sites in hydrogen storage materials.

Explanations for the rising hydrogen binding enthalpies with increasing hydrogen coverage have been presented for the silica based and hydrazine linked materials based on local perturbation of the molecular orbitals and metal to metal cooperativity respectively.

The study was extended further to include hydrazine linked materials based on Ni(II), Cu(I) and Cu(II) metal centres to probe their potential as hydrogen storage materials.

Acknowledgements

I would most of all like to thank Nik Kaltsoyannis who has given me the stability and confidence to undertake a PhD. He has patiently read my initial written work and has provided feedback to nudge me towards expressing myself more eloquently. The Antonelli group in Glamorgan were also very important for without their hydrogen storage materials there would not be any PhD work.

I would also like to thank G19, my basement home from home, and all of its occupants past and present. Special thanks go to Amy for teaching me how to copy a large amount of text using vi, Rosie and Laura for their excellent examples of 'what to do', Leif for his patience with my stupid questions and for teaching my how to do Ziegler-Rauk calculations, Krishna for being a true friend in the office to whom I feel I could tell almost anything and Ian for our surreal conversations and for all of his computing trickery especially 'tablecps'.

Out of G19 I would like to thank the whole of the department and the Chemical Physical Society for taking me as I am and making me feel welcome. Special thanks to Charles, Dave and Jorg for computing support especially the efforts to set up conference calls, remove viruses from my computer and put up screens for the Christmas quiz and Mary-Lou, Liz and Wendy for making things run smoothly on the office side and for the extra work. Thank you also to Helen Fielding for telling me, 'Write up as you go along.'

In the wider world I would like to thank my parents for their unconditional support in everything that I do and for Nanny Bet, Bob, Jack, Rachael and Chris for being there when I need them.

I will always be grateful to the graduate school and CE38 for funding.

Contents

5

List of Figures

7

9

11

14

Introduction

The hydrogen economy where hydrogen, with a high energy density (142 M Jkg^{-1}) compared to liquid hydrocarbons (47 M Jkg^{-1}), is the energy carrier has been the dream of many for some time.[1] The Third Industrial Revolution (TIR), formulated by Jeremy Rifkin in the mid-1990s and taught by him at the University of Pennsylvania in the Wharton School's Advanced Management Program, became mainstream in 2007 when the European Parliament issued a declaration proclaiming the TIR the long-term economic vision and road-map for Europe and is quickly spreading to other countries.[2] It is predicted that the outcome of this revolution will be that every building will generate its own renewable electricity for its own use with the excess energy shared on an 'Energy Internet.'[2] The surplus energy will be stored in batteries and used to power photovoltaic cells that split water to produce hydrogen that may be stored and then used in Proton Exchange Membrane Fuel Cells (PEMFCs) to produce electricity to either remove the intermittency of renewable energies (the wind does not always blow and the sun does not always shine) or to power vehicles. The fuel cell combines the hydrogen with oxygen to form water, which is released, and thus completes this short and non-polluting cycle. The ability to store electricity produced from renewable resources long term as hydrogen, increases the practicality of using renewable resources and, therefore, increases their penetration,[3] links the production of electricity and fuel for transport[3] and could increase the energy independence of oil consuming countries.[4] The use of the hydrogen in vehicles has added benefits as PEMFCs only produce non-polluting water and in comparison to hydrocarbons they do not produce any nitrogen dioxide and so the local air pollution in urban areas would be reduced.[4] The use of hydrogen in vehicles also has benefits over batteries as generally shorter recharge times and longer vehicle ranges are achievable. [4] This hydrogen age will bring to an end the carbon age whose deathbed looms before us.

The increasing demand for depleting fossil fuels is raising energy prices that is in turn causing economic stagnation and rising unemployment.[2] This increase in demand is being caused by the burgeoning world population with the

16

simultaneous development of the emerging economies. In the 20th century the population quadrupled and the energy demand went up 16 times.[5] In 2004 there were 1 billion new consumers compared to the previous year who had a purchasing power parity to match that of the consumers in the U.S.A.[5] These new consumers eat more meat and purchase more vehicles. In China, for example, there were 1.1 million cars in 1990 which had increased to 6 million in 2000[6] and now there are now 114 million automobiles.[7] The number is still increasing as there was a 3.67 % increase from last year.[7] These extra vehicles burn more gasoline and increase the rate at which our oil reserves are depleted. Currently for every billion barrels of new oil discovered we are consuming 4 billion barrels.[5] Obviously, this consumption is not sustainable and attempts to increase production of oil be using new technologies to extract it from hard to obtain areas and sustain the production from each site for longer will not have an impact on the amount of oil available and additional energy will be required for the extraction.[5] Whilst burning more gasoline the extra vehicles produce more carbon dioxide such that global carbon dioxide emissions from motor vehicles, of which cars make up 74 %, increased from 1990-1997 by 26 % at a rate 4 times greater than CO_2 emissions overall.[6] The increasing CO_2 emissions contribute to the rising carbon dioxide levels in the atmosphere which are thought to have passed 400 ppm, having reached 394.01 ppm in April 2012.[8] Carbon dioxide levels higher than this were last seen about 25 million years ago.[9] Carbon dioxide is a well-known greenhouse gas that is linked to the increase in global average temperatures. The long-term global average temperature since records began in 1850 is 14 ºC and 9 of the last 10 years have been ranked within the 12 hottest years on record. 2011 was ranked as the 11th hottest year with a temperature of 0.44 ºC above average.[10] This increase in temperature is thought to be contributing to climate change and the increase in severity and frequency of extreme weather phenomena.[11] The surface temperature of the Atlantic Ocean today is higher than it has been for at least a millennium making the tropical storms and hurricanes stronger than ever.[11] The higher mean surface temperature is also contributing to the melting of the arctic ice and increasing sea levels.[5]

The dawn of the hydrogen age will bring an end to the dependence on fossil fuels and the continued pollution of our planet and the preparation for it will reduce unemployment due to the need to build its infrastructure. However, this dawn is as yet a dim haze on the horizon as much of the world's population continues to be in a state of denial over the impending ecological disaster and the current economic model, based on short term low risk profit, makes financing infrastructure difficult.[2] Although available in many areas the current hydrogen based technologies are not economically viable compared to the traditional technologies based on fossil fuels or even if comparable industry is unwilling to take the risk of new technology.

Small sparks of hope have appeared that could stop us sleep walking into a mass extinction only where government subsidy has played a part to encourage uptake. For example, the U.S.A. has a strong market in fuel cells particularly for fork lift trucks due to government financial incentives such as the Emergency Economic Stabilisation Act of 2008 which gave a tax credit of $3,000/kW of the fuel cell nameplate capacity.[12] This has allowed the number of fuel cell powered forklifts in the U.S.A to increase to about 3,000,[13] for them to now be economically viable and has meant that Ballard, the main producer of these forklifts, is receiving repeat sales from big corporations such as Walmart.[14] These repeat sales come from the reduction in the cost of the fuel cells to $49/kW due to the high volume production[15] and due to the benefits of a 1 − 3 min charge time and constant power over batteries that require an 8h recharge and lose power over time.[16] Ballard has expanded sales into Canada where there are not government subsidies and has plans to expand into Europe.[14] The production of the hydrogen used in these fuel cells, however, has remained stubbornly in the past with 95% produced by steam reforming of methane, (1), derived from fossil fuels, via syn gas, which is not renewable[17] with only 4 % formed by the electrolysis of water.[4] This may be due to a lack of government subsidy for cleaner alternatives.

$$CH_4 + H_2O \rightarrow 3H_2 + CO$$
$$\underline{CO + H_2O \rightarrow H_2 + CO_2}$$
$$CH_4 + 2H_2O \rightarrow 4H_2 + CO_2 \qquad\qquad (1)$$
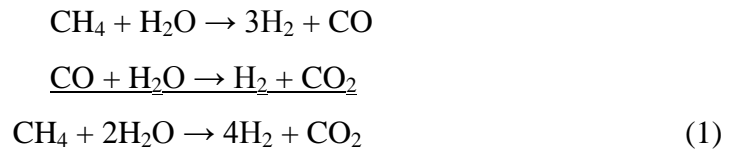
Most of the hydrogen produced is not used in fuel cells but is an important feedstock in many vital chemical processes. Of the 50 million tons of hydrogen that is formed each year 51 % is used to make ammonia via the Haber process by combining it with nitrogen, 35% is used in the refining of petroleum to form hydrogenated hydrocarbons such as cyclohexane and 8% is used in the formation of methanol from carbon monoxide.[4] Ammonia is an important component of fertilisers and the hydrogenation products of petroleum are used in the formation of plastics and by the pharmaceutical industry.[18]

The use and production of fuel cell powered cars has come up against a 'chicken and egg' problem as it is not economical to build hydrogen refuelling stations, unless there are hydrogen powered cars to fill up, and customers will not buy hydrogen powered vehicles, unless they can refuel them. However, the motor industry has set itself a target of 2015 for commercialising hydrogen powered cars and a few countries have taken this as a deadline for providing a rudimentary hydrogen refuelling network. For example, in Japan where Toyota is leading the way with hydrogen powered vehicles, they plan to have 100 hydrogen refuelling stations by 2015.[19]

The on board storage of the hydrogen still remains a problem as hydrogen is a low density gas and 4 kg of hydrogen, with a volume of 45 m^3 at room temperature and pressure, is required for a fuel cell powered car to travel 400 km.[1] The hydrogen has a lower energy density by volume than liquid hydrocarbons such that 1 litre of liquid hydrogen contains 71 g of hydrogen but 1 litre of gasoline contains 116 g of hydrogen. This means that heavier larger tanks of hydrogen are required to provide the same amount of energy and higher pressures are required for smaller tanks. The smaller tanks are still heavy, however, due to the added material required to accommodate the higher

pressure.[20] Currently Toyota, in the same way as most manufacturers, has implemented high pressure storage tanks of 70 MPa[21] but tank pressures up to 80 MPa are possible.[20] Hydrogen may also be stored as a liquid at 21 K but this results in a high energy loss to produce and maintain the cryogenic temperature or in the loss of hydrogen through boil off.[20] BMW, though, is implementing cryogenic storage, with cold gaseous hydrogen to reduce the pressure required to store the same amount at room temperature. This also reduces that lost through boil off and the energy required to cool the hydrogen vs storing it as a liquid.[22] Storage at 0.1 MPa and room temperature would be the ideal[21] and there has been a search for a hydrogen storage material that could be incorporated into pressurised tanks such that more hydrogen is stored at a given pressure. Materials such as this would reduce the possible hazard of the high pressure and could be more energy efficient than liquid or high pressure storage.[20] The U.S.A.'s Department of Energy has targets for any storage system, including any material and the tank, to be met by 2015 which include a gravimetric storage density of 5.5 %wt, a volumetric storage capacity of 40 gL^{-1} and a 3.3 minute refuelling time for a 5 kg tank.[23] This means that any storage material has to have a hydrogen storage capacity greater than 5.5 %wt to comply. However, a hydrogen storage material has not yet been delivered that is more economically viable than a high pressure tank. Though Toyota would welcome a storage material to remove the potentially dangerous high pressure tanks, they have invested in this system such that any storage material would have to be a significant improvement especially in terms of its cost and safety, although it would not have to meet all of the DOE targets, in order for them to make a change.[21]

Many types of storage material have been considered, which interact with the hydrogen in different ways with different hydrogen binding enthalpies. It has been calculated that to achieve the storage requirements at room temperature a storage material hydrogen binding enthalpy of 20 – 40 kJmol^{-1} is required.[24, 25] Materials that physisorb the hydrogen have enthalpies that are too low (ca. 3 – 4 kJmol^{-1})[26] where the hydrogen is bound by van der Waals interactions. These materials are typically carbon based, metal organic frameworks (MOFs) or zeolites. Although they can easily adsorb and desorb reasonable amounts of

hydrogen at 77 K (9.05 wt% for NU-100)[27], due to their low kinetic barriers, because of their low binding enthalpies they have low storage capacities at room temperature.[28] By contrast, materials that chemisorb the hydrogen and bind to individual hydrogen atoms through strong covalent bonds have enthalpies that are too high (ca. +70 kJmol^{-1}).[29, 30] These are typically metal hydrides and although they have high hydrogen storage capacities at room temperature they often exhibit slow kinetics for hydrogen adsorption and removal and, due to their high binding enthalpies, evolve a great deal of heat upon hydrogen adsorption.[31] Between these two extremes there are fewer materials and the nature of the interaction of the material with the hydrogen is unclear.

In order to reach the desired enthalpy it has been suggested that transition metals should be incorporated into large surface area materials for hydrogen to interact with through the Kubas interaction or through hydrogen spillover. Hydrogen spillover is where the metal catalyses the dissociation of the hydrogen and the hydrogen atoms then migrate, usually through diffusion, to bind with the rest of the material.[32] In order for this to be reversible the metal needs to catalyse the recombination of the hydrogen as well.

The Kubas interaction[33, 34] is consistent with a lengthening of the H–H bond without breakage and involves σ-donation from the filled H–H σ-bonding orbital into an empty d orbital of a metal, and simultaneous π-back-donation from a filled metal d orbital into the vacant σ* anti-bonding orbital of the H_2 molecule (Figure 1). This is similar to the synergic bonding described by the Dewar-Chatt-Duncanson model for the interaction of, for example, CO with transition metals.[35, 36]

σ-donation   π-back-donation
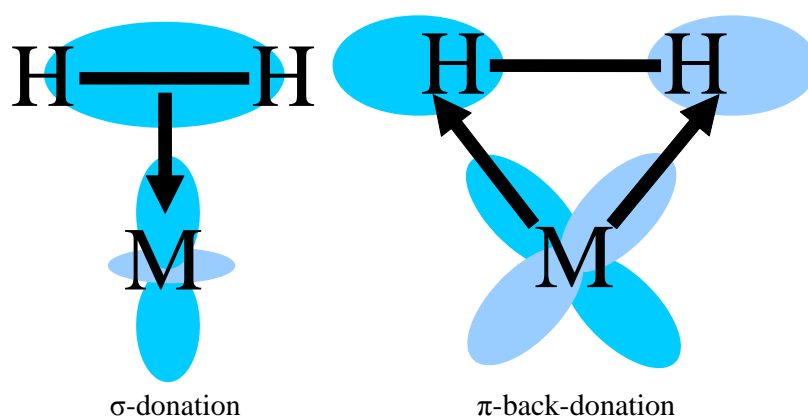
Figure 1: Schematic representation of the two synergic components of the Kubas interaction.

This type of interaction between a H_2 molecule and a metal centre was first identified by Greg Kubas in 1983 in $W(CO)_3(P^iPr_3)_2(\eta^2\text{-}H_2)$ (Figure 2).[37, 38] The H–H bond is stretched to about 0.84 Å,[39] from the H_2 free value of 0.74 Å. Before then it was thought that dihydrogen could form only as an intermediate before the formation of a dihydride.[33] Although the σ-donation is generally the dominant interaction there needs to be a balance between σ-donation and π-back-donation to coordinate the H_2. The π-back-donation orientates the H_2 side on to the metals and the extent of π-back-donation determines whether the H_2 will form a hydride. There is a continuum of coordinated H–H bond lengths from the 0.74 Å of free hydrogen up to 1.6 Å with lengths above this considered by Kubas to be two hydride ligands. He considers only 0.8 – 0.9 Å complexes to be 'true' Kubas and those with bond lengths of 1 – 1.6 Å to have elongated H–H bonds. The latter were discovered only in about 1990.[33] Presumably those H_2 molecules with bond lengths of 0.9 – 1.0 Å are at the transition between the two on the continuum of H–H bond lengths.
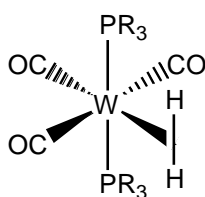
Figure 2: Structural representation of $W(CO)_3(P^iPr_3)_2(\eta^2\text{-}H_2)$.

π-back-donation may be decreased by having ancillary ligands about the metal that are electron-withdrawing, especially the ancillary ligand trans to the H_2, and metals that are less electron rich. However, H_2 can still bind strongly to electron deficient metals as well as to electron-rich metals as a greater amount of σ-donation can offset the decrease in the amount of π-back-donation. The amount of σ-donation versus π-back-donation is affected much more by the ancillary ligands about the metal rather than the metal itself.[33] The sum of these bonding components for a given system tends to remain reasonably constant however, as a loss in one of the components is compensated for by an increase in the other.[33]

Theoretical study of the metal to hydrogen ($M\text{–}H_2$) interaction occurred at about the same time as the experimental study. Bagatur'yants was the first to publish quantum-mechanical calculations with a stable $M\text{–}H_2$ interaction in 1980 and $W(CO)_3(P^iPr_3)_2(\eta^2\text{-}H_2)$ was the first Kubas complex studied theoretically.[33] Many types of calculation method have been used to describe the $M\text{–}H_2$ interaction and density functional theory (DFT) has emerged as a leading methodology.[33] Theoretical analysis remains challenging as the $M\text{–}H_2$ interaction is weak and the potential energy surface (PES) of the stretch of the H–H bond is extremely flat.[33]

Potential hydrogen storage materials with metals that are thought to bind hydrogen through the Kubas interaction have been investigated. Much of the research is computational, probably due to the difficulty in synthesising materials with metals that are not fully coordinated, but there have been some experimental studies of metal organic frameworks (MOFs)[40, 41], zeolites[42] and of molecules

23

representing the binding sites in MOFs[43] and graphene.[44] The computational studies have included some that are based on or model experimental systems[45-47] but much of the computational work is only loosely based on real systems or is entirely theoretical.[48-66]

The occurrence of the Kubas interaction experimentally is suggested by a reduction in the H–H stretching frequency observed by Raman spectroscopy. Definitive evidence for the Kubas interaction is given, however, by observing the H_2 molecule's rotational transitions in inelastic neutron scattering experiments which are not seen in hydrides. These measure the barrier to H_2 rotation which is present due to the H_2 favouring a particular orientation that aligns it with certain favourable d orbitals on the metal for π-back-donation.[33]

Proving that the H_2 is binding to the metals of the experimental solids through the Kubas interaction is difficult but Dincă, Long and co-workers[40] believe that it is in their MOF with exposed Mn^{2+} sites due to the high maximum enthalpy of adsorption of 10.1 kJmol^{-1} when compared to that of physisorption materials (c.a. 3 – 4 kJmol^{-1})[26] and because the neutron diffraction data demonstrates that the H_2 binds most strongly to the Mn^{2+}.[40] Similarly Vitillo[41] and co-workers used infra-red (IR) spectroscopy to show that the H_2 was binding to the exposed Ni^{2+} sites in CPO-27-Ni, and feel that this is the cause of the high initial adsorption enthalpy of 13.5 kJmol^{-1}. They also compared it to MOF-5 with unexposed metal sites, to which the hydrogen did not bind, which shows the importance of including metals that are not fully coordinated to allow them to take part in Kubas type interactions. Kaye and Long[43] also showed, indirectly through IR spectroscopy, that H_2 was binding to the Cr in the MOF $Zn_4O(BDC)_3$ (BDC^{2-}=1,4-benzenedicarboxylate) after it was converted to $Zn_4O[(\eta^6\text{-}BDC)Cr(CO)_3]_3$. However, the binding of the H_2 involved photolysis to replace a carbonyl CO ligand with a H_2 molecule. This again highlights the importance of metals that are not fully coordinated so that they can bind hydrogen strongly. Shi, Li and Wu[42] have involved the Kubas interaction as an explanation of enhanced hydrogen adsorption on zeolite NaX with a monolayer of MnO_2 dispersed over the surface, but do not provide further experimental evidence for this. Due to

24

these experimental difficulties there may be other materials that interact with H_2 through the Kubas interaction but they are not presented as such in the literature due to a lack of knowledge and in some cases there may be so few sites that can bind through the Kubas interaction that other interactions dominate. None of the above highlighted materials, however, present the definitive evidence of the Kubas interaction by showing H_2 rotational transitions in inelastic neutron scattering experiments.[33]

There have also been experimental studies on molecular models of the binding sites in hydrogen storage materials in order to reduce the experimental difficulty of characterising the $M–H_2$ interaction. For example, Ti-benzene[44] and Ti-ethylene[67] complexes have been formed in an ultrahigh vacuum chamber and were found to bind hydrogen, though the nature of the $M–H_2$ interaction has not been analysed spectroscopically. These systems would not be practical hydrogen storage materials but these models have been studied computationally[58, 68] and could represent hydrogen binding to metals bound to graphene and similar systems.

There are some computational studies that are closely related to experimental systems.[45-47] Sun, Kim and Zhang[47] and Zhou and Yilidirim[46] examine the same Mn_4Cl-MOF system independently whilst Solons-Monfort and co-workers[45] examine a zeolite with Cu^+ and FeO^+ extraframework cations. Interestingly Zhou and Yildirim and Sun, Kim and Zhang disagree on whether the hydrogen is binding to the Mn through the Kubas interaction. Both parties have undertaken similar computational investigations but interpret the evidence differently. Sun, Kim and Zhang cite the high hydrogen binding enthalpies and orbital interactions as evidence for Kubas binding, whereas Zhou and Yildirim do not feel that the H–H bond lengthens or that its frequency reduces sufficiently for the Kubas interaction to be present, nor that there is enough charge transfer between the H_2 and the metals. They cite significant attractive electrostatic interactions for the high enthalpies that they also observe. Due to neither party examining the same aspects of the results I feel that the situation is still unresolved.

25

There are further computational studies, independent of experimental work, of MOFs[65, 69, 70] but most computational studies are of various carbon networks, possibly doped with boron, with early transition metals bound to them.[49-56, 58-60, 63, 66, 71] There are some exceptions such as studies of metals and alloys,[48] transition metals bound to functional groups[62, 72] and polymers[61] and titanium substituted boranes.[64]

Within the computational studies certain trends in results and methodology are discernible that relate to the PhD work described later and will now be highlighted.

Density Functional Theory (DFT) is a popular choice of calculation method, as observed by Kubas,[33] with only a few choosing to employ MP2[51, 64, 66, 69] and this mainly as a comparison or supplement to the DFT.[51, 64, 69] Of those that use DFT the Perdew-Burke-Ernzerhof (PBE) functional is very popular[46, 47, 49-51, 56, 59, 61, 62, 64, 69, 72] with only a few other functionals utilised including B3LYP,[45, 60, 63] BLYP,[65] B3PW91,[48] BP86[70] and PW91.[54, 55, 71]

Most of the computational studies referenced here involve H_2 interacting with metal centres that are bound to other groups or ligands. The early first row transition metals are a popular choice of metal with Ti as the most popular.[48, 49, 52-54, 58, 62, 64] This may as much be a choice based on computational efficiency, due to the fewer d electrons, as well as thoughts of minimising the gravimetric density of the hydrogen storage material.

Hydrogen has been found to bind to these materials as two hydride ligands [48, 52, 56, 63] as well as molecularly, and in most of the molecular cases the hydrogen is thought to bind through the Kubas interaction. The type of metal seems to greatly affect whether the H_2 binds in a Kubas fashion. The transition metals are thought to bind H_2 through the Kubas interaction but metals from groups one and two of the periodic table only do so under special circumstances. For example, Wu and co-workers[55] found in a study with Sc and Ca bound to B_{80}

buckyballs that the Ca interacted with the H_2 through a weaker induced dipole interaction but that the Sc interacted through a Kubas type interaction. This was also found by Zou and co-workers[54] in a study with Ca and Sc bound to boron doped carbon organic frameworks (COFs) made up of benzene rings. Li^+ was also found to bind to the H_2 through a charge induced interaction[69] as was Mg^{2+} in representations of the metal sites in MOFs.[65] Ni^{2+} in the same system as the Mg^{2+} was found to bind H_2 in a Kubas type interaction.[65] Interestingly Kim and co-workers[51] found that Ca bound to graphene could alter its interaction with H_2 from that of an induced dipole to Kubas type as more H_2 was bound. Initially the H_2 interacted in an induced dipole interaction with the 3s orbital but this raised the energy of the 3s orbital such that it became higher than the 3d orbital. The 3d orbital then became populated such that the Ca could interact via a Kubas interaction and the binding energy therefore also increased as more H_2 was bound.

The strength of the M–H_2 binding enthalpy as a function of the hydrogen coverage is a major theme in the PhD work that follows. In the literature, materials that are thought to interact with the H_2 molecule through the Kubas interaction show various trends. Some materials show a fall in the M–H_2 interaction energy as more H_2 is bound, such as in the study by Zhu and co-workers[63] where the Ti–H_2 interaction energy falls as more H_2 is bound to their molecular Cp_2Ti_2 systems. This has also been seen experimentally such as in the study by Dincă, Long and co-workers[28] where the isosteric enthalpy of adsorption fell as more hydrogen was bound to their MOF with exposed Mn^{2+} sites. Some studies found that the M–H_2 interaction energy did not alter significantly as a function of the number of bound H_2 molecules such as in that by Zhang and co-workers[64] with Ti substituted boranes. While others found that the M–H_2 interaction as a function of the number of bound H_2 molecules either rose or fell depending on the metal and on which ancillary ligands were bound to it, such as in Zhao and co-workers' study of hydrogen binding to metal coated buckyballs,[56] and Lee, Choi and Ihm's study of H_2 binding to metals attached to functional groups.[61]

The partial charge of the metal bound to the H_2 as a function of the number of H_2 molecules bound is also of interest. It was seen by Zhang and co-workers[64] that the partial charge of the Ti attached to their boranes reduces as more H_2 is bound. For example, with B_5H_5Ti the natural charge on the Ti reduces from +1.24 with no H_2 bound to -0.82 with five H_2 molecules bound. In Kosa and co-workers'[65] study of molecular analogues of MOF binding sites, the partial charges were used to highlight the greater interaction with the H_2 of the Ni^{2+} sites compared to the Mg^{2+} sites, due to the Ni interacting though the Kubas interaction and the Mg only through induced dipole interactions. The formal charge on the Ni reduced from +2 to +1.04 but that of the Mg only reduced from +2 to +1.74. The metals become more negative as more H_2 is bound in these cases suggesting that, if the H_2 is binding through the Kubas interaction, the overall interaction is dominated by the σ-donation from the H_2 to the metal rather than the π-back-donation from the metal to the H_2.

The M–H_2 interaction as a function of the transition metal is also of interest. There is a general trend for Sc to have a low M–H_2 interaction energy[47, 61, 62] compared to Ti or V and this is not surprising as Sc does not have d electrons and therefore can not take part as readily in the π-back-donation component of the Kubas interaction. Few studies compare metals across the whole first period of the transition metal block of the periodic table.[56, 58] One that does, involving H_2 binding to metals bound to ethylene,[58] suggests that the M–H_2 interaction energy is generally higher for early and late transition metals excluding Sc and Cu with empty and full d shells respectively, as does the other,[56] involving H_2 bound to metals bound to buckyballs, though the trend is less well defined. Perhaps early transition metals benefit from many unfilled d orbitals and late transition metals from many full d orbitals such that the σ-donation and π-back-donation of the Kubas interaction can dominate respectively. With few studies though and trends ill-defined I believe that the matter is open to debate.

The M–H_2 interaction as a function of the ligands bound to the metal is also of interest. Some studies alter the type of ligand bound to the transition

metal only slightly[62] and therefore trends in M–H_2 interaction energy are hard to observe. However, in the studies by Lee and co-workers on titanium bound to polymers[61] and functional groups[72] the ligands were altered significantly. The polymers were altered from polyacetylene to polypyrrole and polyanaline but the M–H_2 interaction energy did not give a clear trend as a function of ligand. The functional group was changed between a thiol, an alcohol, a carbon to carbon triple bond C≡C, a nitrile and an isocyanate. The M–H_2 interaction generally seemed to decrease the better the ligand at accepting π electron density from the metal. For example, the binding of the first H_2 molecule to the Ti bound to the carbon triple bond C≡C was about 0.1 eV but bound to the thiol was about 0.9 eV. It would be expected that the ancillary ligands that are good π-acceptors would give weak M–H_2 interactions as less π electron density would be available on the metal to donate to the hydrogen. Kosa and co-workers[65] did not alter the types of ligands but did alter the ligands' relative positions in their study of the molecular analogues of Ni^{2+} and Mg^{2+} binding sites in MOFs. They found that the M–H_2 interaction energy was sensitive to the ligands' relative positions and therefore concluded that the hydrogen adsorption properties of MOFs would be dependent on the fine detail of their crystal structures. Due to the few studies in this area I again believe that the trends are open to debate.

The experimental systems investigated in this computational study are those of Prof Antonelli and co-workers. Initial work focused on amorphous mesoporous silica based materials with dispersed transition metal binding sites[65-68] and moved onto amorphous gels made up of transition metal binding sites linked by hydrazine based ligands.[69-71]

Experimental Materials

The experimental work of Prof. Antonelli and co-workers will now be described in detail as this provides much of the focus of this PhD thesis, before moving on to the description of the course that the PhD took, the background theory and the computational systems that represent the experimental materials.

The silica based material[73] is an amorphous mesoporous silica with 23 Å wide pores and a Brunauer, Emmett, Teller (BET) surface area of 1219 m^2g^{-1} with titanium binding sites all over its surface and within the pores at 0.4275 per nm^2. The titanium is either bound to the surface with two bonds and has one benzyl ligand bound to it or is bound to the surface with one bond and has two benzyl ligands bound to it (Figure 3). These two types of binding sites are in a 55:45 ratio.
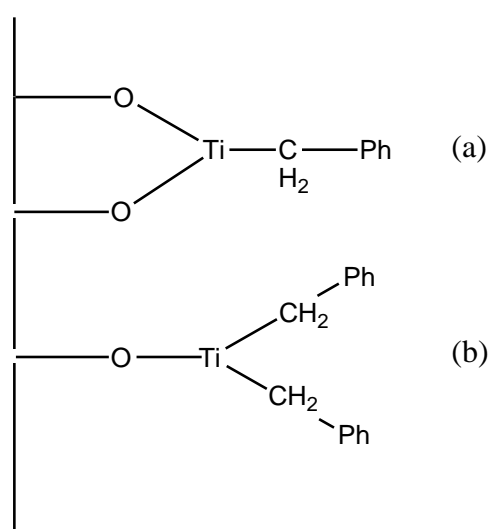
Figure 3: Schematic representations of (a) a benzyl disiloxy titanium(III) binding site and (b) a dibenzyl siloxy titanium(III) binding site.

The hydrogen adsorption capacity (hydrogen adsorbed to the walls of the material) and the hydrogen adsorption enthalpy both increase with increasing hydrogen pressure and surface coverage up to maxima of 1.66 wt %, which equates to 2.7 H_2 molecules per Ti, and 22.14 $kJmol^{-1}$ respectively at 77 K. This enthalpy is in the desired range for hydrogen storage making it of particular interest. The capacity decreases as the temperature is increased to 195 K and 298 K reducing to 0.99 wt %/2.4 H_2/Ti and 0.69 wt %/1.1 H_2/Ti respectively.

After my computational study of the silica based material, the experimental system was optimised[74] by varying the conditions of its formation. This involved altering the Si-to-surfactant molar ratio and surfactant chain length whilst forming the mesoporous silica substrate. Varying these conditions controlled the surface area and pore size of the material. The precursor used to form the titanium binding sites on the solid and its loading level were also varied, which is thought to control the extent to which clustering of the titanium occurs on the silica. By varying these conditions the optimum hydrogen capacity and adsorption enthalpy were both increased to 3.05 wt%/4.85 H_2/Ti and 23 kJmol^{-1} respectively.

The later work also varied the ancillary ligand bound to the titanium from benzyl to allyl or methyl.[75] Attempts to form a hydride analogue were not published. X-ray photoelectron spectroscopy (XPS) studies of the systems show that the π-back-donating ability to the H_2 molecule decreases in the order methyl > allyl > benzyl. A larger π-back-donating ability would suggest a greater propensity to form a strong M–H_2 interaction. The adsorption capacities (~1.4 wt%) and hydrogen adsorption enthalpies (~3 kJmol^{-1}) are significantly lower however for these systems. This was concluded to be due to THF being present bound to the titanium. The THF is required as the solvent for the synthesis of the allyl or methyl analogues but not for benzyl. In a separate study, where the metal was also altered[74] and hydrogenation of the ancillary ligand led to the formation of a hydride, it was also generally concluded that a hydride ligand gave improved H_2 storage properties than carbon based ligands.

The experimentalists' later work also varied the metal and its oxidation state to +2.[74, 76] However, keeping the same ancillary ligand bound to the metal centres proved impossible due to the different availabilities and stabilities of early transition metal alkyls in the +2 and +3 oxidation states that are used to form the binding sites on the silica surface. Despite this, it was generally concluded that the hydrogen storage material performed better in relation to the metal in the order Ti > V > Cr and in relation to the oxidation state that M(II) performed better than M(III).

Hydrazine Linked Materials

Due to the low percentage of Ti, unstable surface metal fragments and the binding of most of the H_2 through physisorption in the silica based materials, Prof. Antonelli and co-workers progressed to exploring hydrazine linked materials.[77] The hydrazine linked systems that have been investigated are amorphous gels and are made up of metal centres with unknown coordination environments connected by hydrazine based ligands. By hydrazine based ligands I refer to both hydrazide (NH_2NH) and hydrazine (NH_2NH_2). This PhD work was based on two experimentally realised materials with Cr[77] and V[78] metal centres respectively. After this computational study was completed experimental research was also carried out on a hydrazine linked material with Mn metal centres.[79]

The materials with hydrazine linked Cr centres are largely amorphous (X-ray diffraction (XRD) shows broad, low-intensity reflections from $2\theta = 30 - 35^o$ that do not correspond to any known Cr-N phase) with Cr(II), Cr(III) and Cr(IV) sites, although the majority are Cr(II). X-ray photoelectron spectroscopy (XPS) shows that the binding mode of the hydrazine and the way that it links the binding sites together also vary, although mostly it links in a $-NH-NH_2-$ fashion. During synthesis, each Cr(II) has a bis[(trimethylsilyl)methyl] ligand bound to it initially, which is then hydrogenated off. Proposed structures for the Cr(II) sites within the gel before and after hydrogenation are shown in figures 4A and 4B respectively, although the coordination number and the geometry of the ligands about the metals are not known. This is due to the air sensitive, paramagnetic, and amorphous nature of these materials precluding more detailed methods of structural characterization. At room temperature there is a significant increase (~ 1 wt%) in the hydrogen storage capacity after hydrogenation. However, this is not seen at 77 K at which temperature all of the binding sites are filled, indicating that the hydrogenation does not alter the number of binding sites but that their binding enthalpy increases so that more sites are occupied at room temperature. The binding enthalpies increase with increasing hydrogen coverage before

32

hydrogenation to a maximum of 17.86 kJmol^{-1} and after to 51.58 kJmol^{-1}. The maximum storage capacity of 3.2 wt% at 170 bar equates to 1.75 H_2/Cr.

A

B
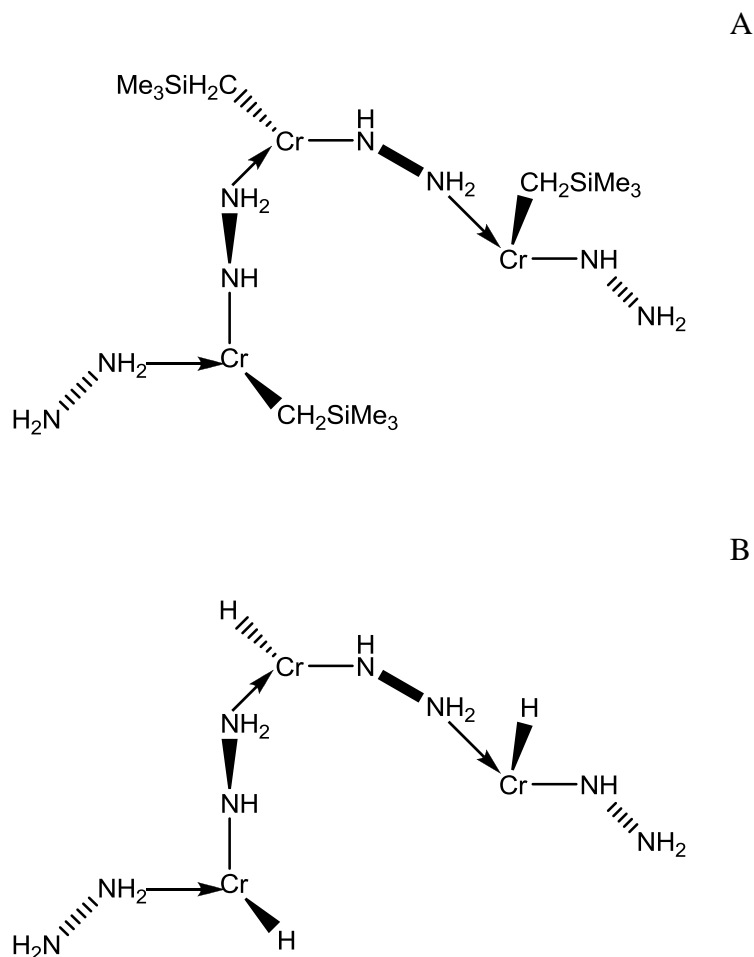
Figure 4: Schematic representations of the experimentalists' proposed structures of the Cr(II) hydrazine linked materials, A, before hydrogenation and, B, after hydrogenation.[77]

The second hydrazine linked, mainly amorphous (XRD displays a single broad reflection at low angle that suggests mesoscopic order,[79]) gel has mainly V(III) centres, though there are some V(0), V(I) and V(IV) centres.[78] Each is thought to have a THF ligand and the rest of the coordination sphere is made up of hydrazine based ligands (Figure 5). The binding enthalpy of the hydrogen

33

rises with increasing H_2 coverage to a maximum of 36.5 kJmol^{-1} and a maximum of 1.96 H_2/V bind at 77 K.
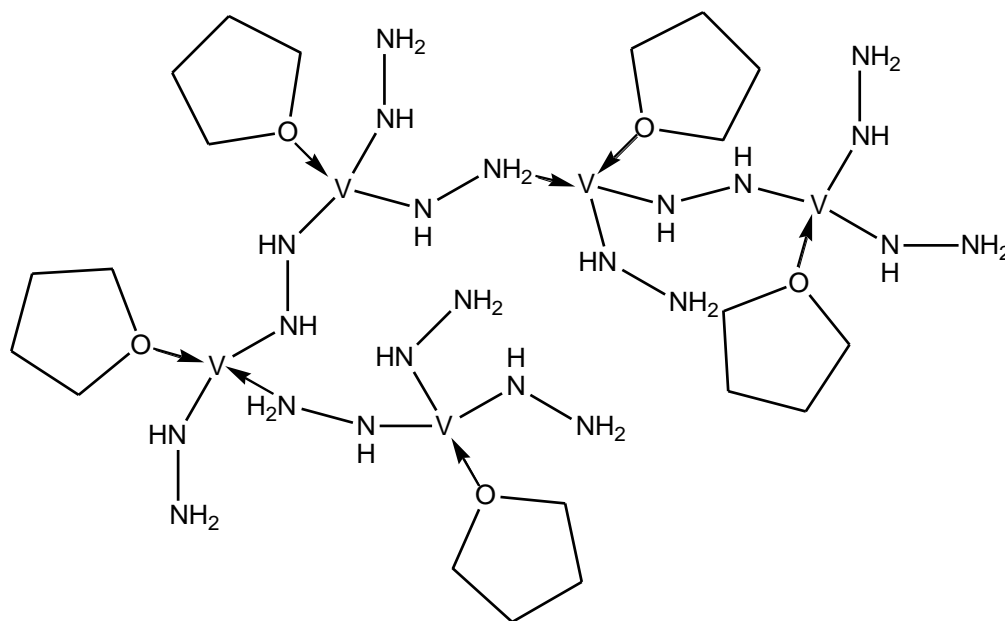
Figure 5: Schematic representation of the experimentalists' proposed structure of the V(III) hydrazine linked materials.[78]

Hydrazine linked materials with Mn metal centres[79] were also investigated as Mn is cheaper than Cr and Mn(II) is more air stable than Cr(II). The materials were found by X-ray diffraction to be completely amorphous and are unfortunately pyrophoric in air. Some residual trimethylsilylmethyl groups remain bound to the mainly Mn(II) centres but there are also Mn(0), Mn(IV) and Mn(VII) centres. There is a slight irreversibility of H_2 binding with H_2 adsorption enthalpies rising with hydrogen coverage roughly from 1.3 kJmol^{-1} to 39 kJmol^{-1} with a maximum of 0.59 H_2/Mn bound at 77 K.

All of the hydrazine linked materials have been studied by X-ray photoelectron spectroscopy and the results on all the materials have suggested that they are either narrow bandgap semiconductors or semi metals.[79]

All materials studied by Prof. Antonelli and co-workers have shown rising hydrogen binding enthalpies with hydrogen surface coverage which is opposite to the behaviour of materials that physisorb hydrogen and suggests an alternative adsorption mechanism is taking place. Inaccurate isotherms or measurement techniques have been ruled out as the group have measured the adsorption enthalpy of carbon AX-21 under the same conditions as their materials and have found that its adsorption enthalpy decreases with increasing H_2 coverage.[78] Kinetic effects that would block the higher enthalpy binding sites at 77 K and lead to the illusion of rising enthalpies have also been ruled out as an equilibrium is maintained for five minutes before a measurement is taken.[79] Inelastic Neutron Scattering (INS) experiments have not yet been carried out on any of these systems to prove the occurrence of π-back-bonding to the H_2 and thus that the Kubas interaction is the mode of binding, but a Raman study on a similar polymeric system with V(III) binding sites[80] has shown a H–H stretch lower than that of free H_2 and comparable to an IR stretch seen for the classically Kubas system $W(CO)_3(PCy_3)_2(\eta^2\text{-}H_2)$.[81]

Though the hydrazine linked materials are an improvement on the mesoporous silica based materials, hydrazine has many safety issues (toxic, flammable and explosive)[79] and it can also bind in multiple coordination modes. This leads to amorphous systems that are difficult to characterise. Therefore the experimentalists are continuing to explore other low-molecular weight ligands that would support low-coordinate metal sites useful for hydrogen binding.[80]

The aim of this study was to answer computationally the questions posed by these novel materials. These include, what is the maximum number of H_2 molecules that could coordinate to the metal centres, whether these are coordinating through the Kubas interaction, why the binding enthalpy of the H_2 increases as the number of H_2 bound increases and what would be the effect of altering the metal and/or ancillary ligands bound to the metals on the hydrogen storage properties of the materials? In the case of the silica based materials it is also of interest to probe the effect of the η^1 vs η^3 binding modes of the benzyl ancillary ligand on the hydrogen storage properties.

The remainder of this thesis addresses this aim by developing a model of these systems that reproduces the experimental results and then altering this model to reflect the changes of ligand and metal to be probed. Density Functional Theory (DFT) was used as the method of choice as it allows the detailed modelling of the molecular orbital based Kubas interaction and, compared to other *ab initio* methods, it is computationally cheap. The binding sites were modelled as clusters representing the active sites in the extended structures, again to allow a detailed analysis of the M–H$_2$ interaction. These are referred to as binding site representations (BSRs). For the mesoporous silica based material this method is probably entirely justified as the binding sites are spread out over the surface of the material and as such are highly unlikely to interact. However, the metal binding sites in the hydrazine linked materials are at most only separated by two nitrogen atoms and so it is probable that the binding sites would interact. This was probed by looking at models of two linked binding sites and these are referred to as dimers. En route two diversions were required. One of these was a study of some classically Kubas systems, where the M–H$_2$ interaction has been proven to be of a Kubas type through experimental means, in order to benchmark the Quantum Theory of Atoms in Molecules (QTAIM) computational method, for the Kubas interaction. The computational values from this study could then be compared to the studied systems as similarity between the values would add weight to the M–H$_2$ interaction being of a Kubas type in these systems also. The other extension was to use the model to probe other systems that had not been studied experimentally to see whether they would be of interest as hydrogen storage materials.

All of the following work has been written into five papers that have been published in the Journal of the American Chemical Society,[82] Chemistry – A European Journal,[83] Dalton Transactions on the front cover,[84] the Journal of Physical Chemistry C[85] and in Energy Procedia as conference proceedings of the 2012 World Hydrogen Energy Conference respectively.[86]

Density Functional Theory

DFT has been used as the method of choice to model all of the structures in this study. This theory is based on varying the electron density of a given atomic geometry in order to minimise the energy. The lower the energy the closer it is to the true energy, which was shown to be true by Hohenberg and Kohn as the density obeys a variational principle.[90] The electron density is related to the geometry as its integral over all space gives the total number of electrons, the peaks in the density represent the positions of the atoms and the integration over those peaks may give the atomic number of those atoms in an uncharged system.

To find a minimum electron density for a given atomic geometry a type of Schrödinger equation, (2), needs to be solved.

$$\hat{H}^{KS}\rho = E\rho \qquad (2)$$

Here the Hamiltonian operator, $\hat{H}^{KS}$, acts on the electron density, ρ, to give the energy multiplied by the density, ρ. The electron density may be made up from a combination of atomic orbitals, χ. The structure of the Hamiltonian depends on the total number of electrons and the position of the nuclei. The Hamiltonian operator and the energy are functions of the electron density, which in turn is a function of the positions of the nuclei, a functional is a function of a function and hence the name DFT.

The Hamiltonian and the energy are split so that the first terms describe a system of non-interacting electrons that have the same ground state energy as the real, interacting system of interest and thus the same number and position of the nuclei and later terms add corrections to these terms to account for the interacting electrons.

$$E[\rho(r)] = T_{ni}[\rho(r)] + V_{ne}[\rho(r)] + V_{ee}[\rho(r)] + \Delta T[\rho(r)] + \Delta V_{ee}[\rho(r)] \tag{3}$$

Therefore, the energy, $E[\rho(r)]$, is made up of the kinetic energy of the non-interacting electrons, $T_{ni}[\rho(r)]$, the nuclear-electron interaction, $V_{ne}[\rho(r)]$, the classical electron-electron repulsion, $V_{ee}[\rho(r)]$, the correction to the kinetic energy for the interacting electrons, $\Delta T[\rho(r)]$, and corrections to the electron-electron interaction, $\Delta V_{ee}[\rho(r)]$, which includes exchange and correlation and a correction for the classical self-interaction energy. These latter terms are lumped together into the exchange correlation energy, E_{XC}.

$$E_{XC} = \Delta T[\rho(r)] + \Delta V_{ee}[\rho(r)] \tag{4}$$

The Born-Oppenheimer approximation is invoked such that the kinetic energy of the nuclei is ignored as is the electrostatic nuclear-nuclear repulsion, though it is added on later.

The density may be split into single particle densities and the single particle Kohn-Sham operator for one electron is[91]

$$h_i^{KS} = -\frac{1}{2}\nabla_i^2 - \sum_k^{nuclei} \frac{Z_k}{|r_i - r_k|} + \int \frac{\rho(r')}{|r_i - r'|} dr' + V_{XC} \tag{5}$$

The DFT molecular orbitals are the eigenfunctions when this Hamiltonian acts on the atomic orbitals and the eigenvalues are the orbital energies. V_{XC}, is a functional derivative such that

$$V_{XC} = \frac{\partial E_{XC}}{\partial \rho} \tag{6}$$

DFT is an exact theory if the exchange correlation operator is known exactly. However, its form is not known and is thus approximated. DFT may be improved by altering this operator but these changes do not show a clear systematic pattern. It is generally thought that functionals which are local spin density (LSD) corrected, meaning that the exchange-correlation operator depends on the value of the electron density at a point, are not as good as those that employ a generalised gradient approximation (GGA), meaning that the exchange-correlation operator depends on the electron density at a point but also on the gradient of that density.

The principal functional used throughout this work is that of Perdew, Burke and Ernzerhof (PBE)[92, 93]. This is a GGA functional where all the parameters other than those in the LSD part are fundamental constants. Other functionals that were screened include

1. VWN by Vosko, Wilks and Nusair[94] which is the parametisation of the electron gas and is one of the more advanced LDA functionals as it includes correlation effects.

2. BLYP, which is a GGA functional with the Becke[95] exchange correction and the Lee-Yang-Parr correlation correction. The Becke correction has only one experimentally derived parameter while the Lee-Yang-Parr correction has several.[96-98]

3. B3LYP by Stephens, Devlin, Chablowski and Frisch is a hybrid GGA meaning that it is formed from the exchange-correlation functional BLYP but also mixes in 20% exact exchange from Hartree Fock theory.[99] This was first suggested by Becke.[100]

4. PBE with dispersion, which is PBE with an added correction by Grimme for the dispersion which contains several experimental parameters.[101]

Self-Consistent Field Procedure

The DFT (or Kohn-Sham) molecular orbital energies are found using a self-consistent field (SCF) procedure. In order to carry out a SCF procedure a

basis set of N functions, ϕ_i, is taken to represent the atomic orbitals and the basis set coefficients a_{ij} for each of the N molecular orbitals need to be found. These coefficients determine how much each of the basis set functions contributes to that molecular orbital such that the wavefunction of it, ψ_j, is given by equation (7), i.e. the Linear Combination of Atomic Orbitals (LCAO).

$$\psi_j = \sum_{i=1}^{N} a_{ij}\phi_i \tag{7}$$

We can find these coefficients by solving equation (8).

$$E_k = \frac{\sum_{ij} a_{ik} a_{jk} \int \phi_i \hat{H} \phi_j d\mathbf{r}}{\sum_{ij} a_{ik} a_{jk} \int \phi_i \phi_j d\mathbf{r}} \tag{8}$$

To solve this $\frac{N}{2}(N+1)$ values of H_{ij}, (9), and S_{ij} ,(10), are computed for all of the electron pairs.

$$H_{ij} = \int \phi_i \hat{H} \phi_j d\mathbf{r} \tag{9}$$

$$S_{ij} = \int \phi_i \phi_j d\mathbf{r} \tag{10}$$

The 'correct' groundstate wavefunction will be that with the lowest energy. The coefficients need to be selected to give the minimum energy, E. If this were true then the partial derivative of E with respect to any coefficient would give zero, (11).

$$\frac{\partial E}{\partial a_j} = 0 \qquad \text{for all } j \tag{11}$$

For this to be true equation (12) must be true

$$\sum_{i=1}^{N} a_i \left(H_{ji} - ES_{ji} \right) = 0 \qquad \text{for all } j \qquad (12)$$

There are N equations and N unknowns, forming a secular determinant, (13).

$$\begin{vmatrix} H_{11} - ES_{11}, H_{12} - ES_{12} \cdots\cdots\cdots H_{1N} - ES_{1N} \\ \cdots\cdots\cdots\cdots\cdots\cdots\cdots\cdots\cdots\cdots\cdots\cdots\cdots\cdots\cdots \\ \cdots\cdots\cdots\cdots\cdots\cdots\cdots\cdots\cdots\cdots\cdots\cdots\cdots\cdots\cdots \\ H_{N1} - ES_{N1}, H_{N2} - ES_{N2} \cdots\cdot H_{NN} - ES_{NN} \end{vmatrix} = 0 \qquad (13)$$

The solution of the secular determinant gives N values of E each with a different set of coefficients, a_{ij}. The lowest energy E is the ground state energy. To find its coefficients the set of linear equations are solved, (13). The higher E are the energies of the 'excited states'.

This process must be done iteratively. To construct the Hamiltonian the positions of the nuclei and electrons must be known and so the electron density must be known and for this the basis set coefficients must be known. These coefficients are found by solution of the secular equation for which the Hamiltonian is required. Therefore an initial molecular geometry is chosen, all of the integrals for the system where the electrons do not interact are computed and the initial coefficients are guessed. These coefficients are used to construct the Kohn-Sham secular equation. The coefficients found using the lowest E from the solution of this secular equation and solving the linear equations are then compared with the coefficients used in its construction. The process is continued until the coefficients found from the solution of the secular equation are sufficiently similar to those used in its construction.

Geometry Optimisation

A geometry optimisation may be carried out once the SCF has been converged in order to find a stationary point on the potential energy surface of the molecule, where the forces acting on the atoms are zero with respect to alteration of their relative geometry. The first derivative of the energy with respect to each of the $3N$ coordinates is calculated where N is the number of atoms in the molecule. The next step is to calculate the second derivative of the energy with respect to the $3N$ coordinates. The matrix of second derivatives is known as the Hessian. The Hessian gives the curvature of the surface for that particular geometry and may be used by an algorithm to determine a change in the geometry for the next step. The Berny algorithm is used in the Gaussian 09 program[102] and this algorithm takes into account the values of the Hessian of previous geometry steps. Overall the geometry is moved along the path of steepest descent of the Hessian. The geometry of the current step is then tested to see if it meets the convergence criteria. In Gaussian the maximum force component (the size of any first derivative away from zero), the root mean squared (RMS) force, the maximum step component (the distance that an atom will be moved from its current position to its new position in the geometry of the next step) and the RMS step all need to be below a certain threshold. If the convergence criteria are not met then the geometry will be altered and the SCF procedure will be repeated at the new geometry. The derivatives are recalculated and the geometry is again tested for convergence. This is repeated until the convergence criteria are met.

Analytical Frequency Calculation

Once the geometry convergence criteria have been met an analytical frequency calculation may be performed. This involves calculating the Hessian and then converting it to mass-weighted coordinates. This Hessian is then diagonalised to give the eigenvectors, which correspond to the vibrational, translational and rotational modes of the molecule and the eigenvalues, whose

roots are the fundamental frequencies of the modes of motion of the molecule. Any of these roots that are zero (or very near zero) are the translational and rotational modes while any above zero are the vibrational frequencies of the molecule. Any eigenvalues which are negative would lead to an imaginary frequency. If there are imaginary frequencies (shown as negative frequencies in the Gaussian output) then the molecule has not reached a true minimum. If there is one imaginary frequency then this may indicate that a transition state has been reached. The direction of the vibration would then give the reaction coordinate.

Basis Sets

A way of systematically improving calculations is to increase the quality of the chosen basis set. The larger the basis set the more coefficients, the more mathematical functions describing each orbital and the more precise the description of the electron density. Basis sets are chosen in such a way that they can be computed in an efficient manner, have as few functions as possible, and make chemical sense, e.g. their amplitude is large where the electron density is large.

The types of functions making up the basis sets in the calculations, which follow, are either Slater-type orbitals (STOs), (14) or Gaussian functions.

$$\Psi(r,\theta,\phi:\xi,n,l,m) = \frac{(2\xi)^{n+\frac{1}{2}}}{[(2n)!]^{\frac{1}{2}}} r^{n-1} e^{-\xi r} Y_l^m(\theta,\phi) \tag{14}$$

$\xi =$ Exponent which depends on a set of rules developed by Slater that depend on the atomic number

$n =$ Principal quantum number for the valence orbital

$Y_l^m(\theta,\phi) =$ Spherical harmonic functions which depend on the momentum quantum numbers m and l of the orbital.

The STOs are similar to the hydrogenic orbitals as the 1s orbital has a cusp at the nucleus and there is the correct exponential decay with increasing distance of the electron from the nucleus, r. The TZ2P bases[103-107] used later are made up of these functions. This short hand name means that the core orbitals are double zeta, the valence orbitals are triple zeta, and it is double polarised. This means that for each atom the core orbitals are represented by two STOs, the valence orbitals are represented by three and then there are two STOs with a higher orbital angular momentum than the valence orbitals. The STOs with angular momentum higher than the valence allow for greater deformation of the electron density when interactions occur between atoms.

The other sort of function used in the calculations is the Gaussian function. The function differs from a STO only in the radial component, which instead of a radial decay proportional to $e^{-\xi r}$ it is proportional to $e^{-\xi r^2}$. For Gaussian functions the exponent is usually labelled as α rather than ξ. They do not have a cusp at the nucleus and the function decays too quickly at large values of r. Gaussian functions are used as the integrals involving them are easier to calculate than those of STOs, however, it has been seen that the precision of the calculations using Guassian basis sets does not increase as swiftly with basis set size when compared to STOs,[108] therefore, to make them comparable in their description of the electron density several Gaussian functions need to be used for every STO. They are fitted to a STO by combining them through a linear combination and altering the relative weights. These contracted Gaussians are then used in the calculations. In the following calculations the 6-311++G** basis set[109-115] was used. This means that each set of core orbitals is represented by a contracted Gaussian made up of six Gaussian functions and that each valence orbital is represented by three contracted Gaussians with one made up of three Gaussians and two made up from one. There is also one diffuse function on every atom, these are Gaussian functions that decay away slowly with increasing r but have the same angular dependence as the valence, represented by the + signs. There are also polarisation functions on all atoms represented by the *'s. The 6-311++G** basis set may be considered to be of similar quality to the TZ2P basis set.

Quantum Theory of Atoms In Molecules[116]

Once the minimum energy electron density has been found it may be analysed using the Quantum Theory of Atoms in Molecules (QTAIM).[117] This theory was developed by Prof. Richard F. W. Bader and co-workers in the 1960s and may be applied to experimentally as well as theoretically derived electron densities.

In the QTAIM critical points in the density are found where the first derivatives of the density with respect to any direction are zero.

$$\nabla \rho = i \frac{\partial \rho}{\partial x} + j \frac{\partial \rho}{\partial y} + k \frac{\partial \rho}{\partial z} = 0 \qquad (15)$$

The second derivatives of the density at this point determine the type of critical point. There are four types of critical point.

1. All three second derivatives with respect to the x, y and z directions are negative meaning that the density is a local maximum. This is known as a nuclear critical point (NCP) and shows the location of an atom.

2. Two of the second derivatives are negative and one is positive meaning that the density in one plane is a maximum but is a minimum perpendicular to this plane. This is known as a bond critical point (BCP). This is the point on the path of highest electron density connecting 2 nuclei, the bond path, where the electron density is at its minimum. The presence of a bond path and BCP indicates that chemical bonding is occurring between the two atoms involved. Taking z to be the direction of the bond path, the second derivative with respect to the z direction is positive and the second derivatives in the x and y directions are negative at the BCP.

3. Two of the second derivatives are positive and one is negative meaning that the density is a minimum in a plane but a maximum perpendicular to

the plane. This is known as a ring critical point (RCP) and is the point surrounded by bond paths where the density is a minimum on the plane of maximum density created by the bond paths.

4. All three derivatives are positive meaning that the density is a local minimum. This is known as a cage critical point (CCP) and is the point surrounded by RCPs where the density is a minimum.

The number of critical points for an isolated finite molecule follows the Poincaré-Hopf relationship, (16), where n is the number of critical points of the particular type subscripted.

$$n_{NCP} - n_{BCP} + n_{RCP} - n_{CCP} = 1 \qquad (16)$$

Nuclei and their associated critical points and lines representing the bond paths between those nuclei are known as molecular graphs.

The bond order, BO, of a chemical bond, which is closely related to its strength, is related to the electron density at the BCP, ρ_b, by, (17).

$$BO = \exp[A(\rho_b - B)] \qquad (17)$$

A and B are positive constants which depend on the nature of the bonded atoms. Generally BCP densities are greater than 0.2 a.u. for covalent bonds and less than 0.1 a.u. for closed-shell interactions like ionic or Van der Waals bonding.[116] The electron density at the bond critical point has been shown to be strongly correlated with the bond energies. Curved bond paths indicate that the bonding is strained in some way.

The overall second derivative at a BCP is known as the Laplacian, $\nabla^2 \rho(r)$, and is the sum of the second derivatives of the density at the BCP with respect to the x, y and z directions, (18).

$$\nabla^2 \rho(r) = \nabla.\nabla\rho(r) = \frac{\partial^2 \rho(r)}{\partial x^2} + \frac{\partial^2 \rho(r)}{\partial y^2} + \frac{\partial^2 \rho(r)}{\partial z^2} \qquad (18)$$

As mentioned previously, at a BCP the second derivatives with respect to the x and y directions are negative as the density is a maximum perpendicular to the bond path and that with respect to the z direction is positive as the BCP is a minimum in the direction of the bond path. The more negative the x and y derivatives, the more density is concentrated in the bond path, and the more positive the z derivative, the less density is concentrated at the BCP compared to the nuclei. Therefore, for covalent bonds the Laplacian is generally negative as the electron density is concentrated more at the BCP than at the atoms and the negative second derivatives dominate. For non-covalent bonds the Laplacian is generally positive as the bonding involves a depletion of electron density at the BCP.

In QTAIM the molecular space is partitioned about each nucleus into atomic basins, Ω. The surface area of this region for a nucleus cuts through but does not cross any of the critical points around that nucleus and follows the contours of the electron density between them. The Bader partial charge, $q(\Omega)$, of an atom can be found by summing the density within the atomic basin of that atom and taking it away from its nuclear charge, (19).

$$q(\Omega) = Z_\Omega - \int_\Omega \rho(r)dr \qquad (19)$$

A bond catastrophe can occur where a RCP and a BCP are so close together that they cancel each other out. This can occur without breaking the Poincaré-Hopf relationship and occurs either when a bond of a stable ring structure is stretched[118] or when the electron density in that region is flat. The later scenario has been seen experimentally by Sparkes and co-workers[119] for the coordination of a C=C double bond with a metal and by Furrugia and co-workers[120] for an oxygen to H–C interaction.

Partial Charge[121]

The Bader partial charge is not the only method of calculating the partial charge on an atom within a system and the other methods that were employed in this study are those of Mulliken,[122-125] Hirshfeld[126] and Voronoi.[121, 127]

The Mulliken partial charge for an atom is found by first summing together the electron density within the basis functions centred on that atom, (20). Each basis function has a component that is entirely centred on that atom, $\mathbf{D}_{\mu,\mu}S_{\mu\mu}$, and a component called the overlap population, $\mathbf{D}_{\mu,\nu}S_{\mu,\nu} + \mathbf{D}_{\nu,\mu}S_{\nu,\mu}$, which is shared with another atom. Half of the overlap population is assumed to be associated with each atom. The sum of the electron density within the basis functions, Q_μ, is then taken away from the nuclear charge to give the Mulliken partial charge, (21).

$$Q_\mu = \mathbf{D}_{\mu,\mu}S_{\mu,\mu} + \sum_{\nu(\neq\mu)} \frac{1}{2}\mathbf{D}_{\mu,\nu}S_{\mu,\nu} + \mathbf{D}_{\nu,\mu}S_{\nu,\mu} \tag{20}$$

$$Q_A^{Mulliken} = Z_A - \sum_{\mu\in A} Q_\mu \tag{21}$$

The Hirshfeld and Voronoi partial charge analyses do not base themselves on the molecular orbitals but partition the electron density. The Hirshfeld measure of the partial charge, $Q_A^{Hirshfeld}$, compares the electron density of the molecule to that of a promolecule. The promolecule electron density, $\rho_{promolecule}$, is the sum of all the usually spherically averaged ground-state atomic densities.

$$\rho_{promolecule}(\mathbf{r}) = \sum_B \rho_B(\mathbf{r}) \tag{22}$$

48

The amount of the final electron density associated with an atom is then taken in the same ratio as the atomic densities, ρ_A, contribute to that atom in the promolecule, $\rho_A^{molecule}(\mathbf{r}) = (\rho_A(\mathbf{r})/\rho^{promolecule}(\mathbf{r}))\rho^{molecule}(\mathbf{r})$. This electron density is then taken away from the nuclear charge, Z_A, on that atom to give the Hirshfeld partial charge, (23).

$$Q_A^{Hirshfeld} = Z_A - \int \frac{\rho_A(\mathbf{r})}{\rho_{promolecule}(\mathbf{r})} \rho_{molecule}(\mathbf{r})d\mathbf{r} \qquad (23)$$

The Voronoi deformation density partial charge, Q_A^{VDD}, is found for an atom by integrating the difference in the electron density of the real molecule compared to the promolecule over the volume that is closest to that atom, the Voronoi cell, (24).

$$Q_A^{VDD} = -\int \left[\rho(\mathbf{r}) - \rho_{molecule}(\mathbf{r})\right]d\mathbf{r} \qquad (24)$$

The PhD work follows on from that of my Masters project on the same topic when initial calculations on the silica based materials were performed.[128] During the Masters Project a computational method was developed that has been applied to all of the systems studied during my PhD project with a few minor adjustments on how the metal to hydrogen (M–H_2) interaction energy was calculated. It was during the Masters Project that the decision was taken to model the H_2 binding sites as molecules, known as binding site representations (BSRs) and to use Density Functional Theory (DFT) as the method of choice. To select the particular flavour of DFT a range of functionals were probed with respect to the different values that they gave for the M–H_2 interaction energies (Figure 6).
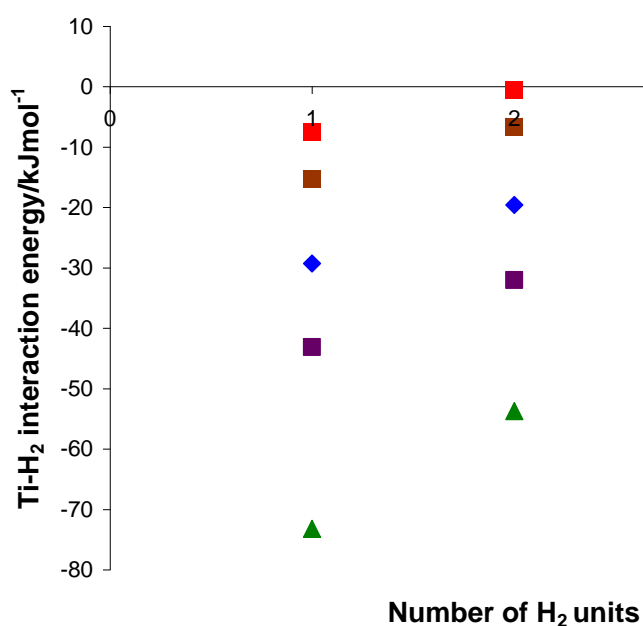
Figure 6: The Ti(III)–H_2 interaction energy for the silica based BSR with two benzyl ligands and various functionals, PBE blue, PBE with dispersion purple, LDA VWN green, BLYP brown and B3LYP red. The geometry was taken from preliminary calculations using the PBE functional.[128]

All of the functionals produced the same trend in the interaction energies as a function of the number of H_2 units bound. The Perdew-Burke-Ernzerhof (PBE)

functional was selected [92, 93] and used throughout as it gave absolute values that were the closest to those of the experiment and were the lowest out of the GGA functionals. GGA functionals are generally considered to be more accurate than LDA functionals and from the variational principle the lower the energy the closer it is to the true energy. However, the PBE functional may well be systematically overestimating the energy of the bond in this case. The dispersion correction by Grimme[101] was discounted as it increased the binding energies by 20 kJmol^{-1} from the PBE value and so did not add any further information to the trend in the values while moving the absolute values away from those of the experiment. It is pleasing to note that it has been shown by Sun and co-workers that PBE is the best functional to balance computational speed and accuracy when looking at dihydrogen bound to metal centres[71] and that it has been used by many others in this area of research.[56, 59, 61, 64, 69, 72, 129-132]

During the Masters project initial geometry optimisations were carried out using the Amsterdam Density Functional (ADF) program.[133] This code is specialised for performing DFT calculations on molecular systems using Slater type orbitals (STOs) that are calculated numerically. However, it was realised that the number of H_2 units that could be bound was basis set dependent. Calculations were then carried out in the Gaussian 03 code[134] where a greater variety of basis set, including Pople and Dunning type basis sets, and method, including Møller–Plesset perturbation theory to second order (MP2), Hartree Fock (HF) and ONIOM (our own n-layered integrated molecular orbital and molecular mechanics) where molecular mechanics and quantum mechanics may be combined in the same calculation, are possible. The size of the basis set was increased until the number of H_2 units that could be bound saturated and, as a result, the 6-311++G** basis[109-115] set was selected. The integration grid size and convergence criteria were also optimised for the maximum number of H_2 units that could be bound. Test calculations with MP2 and HF methods proved unsatisfactory and were not continued past the Masters project as the Hartree Fock calculations produced inaccurate structures and the MP2 SCFs failed to converge. The Gaussian 03 code was used for all geometry optimisations for the silica systems whilst the Gaussian 09 code[94] was used for the hydrazine linked

systems, and the 6-311++G** basis[109-115] sets were used on all atoms. An ultrafine integration grid was used and the RMS force geometry convergence criterion was set to 0.000667 a.u. using IOP 1/7. Stationary points were analysed by performing analytical frequency calculations.

Atoms in Molecules (AIM) calculations were performed using the AIMALLPro[135] programme on the electron densities at the Gaussian optimised geometries, employing formatted Gaussian checkpoint files as input. AIMALLPro is specifically written for performing quantitative and visual Quantum Theory of Atoms in Molecules (QTAIM) analysis of molecular systems starting from molecular wavefunction data.

Partial atomic charges were quantified using the Mulliken, Voronoi and Hirshfeld scales. These were calculated at the Gaussian optimised geometries using the ADF program, with the PBE functional, TZ2P basis sets[103-107] on all the atoms and the parameter controlling the integration grid set to 6.0. Mulliken charges were also calculated using the Gaussian code and Bader charges were taken from the AIMALLPro output. The 2009 ADF program was used for the silica systems and for the hydrazine linked systems with single metals in the +3 oxidation state whilst the 2010 ADF program was used for all other calculations. Test calculations found that altering the code had an insignificant effect on the results.

Methods of Quantifying the Energy of Combination of the BSRs with the H_2 Units

1. For the silica based systems[82] only, the enthalpy per H_2 unit of the reaction between a binding site representation (BSR) and n H_2 molecules was calculated as the difference in energy between the reactants and the products divided by the number of H_2 molecules, *i.e.* for

$$BSR + nH_2 \rightarrow BSR(H_2)_n$$

$$\Delta H_{H_2} = \frac{E_{BSR(H_2)_n} - E_{BSR} - nE_{H_2}}{n}$$

(25)

E for all species was taken as the SCF energies from the Gaussian optimisations, corrected with zero point energies and thermal corrections to 298 K.

The method of calculating the M–H_2 interaction energy evolved over time.

2. For the silica based systems the Ti(III)–H_2 interaction energies were calculated using the Ziegler-Rauk[136-139] energy decomposition scheme implemented in the ADF code using the Gaussian optimised geometries and the same calculation settings employed for the partial charges. This is also known as the Morokuma-type decomposition method. In this method a molecule may be split into fragments made up of groups of atoms. In this way the interaction between these fragments to form the whole molecule is separated from the interactions between all the atoms to form the whole molecule. Here the molecules were split into two fragments; the H_2 units and the rest of the molecule. Single point calculations were performed on the fragments at their geometries within the complete molecule and then the output files from these calculations were used as the basis for a calculation calculating the interaction energy between the fragments. The Ti(III)–H_2 interaction energy per H_2 unit was found by dividing by the number of H_2 units bound. The Ti(III)–H_2 interaction energies were corrected for basis set superposition error BSSE (~1 kJmol^{-1} per H_2 molecule bound) using the counterpoise method. As these BSSE were small they could be ignored in later calculations

3. The Ziegler-Rauk scheme requires the use of spin-restricted fragments. This is appropriate for the Ti(III) silica systems, for which the metal fragment has one unpaired electron, but not so for the V(III) and Cr(III)

silica species. For the latter, the average energy of interaction between the metal and the H_2 units was calculated in ADF as follows. Using the same calculation settings and the Gaussian optimised geometries, a spin-unrestricted single point calculation was performed. Two further single point calculations were then performed breaking the molecule into two fragments; the metal-containing fragment (spin-unrestricted) and the $(H_2)_n$ fragment (spin restricted). The average energy of interaction between the metal and the H_2 units was calculated as

$$E_{H_2}^{int} = \frac{E_{BSR(H_2)_n} - E_{BSR} - E_{(H_2)_n}}{n}$$

(26)

E for all species was taken as the SCF energies. In order to facilitate comparison, any silica Ti(III)–H_2 interaction energies quoted in the context of comparison with analogous V(III) and Cr(III) data were recalculated using the spin-unrestricted method.

4. The above method without using the Ziegler-Rauk scheme was used for the hydrazine linked systems with single metals in the +2 oxidation state[84, 86] and for all those with multiple metals.[85] For the hydrazine linked systems with single metals in the +3 oxidation state,[83] however, the method proved to be very occasionally unreliable, producing interaction energies which did not correlate well with H–H bond length and frequency data. In order to establish a more robust measure of the M(III)–H_2 interaction energies, the energy data obtained for all of the single metal +3 hydrazine linked systems with one H_2 unit bound to the metal centre, and for which there is a good correlation with H–H bond length and frequency, was plotted against the electron density at the QTAIM-derived bond critical point of the H–H bond. This is shown in figure 7. The exponential equation of the line of best fit from this graph was then used to extrapolate M(III)–H_2 interaction energies from the density at the BCP of the H–H bond for all of the mono-metallic hydrazine linked systems in the +3 oxidation state. The outlying point,

with a low bond critical point electron density, represents a rare occasion where a H_2 molecule was observed to bind with an elongated H–H bond. When multiple H_2 molecules were bound to one metal centre then an average of their extrapolated M(III)–H_2 interaction energies was taken.
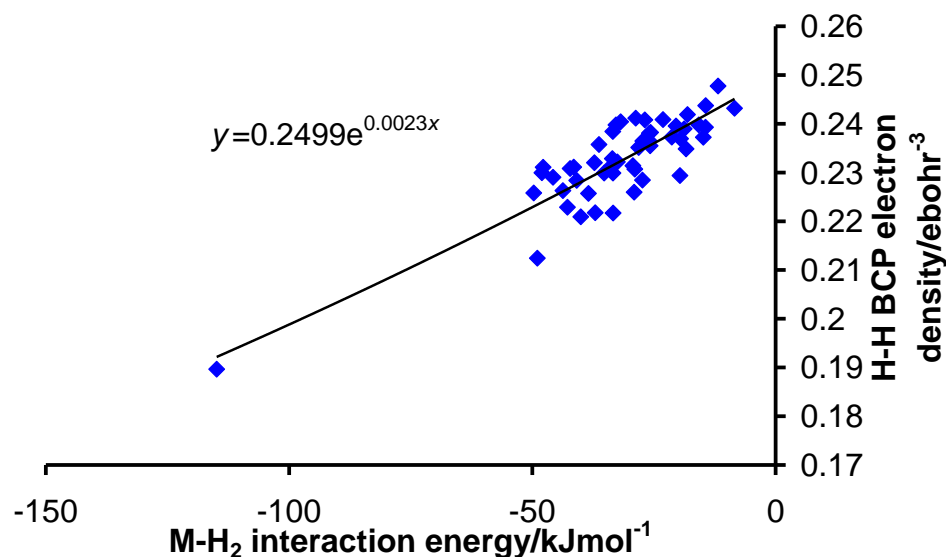
Figure 7: The electron density at the bond critical point (BCP) of the H–H bond when one H_2 unit is bound to the metal for all of the studied mono-metallic hydrazine linked systems with metals in the +3 oxidation state against the M(III)–H_2 interaction energy. The equation of the line of best fit is shown on the graph.

In summary, the combination of the BSRs with the H_2 units in the silica systems was studied using methods one, two (where possible) and three. All other M–H_2 interaction energies were studied using method three except for the monomeric hydrazine linked systems with early transition metals in the +3 oxidation state which were studied using method four.

Whilst searching for alternative structures with different metals and ligands it was found that there were multiple possible true minimum geometries for the same set of ligand, metal and number of bound H_2 units for the mono-metallic hydrazine linked systems in the +2 oxidation state. For example, with

Ti(II), a hydride ancillary ligand and one bound H_2, it is possible to converge several structures with a capped square planar geometry with different relative positioning of the ligands, and also a trigonal bipyramidal structure. These geometries are within 32 kJmol^{-1}. Due to the difficulty in locating all possible conformers (and as the geometry about the metal in the experimental system is not known) it was thought best to focus on a single conformer with one bound H_2 when making comparisons between metals and ligands. Therefore, all comparisons, in terms of the energy of the M(II)–H_2 interactions, are made with reference to the binding of one H_2 molecule in a standard molecular conformation. This conformer is not necessarily the global minimum for all combinations of ligands and metal but is a true minimum. The chosen conformers for each of the ligand sets are shown in figure 8.
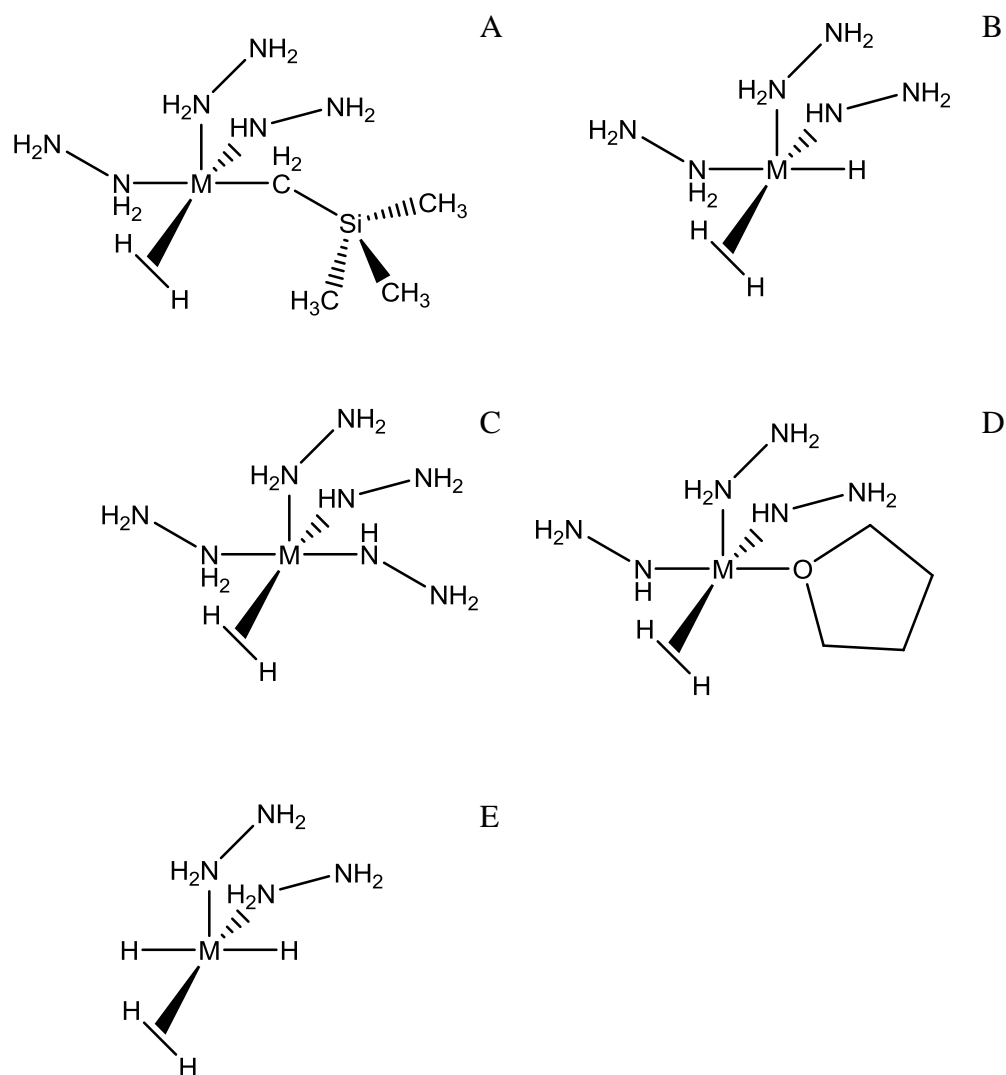
Figure 8: Schematic representations of the conformers chosen for binding the first H_2 unit to the mono-metallic hydrazine linked BSRs with metals in the +2 oxidation state, A, with a bis[(trimethylsilyl) methyl] ancillary ligand, B, with a hydride ancillary ligand, C, with only hydrazine based ligands, D, with a THF ancillary ligand and, E, with two hydride ancillary ligands.

<u>Results and Discussion</u>

Benchmarking the Results Against Experiment

Silica Based Systems[82]

Two binding site representations (BSRs) are required to model the silica based experimental material[73] as there are two types of benzyl-titanium binding site bound to the surfaces of the mesoporous silica in approximately a 50:50 ratio (Figure 3). One of these has one benzyl ligand bound to the Ti and the Ti is bound to the surface by two bonds and the other has a Ti with two benzyl ligands and one bond to the surface. It was decided to truncate the bulk solid at the oxygen atoms with H atoms to satisfy the oxygen valence and to include only one and two silicon atoms for the cases with one and two bonds to the surface respectively. This position seemed the most chemically intuitive whilst keeping the computational cost down to enable higher level calculations to be performed. The optimised geometries of the molecules used are shown in figures 9A and 9E for the single benzyl and dibenzyl binding sites respectively.
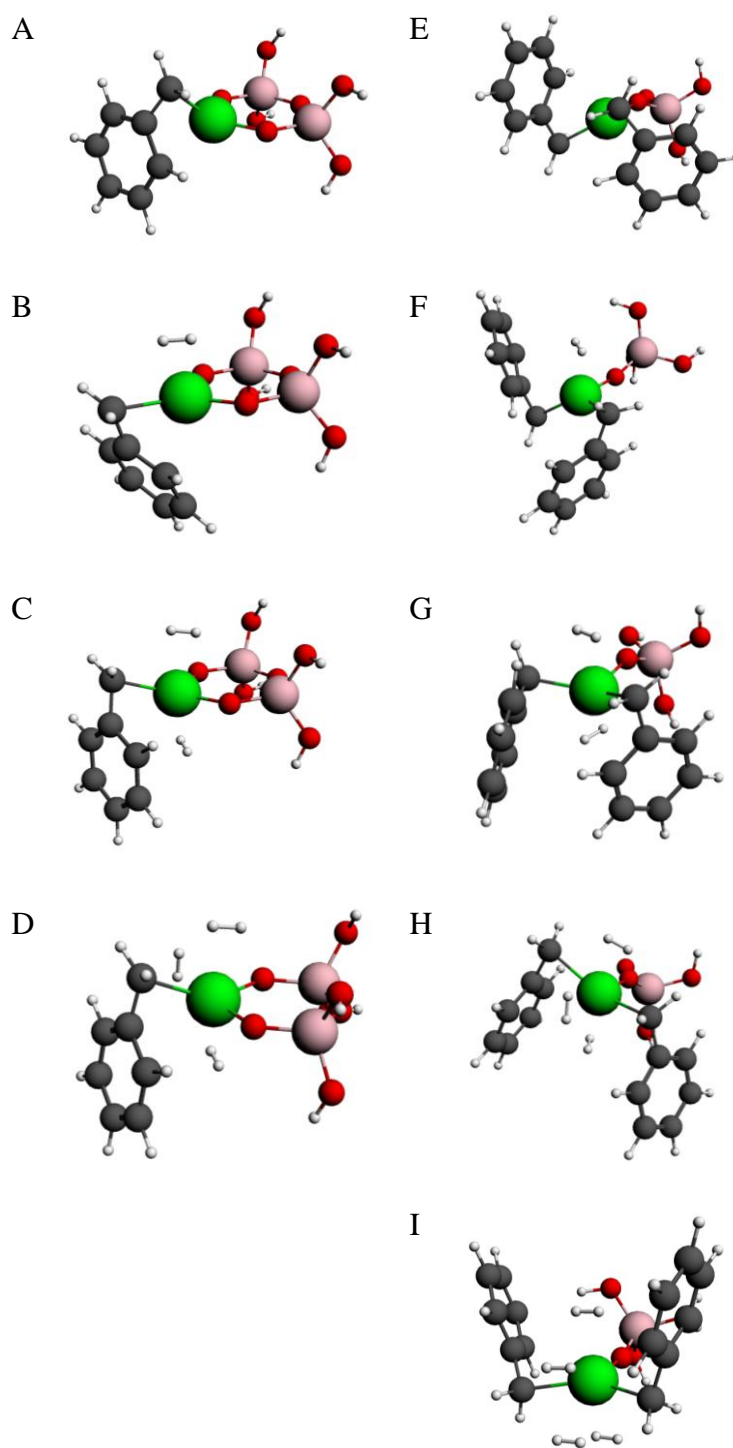
Figure 9: Ball and stick representations of the BSRs of the silica based system with one benzyl ancillary ligand with A zero, B one, C two and D three H_2 units bound. Ball and stick representations of the BSRs of the silica based system with two benzyl ancillary ligands with E zero, F one, G two, H three and I four H_2 units bound. Key: C black, H white, O red, Si pink, Ti Green.

Some of the bond lengths and angles were then fixed before binding H_2 units in order to better represent the nature of the rigid bulk structure. The bond lengths and angles selected were of the atoms from the silicon atoms onwards moving away from the Ti atoms. The inevitable consequence of this fixing approach is that some of the structures with H_2 bound have imaginary frequencies. These are generally few (no more than two), are small in magnitude (typically < 30i cm^{-1}) and all values are in appendix 1. All imaginary frequencies are isolated in the part of the molecules which are fixed prior to interaction with H_2.

Maxima of three and four H_2 units could be bound to the BSRs with one and two benzyl ligands respectively (Figure 9 D and I). This agrees well with the final experimental[74] maximum of 4.85 H_2/Ti as the computational value does not include any physisorbed H_2. From the ball and stick representations (Figure 9) it can be seen that the benzyl ligand gradually alters from a η^3 to a η^1 binding mode to accommodate the binding of the H_2 units.

The average Ti(III)–H_2 reaction enthalpies, ΔH_{H_2}, calculated using method one in the computational details (method 1), and interaction energies $E_{H_2}^{int}$ (method 2) are compared with the experimental hydrogen adsorption enthalpies in figure 10, from which it may be seen that the calculated reaction enthalpies do not agree very well with experiment. The experimental isosteric enthalpy only includes the interaction between the hydrogen and the material and not distortions of the material. The calculated enthalpy includes the distortion of the BSR and the H_2 molecules from their unbound equilibrium positions into their bound positions as well as the interaction energy between the metal and the hydrogen and the discrepancy between the experimental and theoretical values can be traced to these distortions. These distortions carry energy penalties which are larger than the energy recovered through the Ti(III)–H_2 interaction (Tables 1 and 2), and the calculated reaction enthalpies (method 1) are positive. The calculated Ti(III)–H_2 interaction energies (method 2) should agree better with experiment as they only include the interaction between the Ti and the H_2, which

60

they do, deviating by at most ca. 10 kJmol^{-1}. It is also notable that the Ti(III)–H$_2$ interaction energies generally increase as the number of H$_2$ units increases, as observed experimentally and in the previous computational studies of Zhao and co-workers[56] and Lee and co-workers[72] on the binding of H$_2$ to Sc-decorated fullerenes and Ti-C$_2$H$_2$ respectively. Due to the reaction enthalpies not being applicable for comparison with the experimental enthalpies only the metal to hydrogen molecule (M–H$_2$) interaction energies were probed during the later studies of the hydrazine linked systems.
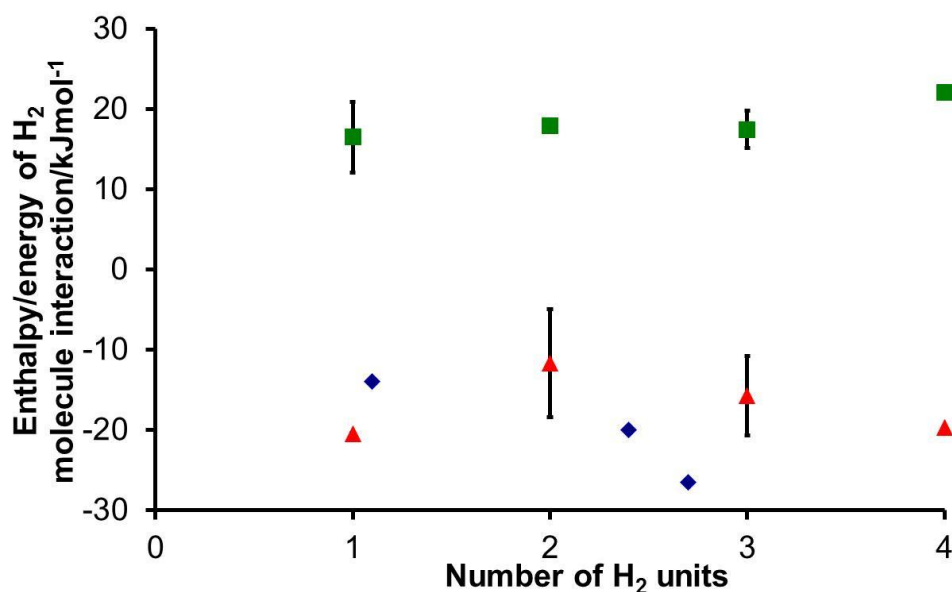
Figure 10: Comparison between the experimental hydrogen adsorption enthalpies[73] (blue) and the computational Ti(III)–H$_2$ interaction energies (red, method 2) and hydrogen adsorption enthalpies (green, method 1) for the silica based system. The experimental enthalpies are an average over all sites in the solid and were determined using the Clausius Clapeyron equation. The computational interaction energies and adsorption enthalpies are each an average over the two BSRs of the two types of binding site in the titanium silica based system and the error bars show the range of these values.

1	2	3	4	5	6	7	8	9	10	11
Number of bound H_2 units	Energy of free H_2 units	Energy of H_2 units bound to BSR	Difference in energy between bound and free H_2 units (Column 3 - 2)	Energy of the BSR without H_2 units bound	Energy of the BSR with H_2 units bound	Difference in energy between bound and unbound BSR (Column 6 - 5)	Energy of interaction between the BSR and the H_2 units	Sum of unbound energies (Column 2 + 5)	Sum of bound energies (Column 3 + 6 + 8)	Difference in energy between bound and unbound structures (Column 10 - 9)
1	-651.7	-649.1	2.61	-17064.9	-17031.3	33.6	-30.3	-17716.6	-17710.7	5.8
1	-651.7	-651.1	0.62	-17064.9	-17055.0	9.8	-9.7	-17716.6	-17715.8	0.8
2	-1303.3	-1301.9	1.49	-17064.9	-17030.5	34.4	-23.6	-18368.2	-18355.9	12.3
3	-1955.0	-1951.7	3.34	-17064.9	-17009.9	55.0	-42.4	-19019.9	-19003.9	16.0

Table 1: The breakdown of the fragment energies/kJmol[-1] of preliminary calculations (method 2) for the silica Ti(III) BSR with one benzyl ancillary ligand that represents half of the experimental system.[120]

1	2	3	4	5	6	7	8	9	10	11
Number of bound H_2 units	Energy of free H_2 units	Energy of H_2 units bound to BSR	Difference in energy between bound and free H_2 units (Column 3 - 2)	Energy of the BSR without H_2 units bound	Energy of the BSR with H_2 units bound	Difference in energy between bound and unbound BSR (Column 6 - 5)	Energy of interaction between the BSR and the H_2 units	Sum of unbound energies (Column 2 + 5)	Sum of bound energies (Column 3 + 6 + 8)	Difference in energy between bound and unbound structures (Column 10 - 9)
1	-651.7	-648.9	2.8	-22230.7	-22204.4	26.3	-33.7	-22882.4	-22887.0	-4.6
2	-1303.3	-1300.3	3.0	-22230.7	-22170.6	60.1	-46.2	-23534.0	-23517.1	16.9
3	-1955.0	-1948.1	6.9	-22230.7	-22138.9	91.8	-74.5	-24185.7	-24161.6	24.1
4	-2606.7	-2574.9	31.8	-22230.7	-22120.8	109.9	-92.4	-24837.4	-24788.0	49.4

Table 2: The breakdown of the fragment energies/kJmol^{-1} of preliminary calculations (method 2) for the silica Ti(III) BSR with two benzyl ancillary ligands that represents half of the experimental system.[120]

The Hydrazine Linked V(III) System[83]

One BSR has been selected to represent the V(III) hydrazine linked experimental material[78] that best mirrored the known experimental results. The hydrazine linked gels are amorphous and X-ray photoelectron spectroscopy measurements revealed that a tetrahydrofuran (THF) ligand is bound to each V(III) (high intensity emissions centred at 530.4 eV in the oxygen region) but the coordination number about the V(III) is not known experimentally.[78] To begin with, four and five coordinate BSRs were modelled with the bulk truncated with H atoms. Again a chemically sensible point was selected with complete hydrazine based ligands, which maintain the oxidation state of the V(III). In this way each V(III) has three formally negative hydrazide ligands (NHNH$_2$) with the rest of the coordination made up with formally neutral hydrazine ligands (NH$_2$NH$_2$). A three coordinate geometry that maintains the oxidation state of the V is not possible, as the THF ligand is formally neutral, and a six coordinate geometry was thought unlikely. The optimised geometries are shown in figure 11. No fixing was thought to be required before H$_2$ molecules were bound as the gels are not as rigid as the mesoporous silica and therefore there is the potential for greater movement of the ligands about the metals.
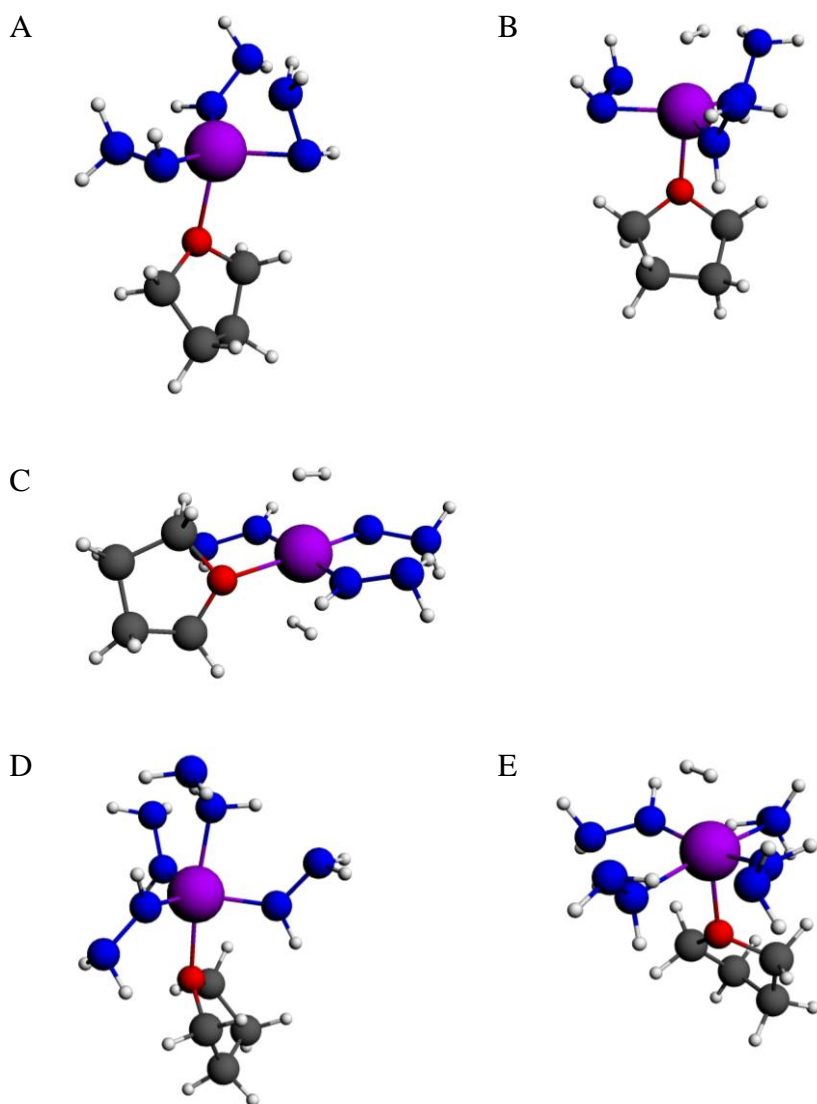
Figure 11: Ball and stick representations of a four coordinate hydrazine linked V(III) BSR with a THF ancillary ligand with A zero, B one and C two H_2 units bound, and a five coordinate BSR with D zero and E one H_2 unit bound. Key: C black, H white, O red, N blue, V purple.

Experimentally a rising binding enthalpy with increasing hydrogen coverage up to -36 kJmol^{-1} was observed and a maximum of 1.96 H_2/V was found to bind.[78] For the four coordinate BSR a maximum of two H_2 units could be bound to each V and the V(III)–H_2 interaction energy (method 4) rose from -17.88 to -19.30 kJmol^{-1} when binding one and two H_2 units respectively.

Although the absolute values of the V(III)–H_2 interaction energies are lower than those of the experiment they do show the correct rising trend. The four coordinate BSR was selected over the five coordinate to represent the experiment as the five coordinate BSR could only bind one H_2 unit and the enthalpy of binding was lower (-11.86 kJmol^{-1}). It was concluded that most of the binding sites in the experimental gel are likely to be four coordinate.

The Hydrazine Linked Cr(II) System[84]

Two BSRs were selected to represent the Cr(II) hydrazine linked experimental material[77] one each for before and after hydrogenation. Before hydrogenation each binding site has a bis[(trimethylsilyl)methyl] ancillary ligand bound and after hydrogenation this is replaced with a hydride ancillary ligand. Again the coordination number about the Cr(II) metals is not known experimentally[77] and therefore three, four and five coordinate BSRs were initially modelled to see which best represented the experimental data. The BSRs were truncated from the bulk in the same way as the V(III) BSRs. As hydride and bis[(trimethylsilyl)methyl] ligands are both formally negative each Cr(II) had one hydrazide ligand bound to it to maintain the oxidation state of the Cr(II) and the rest of the coordination spheres were made up with hydrazine ligands. The optimised three, four and five coordinate BSR geometries are shown in figures 12A, 13A and 14A respectively.
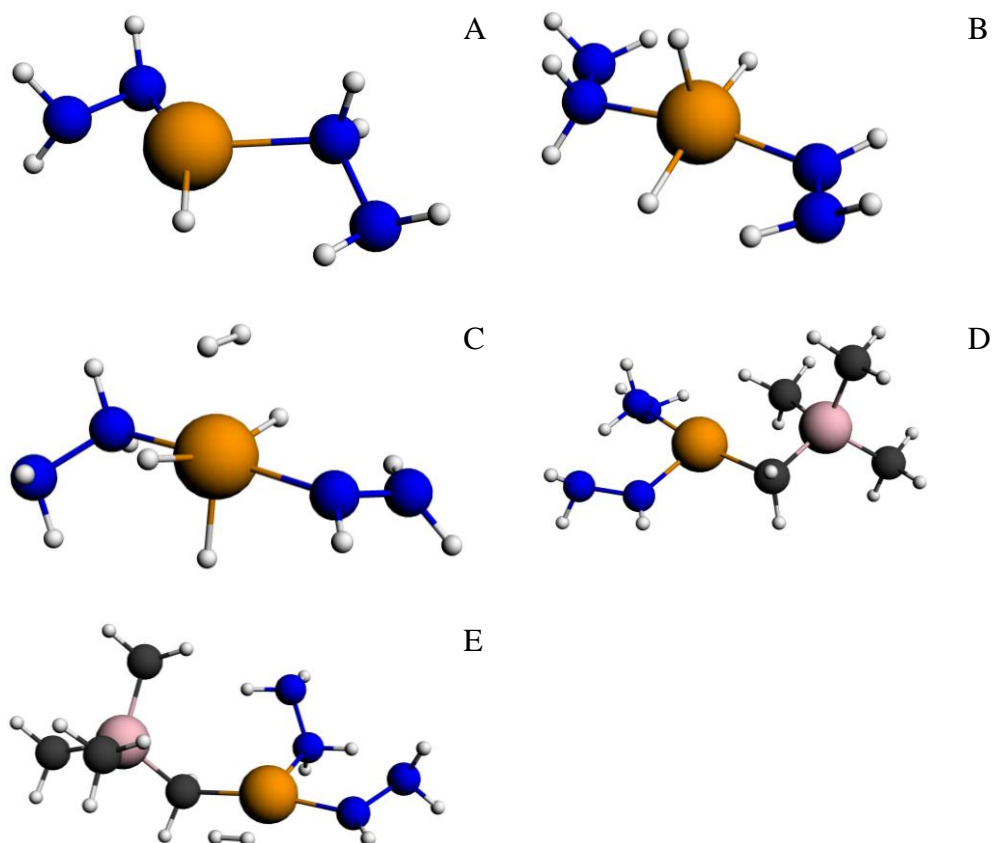
Figure 12: Ball and stick representations of a three coordinate hydrazine linked Cr(II) BSR with a hydride ancillary ligand with, A, zero, B, one and, C, two H_2 units bound and a bis[(trimethylsilyl) methyl] ancillary ligand with, D, zero and, E, one H_2 unit bound. Key: C black, H white, N blue, Si pink, Cr orange.
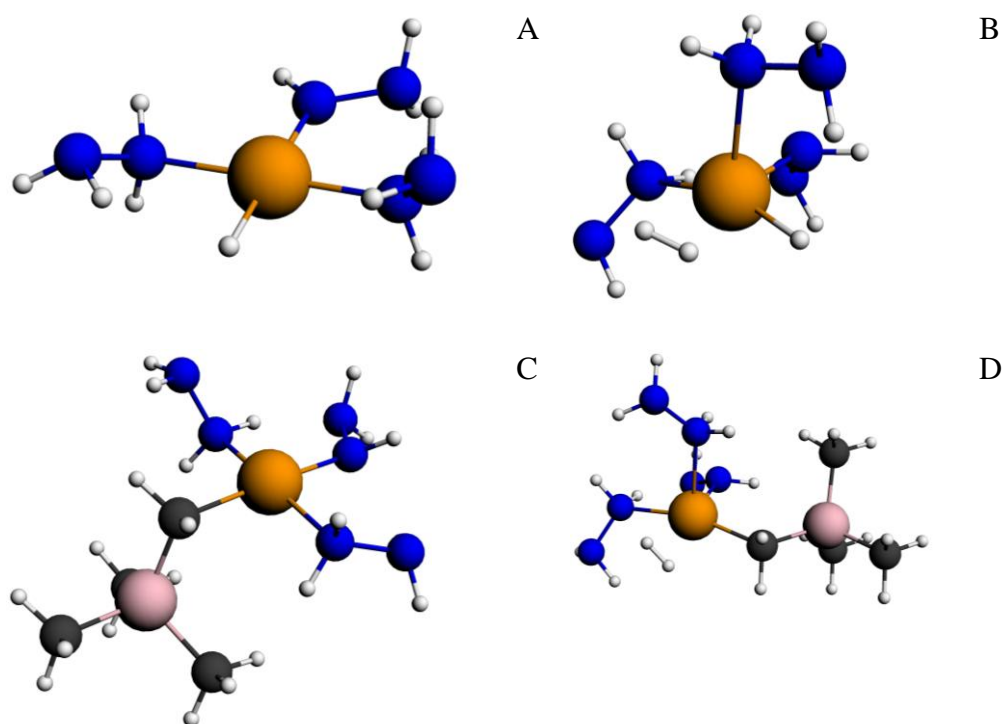
Figure 13: Ball and stick representations of a four coordinate hydrazine linked Cr(II) BSR with a hydride ancillary ligand with, A, zero and, B, one H_2 unit bound and a bis[(trimethylsilyl) methyl] ancillary ligand with, C, zero and, D, one H_2 unit bound. Key: C black, H white, N blue, Si pink, Cr orange.
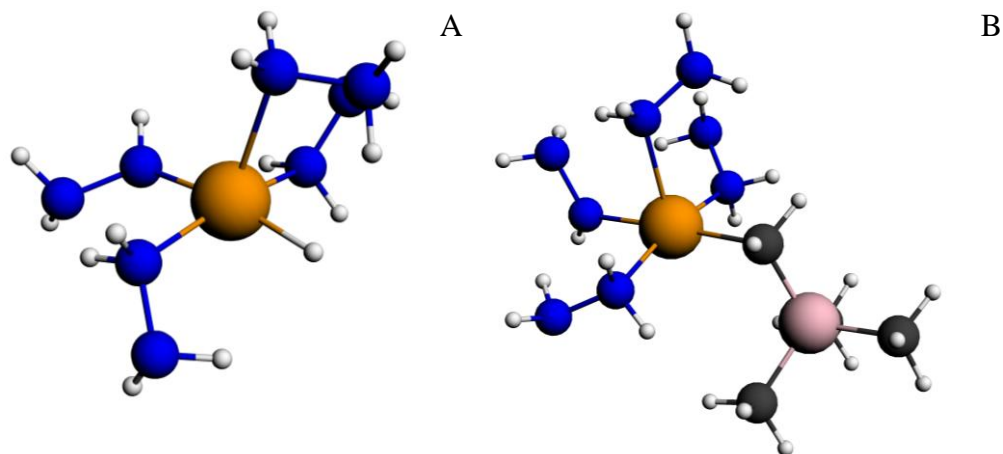
Figure 14: Ball and stick representations of a five coordinate Cr(II) BSR with, A, a hydride ancillary ligand with zero H_2 units bound and, B, a bis[(trimethylsilyl) methyl] ancillary ligand with zero H_2 units bound. Key: C black, H white, N blue, Si pink, Cr orange.

Experimentally the material with a bis[(trimethylsilyl)methyl] ligand showed a rising hydrogen adsorption enthalpy up to -17.86 kJmol^{-1} whilst that with a hydride ligand showed a rising enthalpy up to -51.58 kJmol^{-1}. This is an increase in maximum enthalpy of -33.72 kJmol^{-1}. A maximum of 1.75 H_2/Cr could be bound.[77] Out of the proposed coordination numbers five coordinate was discounted immediately, as it did not bind any H_2 units and the three coordinate was also discounted as the first H_2 unit bound only as two hydride ligands. Binding as hydride ligands suggests that the binding would be irreversible and the hydrogen adsorption observed experimentally was fully reversible. The four coordinate BSRs with a bis[(trimethylsilyl)methyl] ancillary ligand bind one H_2 unit with an energy of -28.33 kJmol^{-1}, rising to -48.52 kJmol^{-1} with a hydride ancillary ligand (method 3). This rise in enthalpy upon altering the ancillary ligand (-20.19 kJmol^{-1}) is in reasonable agreement with experiment. Only binding one H_2 unit to the four coordinate BSRs is also in reasonable agreement with the experimental value as H_2 physisorbed within the gel is not accounted for in the model. It was concluded that as for the V(III) hydrazine linked system that most of the binding sites in the solid were four coordinate and therefore only four coordinate binding sites were studied further.

Benchmarking the Kubas Interaction[83]

In order to allow a comparison between the values found for the studied systems and those of classically Kubas systems (systems where it is agreed in the literature that the H_2 molecule is binding through the Kubas interaction) some classically Kubas first row transition metal molecules[140-142] were selected and modelled with the same computational model as the BSRs of the experimental system using method 3 to calculate the M–H_2 interaction energies. The molecules selected were $Co(CO)_2(NO)(H_2)$, $Fe(CO)(NO)_2(H_2)$ and $Cr(CO)_5(H_2)$ (Figure 15) and the metrics for these systems are shown in table 3.
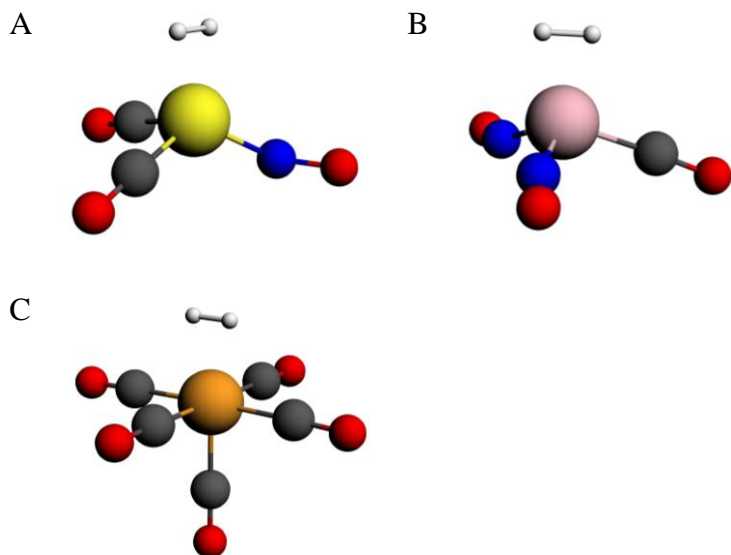
Figure 15: Ball and stick representations of classically Kubas systems: A $Co(CO)_2(NO)(H_2)$, B $Fe(CO)(NO)_2(H_2)$ and C $Cr(CO)_5(H_2)$. Key: C black, H white, O red, N blue, Co yellow, Fe pink, Cr orange.

Compound	Experimental H–H stretching frequency/cm^{-1}	Computational H–H stretching frequency/cm^{-1}	Computational H–H bond length/Å	Computational M–H$_2$ interaction energy/kJmol^{-1}	Computational electron density at the BCP of the H–H bond/ebohr^{-3}	Computational Laplacian at the BCP/ebohr^{-5}
Co(CO)$_2$(NO)(H$_2$)	3100/2976[140]	3098	0.839	-75.96	0.210	-0.631
Fe(CO)(NO)$_2$(H$_2$)	2973[140]	2868	0.860	-93.30	0.202	-0.607
Cr(CO)$_5$(H$_2$)	3030[141]	3164	0.830	-67.85	0.219	-0.694
H$_2$	4161[142]	4316	0.752	N/A	0.256	-1.013

Table 3: Experimental and computational H–H bond length and stretching frequencies, M–H$_2$ interaction energies (method 3) and electron densities and Laplacians at the BCPs of classically Kubas molecules and H$_2$.

Experimentally the Kubas interaction of a metal with a H_2 molecule is characterised by a lengthening of the H–H bond without breakage and a reduction in its stretching frequency upon binding. This was seen experimentally for the classically Kubas systems and has been reproduced computationally (Table 3). Quantum Theory of Atoms in Molecules (QTAIM) calculations were also carried out on these systems to provide benchmarking values for the H–H bond critical point (BCP), electron density and Laplacian. The electron density at the BCP is proportional to the strength of the bond and negative Laplacians at BCPs indicate that the bond is covalent. As expected, the electron density at the H–H BCP is smaller and the Laplacian is less negative for the classically Kubas systems compared to the H_2 molecule due to the H–H bond weakening and becomes less covalent upon binding (Table 3). The QTAIM results could not be compared with other computational values as to the best of my knowledge this is the first QTAIM analysis of the Kubas interaction.
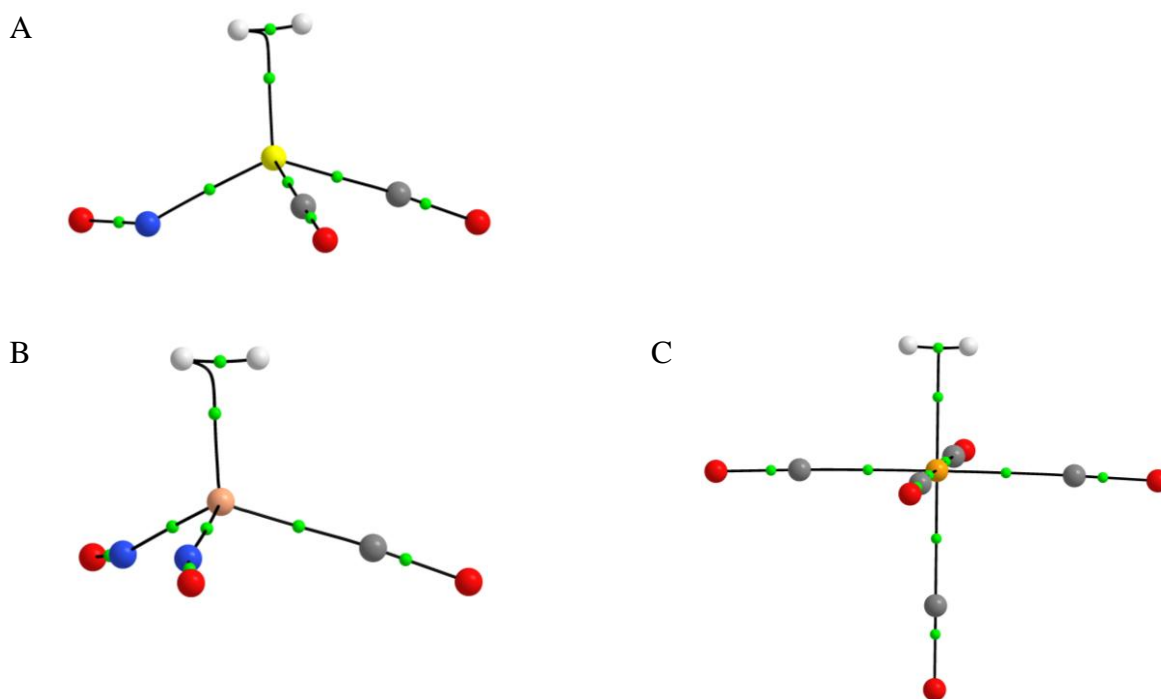
Figure 16: Molecular graphs of A $Co(CO)_2(NO)(H_2)$, B $Fe(CO)(NO)_2(H_2)$ and C $Cr(CO)_5(H_2)$ showing the bond paths (lines) and the different critical points: nuclear (colour-coded by element: C black, H white, O red, N blue, Co yellow, Fe pink, Cr orange), bond (small green dots).

Molecular graphs showing the BCPs and bond paths for the classically Kubas molecules are shown in figure 16. It might be expected that, for a Kubas interaction between the H_2 unit and the metal, there would be a bond path between the H atoms and from each H atom to the metal, and a ring critical point (RCP) at the centre of the triangle formed by these bond paths. However, the RCP and one of the bond paths from one of the H atoms to the metal are missing in the present systems due to a "bond catastrophe", which occurs when a RCP and BCP are so close to each other that they coalesce, cancelling each other out. This has been observed previously by Sparkes for the analogous Dewar-Chatt-Duncanson interaction of a C=C double bond and a metal.[119]

Initially it was thought that there may have been a relationship between the shape of the remaining M–H bond path and the balance of the π and σ components of the Kubas M–H_2 interaction. The bond path, as noted earlier, follows the path of maximum electron density between two atoms. As can be seen in the molecular graphs (Figure 16), the M–H bond path, instead of going directly from the M to the single H atom, follows a path to the centre of the H–H bond before curving off towards the H atom. It was thought that this indicated that the overall M–H_2 interaction was dominated by the σ component and that the extent to which the bond path deviated from this line depends on the magnitude of the π component of the bond.[83] However, later calculations on the M(II) hydrazine linked systems[84] showed that the change in the partial charge on the metal, which indicates the extent of the M–H_2 interaction's σ versus π component, did not follow this hypothesis. The electron density is very flat in that area, as indicated by the occurrence of a bond catastrophe, so small changes in the electron density may affect the bond path and therefore it seems unlikely that alterations in the bond path are indicative of changes in the bonding in this case. Matta and Boyd[143] are also vague about what the curvature of a bond path means stating that it shows the bonding to be strained.

The relationship between the density at the BCP, the Laplacian and the length of the H–H bond has been probed, in order to establish how far the H–H

bond can be stretched whilst maintaining a QTAIM-defined covalent interaction between the H atoms, and thus the maximum H–H distance of a Kubas type bond. The $Cr(CO)_5(H_2)$ molecule was taken as the target for this study, and the length of the H–H bond was increased incrementally in a series of single point calculations. Figure 17 plots the electron density at the BCP against bond length for the H–H bond. The equation for the relationship is shown on this graph, and shows that the density at the BCP depends on the exponential of a second order polynomial of the H–H bond length, implying that the M–H_2 interaction energy has a similar dependence. Interestingly an analogous plot of the Laplacian against the H–H bond length for the same example molecule (Figure 18) crosses the H–H bond length axis at 1.5 Å, showing that beyond this distance the H–H bond is no longer covalent, and a BCP is no longer located once the bond is over 1.75 Å, showing that there is no longer a H–H interaction. 1.5 − 1.75 Å could be considered the range over which the interaction changes from Kubas to a di-hydride interaction with a broken H–H bond. This agrees rather well with the suggestion of Kubas[33] that the M–H_2 interactions characterised as di-hydrides have a H–H distance greater than 1.6 Å.

The graph shows the relationship with the equation $y = \exp(0.4005x^2 - 2.8595x + 0.5579)$, with the y-axis labeled "Electron Density at the BCP/ebohr^{-3}" and x-axis labeled "H-H Bond length/Å".
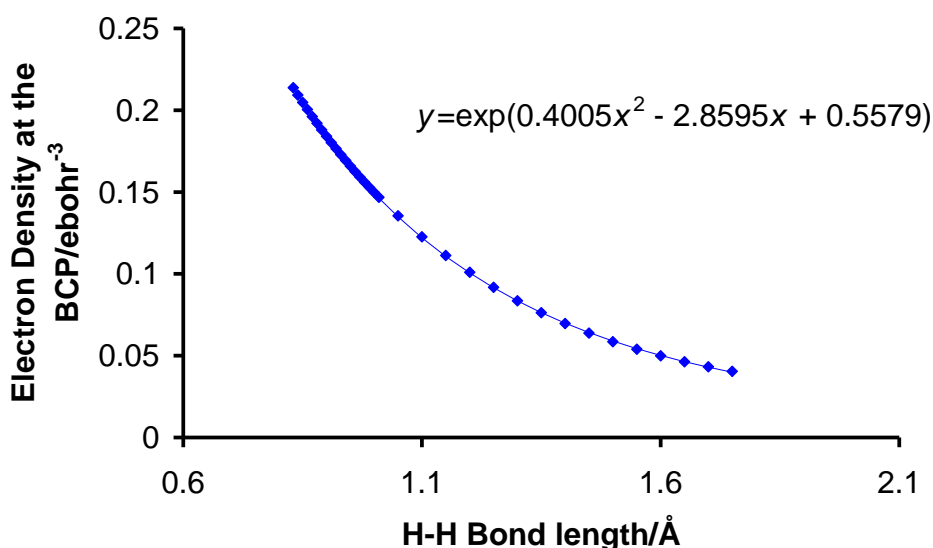
Figure 17: The electron density at the BCP against bond length for the H–H bond in the $Cr(CO)_5(H_2)$ system.
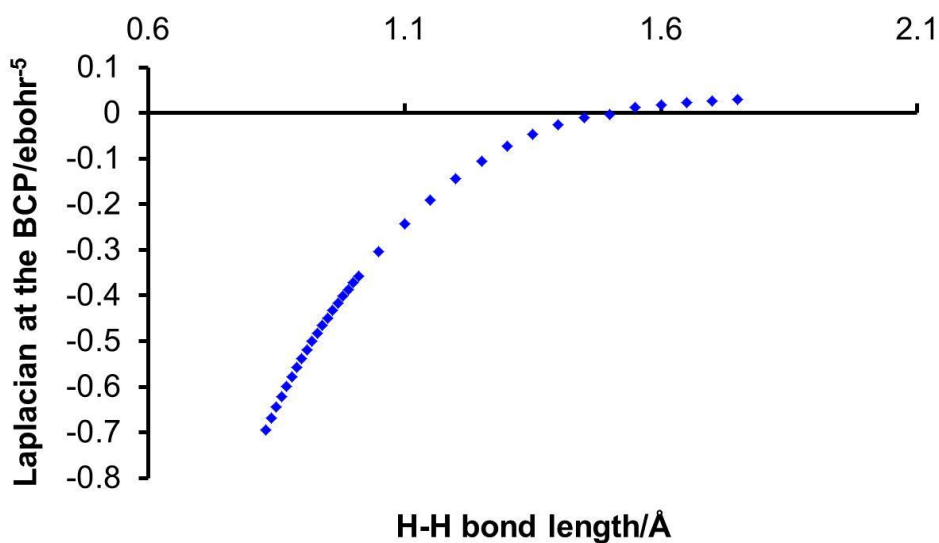
Figure 18: The Laplacian at the BCP against the bond length for the H–H bond in the $Cr(CO)_5(H_2)$ system.

The Nature of the M–H₂ Interaction

One of the most important questions that arose from the experimental research was whether or not the experimentally observed high hydrogen binding enthalpies were caused by the H_2 molecule binding to the metals through the Kubas interaction, as the nature of the materials made experimental confirmation of this difficult. Evidence for the Kubas interaction was therefore sought in the computational results. In the silica system[82] on binding to titanium, the H–H bond length is between 0.77 – 0.79 Å, and the H–H stretching frequency is between 3635 – 3966 cm⁻¹. In the hydrazine linked V(III) system[83] the H–H bond length and H–H stretching frequency values are 0.785 – 0.787 Å and 3726 – 3764 cm⁻¹ respectively and in the hydrazine linked Cr(II) system[84] they are 0.784 Å and 3783 cm⁻¹ respectively with a bis[(trimethylsilyl)methyl] ligand and 0.811 Å and 3377 cm⁻¹ respectively with a hydride ligand. None of the bond lengths are as long as those of the classically Kubas systems[83] (0.830 – 0.860 Å, Table 3) nor are the stretching frequencies as low (2868 – 3164 cm⁻¹, Table 3) but all show a lengthening in H–H bond length and a decrease in stretching frequency from the

H$_2$ molecule free values of 0.752 Å and 4315 cm^{-1}. All values are shown in appendix 1.

A QTAIM analysis was performed only on the hydrazine linked systems. The densities at the BCPs of the H–H bonds for the Cr(II) system are 0.239 and 0.225 ebohr^{-3} with bis[(trimethylsilyl)methyl] and hydride ancillary ligands respectively and for the V(III) system are between 0.238 – 0.240 ebohr^{-3}. These values are all higher than those of the classically Kubas systems (0.202 – 0.219 ebohr^{-3}, Table 3) but are lower than the H$_2$ molecule free value of 0.256 ebohr^{-3}. The Laplacians at the BCPs for the Cr(II) system are -0.878 and -0.774 ebohr^{-5} with bis[(trimethylsilyl)methyl] and hydride ancillary ligands respectively and for the V(III) system are between -0.873 – -0.886 ebohr^{-5}. In a similar fashion these values are all lower than those of the classically Kubas systems (-0.607 – -0.694 ebohr^{-5}, Table 3) but are higher than the H$_2$ molecule free value of -1.013. All values are shown in appendix 1. The molecular graphs of the models of the experimental systems (Figures 19 and 20) show bond path shapes between the metal and the H$_2$ molecule that are very similar to those of the classically Kubas systems. They also show that a bond catastrophe has occurred.
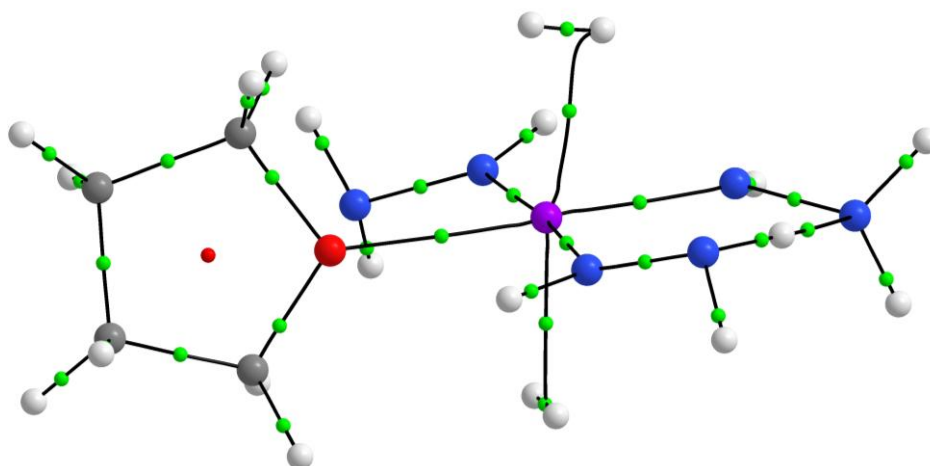
Figure 19: Molecular graph of a four coordinate V(III) BSR with a THF ancillary ligand and two H$_2$ units bound showing the bond paths (lines) and the different critical points: nuclear (colour-coded by element: C black, H white, O red, N blue, V purple), bond (small green dots), ring (small red dot).

A

B
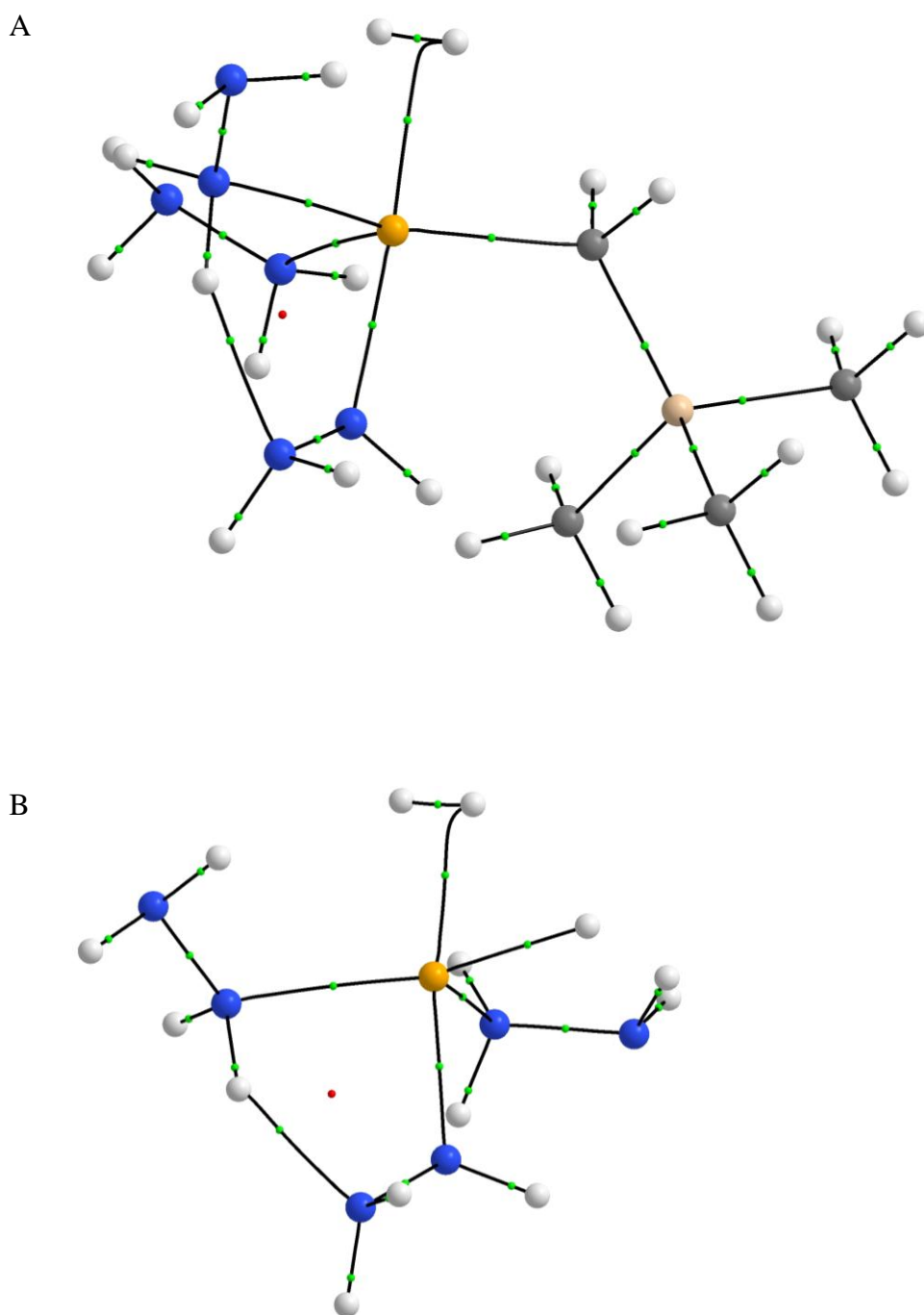
Figure 20: Molecular graphs of a four coordinate Cr(II) BSR with one H_2 unit bound and, A, a bis[(trimethylsilyl)methyl] ancillary ligand and, B, a hydride ancillary ligand showing the bond paths (lines) and the different critical points: nuclear (colour-coded by element: H white, N blue, Cr orange, Si pink), bond (small green dots), ring (small red dots).

A molecular orbital (MO) analysis was also carried out on the models of the computational systems to look for the two components of the Kubas interaction, the σ-donation from the H_2 molecule's σ-bonding orbital to a d orbital on the metal and the π-back-donation from the metal to the σ^* anti-bonding orbital of the H_2 molecule. Orbitals representing these two interactions were observed in all of the experimental systems (Figures 21 – 23).
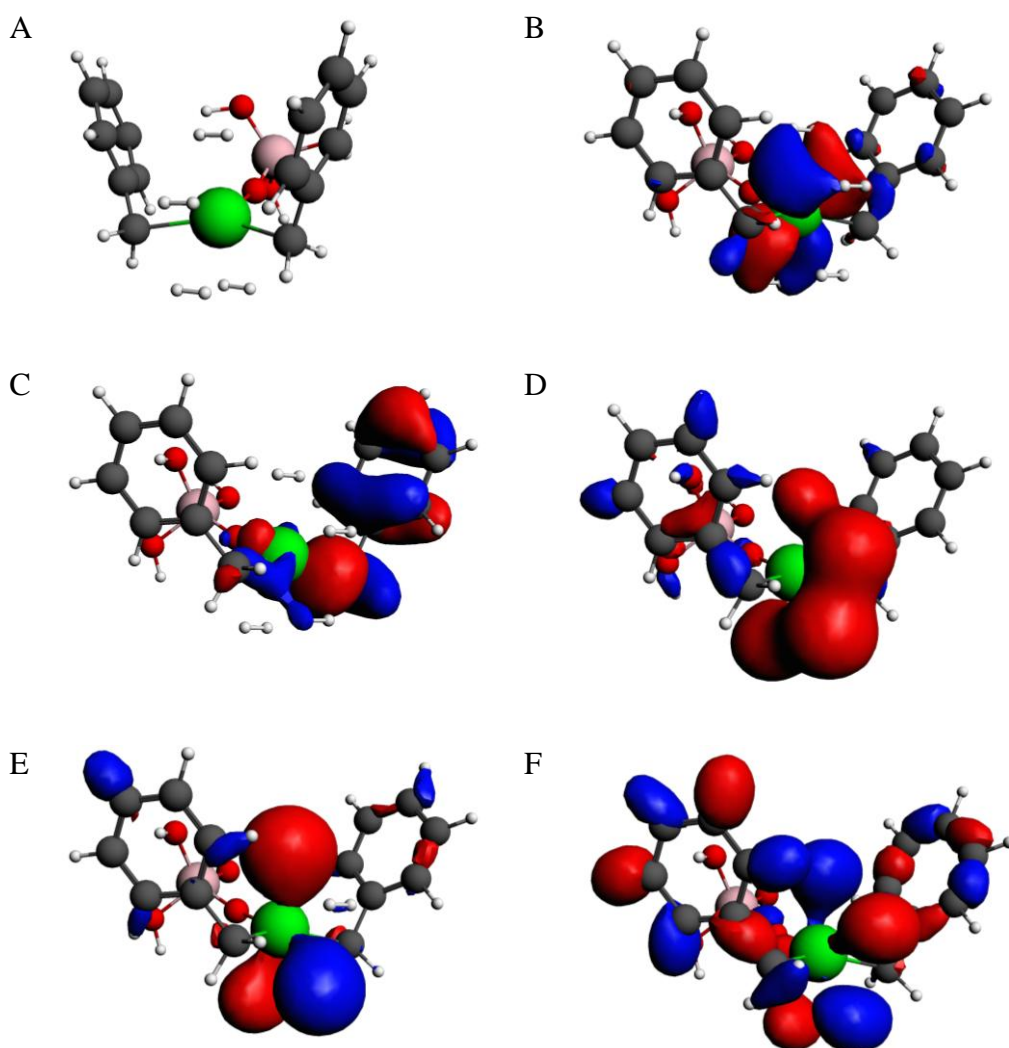
Figure 21: Three dimensional molecular orbitals of the silica based Ti(III) BSR with two benzyl ancillary ligands and four H_2 units bound showing; A, (bare molecule), B, HOMO (π-back-donation), C, HOMO-1 (π-back-donation), D, HOMO-39 (σ-donation), E, HOMO-33 (σ-donation) and, F, HOMO-31 (σ-donation).[82]
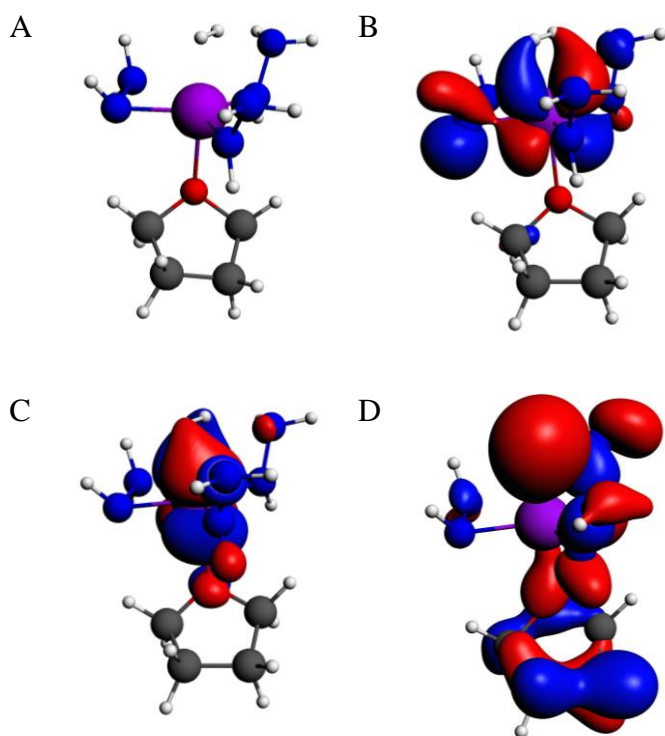
Figure 22: Three dimensional molecular orbitals of the four coordinate hydrazine linked V(III) BSR with a THF ancillary ligand with one H_2 unit bound showing; A, (bare molecule), B, HOMO (π-back-donation), C, HOMO-1 (π-back-donation), and, D, HOMO-34 (σ-donation).
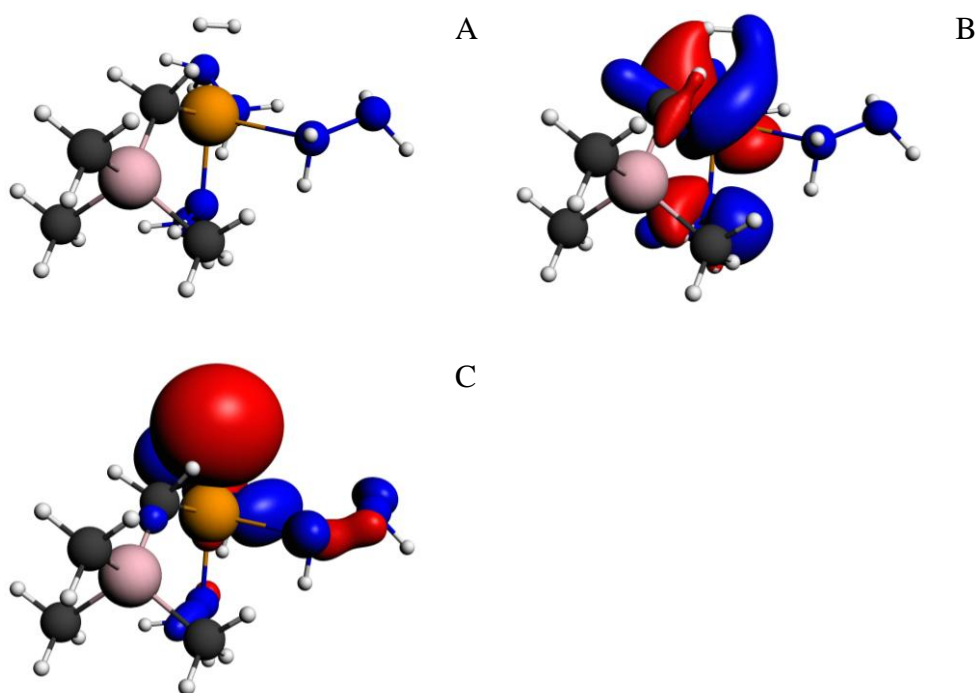
Figure 23: Three dimensional molecular orbitals of the four coordinate hydrazine linked Cr(II) BSR with a bis[(trimethylsilyl) methyl] ancillary ligand with one H_2 unit bound showing; A, (bare molecule), B, HOMO-1 (π-back-donation) and, C, HOMO-44 (σ-donation).

In all of the computational models upon binding to the metal the H–H bond is seen to lengthen, its stretching frequency is shown to reduce and, where studied, the electron density and Laplacian at the BCPs are seen to reduce and become less negative respectively, the molecular graphs are similar to those of classically Kubas systems and orbitals may be observed for the σ and π components of the Kubas interaction. This evidence does not confirm that the H_2 is binding through the Kubas interaction in the experimental systems but certainly strongly suggests that it is. It corroborates the experimentally determined hydrogen binding enthalpies being of the right order for the Kubas interaction, and the Raman study on a similar polymeric system with V(III) binding sites[80] which showed a H–H stretch lower than that of free H_2 and comparable to an IR stretch seen for the classically Kubas system $W(CO)_3(PCy_3)_2(\eta^2\text{-}H_2)$.[81] In summary, as the properties of the H–H bond of the

bound H_2 does not alter as much as in the classically Kubas systems, the interaction may be classified as a weak Kubas interaction. (The presence of the Kubas interaction could be confirmed experimentally using inelastic neutron scattering experiments to observe the H_2 molecules rotational transitions that are not seen in hydrides. These experiments have not yet been performed.)

Altering the Ancillary Ligand

Silica Based Systems[82]

The benzyl ancillary ligand of the computational model of the silica based system was altered to allyl, methyl or hydride to see what effect making the ligand smaller could potentially have if attempted with the experimental system. The maximum number of H_2 units which can be bound to the Ti when the benzyl ancillary ligands are replaced by hydride, methyl or allyl is two, two and three respectively for the BSR with one ancillary ligand, and four to all of the BSRs with two ancillary ligands (Figure 24).
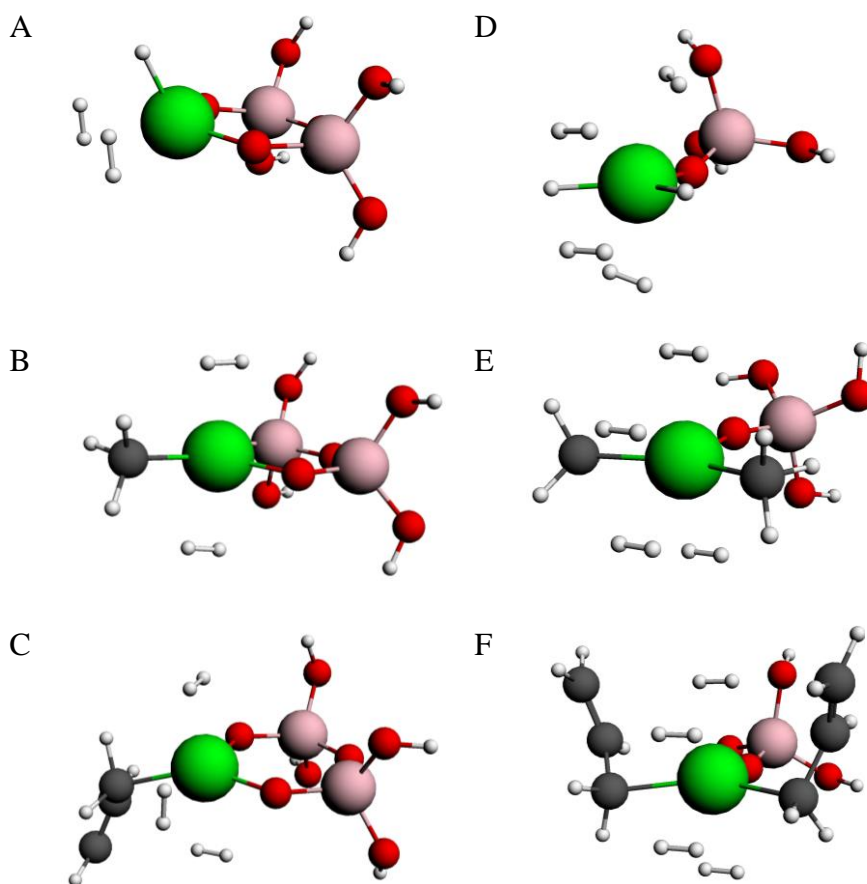
Figure 24: Ball and stick representations of the BSRs of the silica based system with, A, one hydride ancillary ligand and two H_2 units bound, B, one methyl ancillary ligand and two H_2 units bound and, C, one allyl ancillary ligand and three H_2 units bound. Ball and stick representations of the BSRs of the silica based system with four H_2 units bound with, D, two hydride, E, two methyl and, F, two allyl ancillary ligands.
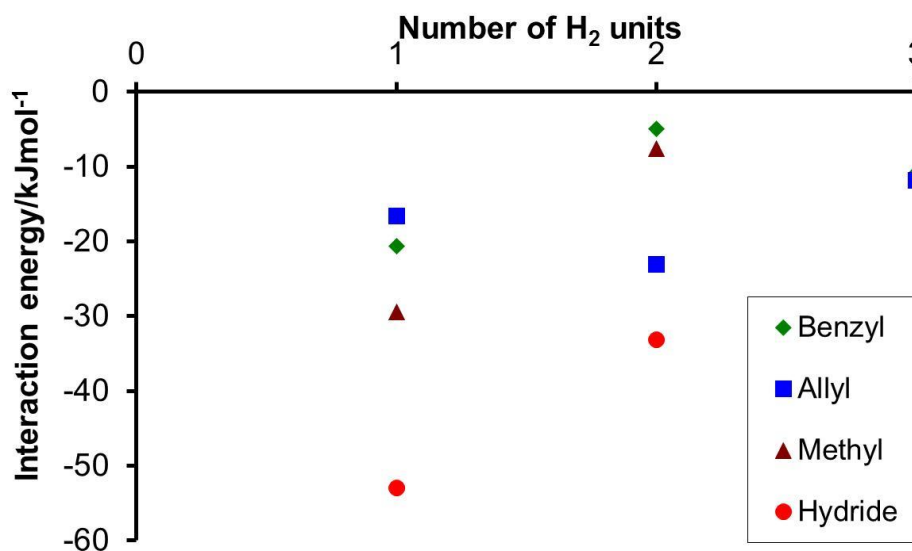
Figure 25: The Ti(III)–H_2 interaction energy (method 3) as a function of the number of H_2 units bound for the BSR of the silica based system with one varied ancillary ligand.
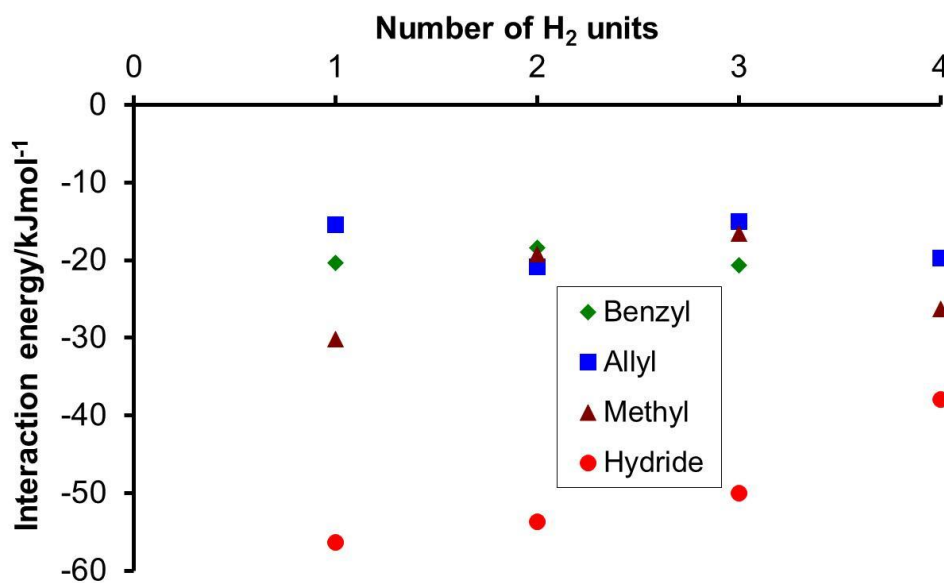
Figure 26: The Ti(III)–H_2 interaction energy (method 3) as a function of the number of H_2 units bound for the BSR of the silica based system with two varied ancillary ligands.

The Ti(III)–H_2 interaction energies (method 3) when one H_2 unit is bound decrease for both BSRs in the order hydride > methyl > benzyl > allyl (Figures 25 and 26).

When more than one H_2 unit is bound it is generally the case that the Ti(III)–H_2 interaction energies are by far the largest for the hydride compounds, with some variations in the ordering of the other ancillary ligands. Hydride < methyl < benzyl < allyl is the order of increasing ability of the ligand to π-accept electron density.

The Hydrazine Linked V(III) System[83]

With the hydrazine linked V(III) system the ancillary ligand was varied computationally from THF to hydride, 1,3-dimethylallyl, (trimethylsilyl)methyl, two hydrides and to a BSR without a non-hydrazine based ligand. (Trimethylsilyl)methyl and 1,3-dimethyl allyl were studied because these alkyl groups have been used to stabilise low coordinate transition metal complexes[144] and it was anticipated that, in future experimental studies on related hydrazides, synthetic routes using precursors with these ligands would lead to hydrazide products with a small amount of these ligands in the final structure. Hydride was included because if hydrogenation of the metal–alkyl bond to eliminate these residual ligands was carried out experimentally it would leave the hydride behind in the structure. Changing from THF to an alkyl, hydride or allyl ligand involved conversion of a hydrazide to a neutral hydrazine ligand in order to preserve the oxidation state of the metal and when changing to two hydride ancillary ligands a hydrazide ligand was replaced by a hydride.

A maximum of two H_2 units can be bound to the BSRs with all of the studied ancillary ligands except for two hydride ligands where a maximum of three H_2 units may be bound. The V(III)–H_2 interaction energies (method 4) with one H_2 unit bound as a function of ligand were investigated (Figure 27). The interaction energies are highest when the coordination sphere contains two hydride ligands, and a single hydride ligand also gives a high V(III)–H_2

interaction energy. The V(III)–H$_2$ interaction energies of the other ligands are similar to each other.
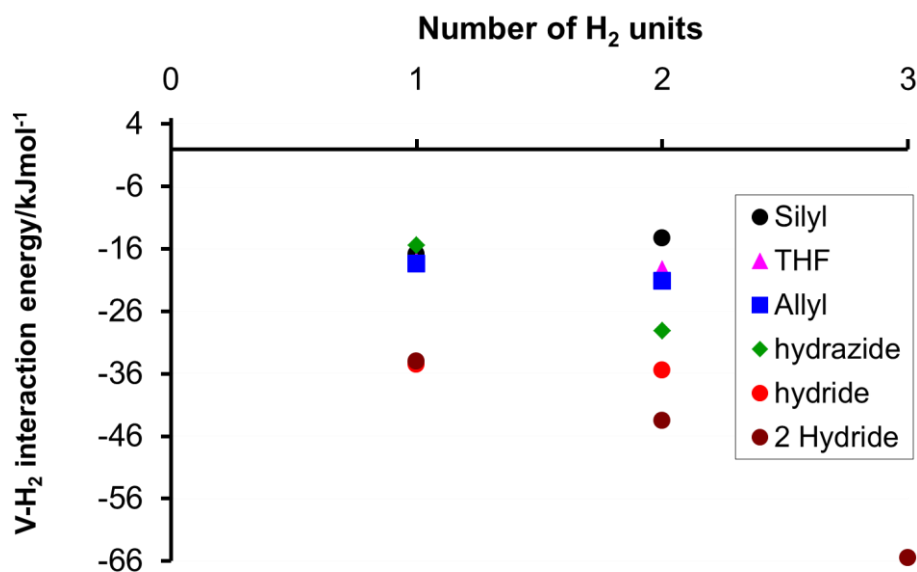
Figure 27: The V(III)–H$_2$ interaction energy (method 4) as a function of the number of H$_2$ units bound for hydrazine linked four coordinate BSRs with two varied ancillary ligands.

The Hydrazine Linked Cr(II) System[84]

With the hydrazine linked Cr(II) system the ancillary ligand was varied computationally from hydride or bis[(trimethylsilyl)methyl] to two hydride ligands and to a BSR without a non hydrazine based ligand. Only one H$_2$ unit could be bound to all of the BSRs and the Cr(II)–H$_2$ interaction energies (method 3) reduced in the order two hydrides > hydride > hydrazide > bis[(trimethylsilyl)methyl] and are -68.78 > -48.52 > -37.75 > -28.33 kJmol^{-1} respectively.

For all of the studied systems the M–H$_2$ interaction energy generally increases as the π-accepting ability of the ancillary ligand decreases. This is due to less π electron density being accepted by the ancillary ligand so more electron density is available on the metal to π-back-donate to the H$_2$ molecule, thereby strengthening the M–H$_2$ interaction. For the silica based and Cr(II) hydrazine

linked systems this is clearly seen where the BSRs with the hydride ancillary ligands have the highest $M–H_2$ interaction energies as they have no orbitals to accept π density from the metal. The second highest are the methyl and hydrazine based ligands which could only accept π density through an agostic interaction with a C–H bond or a N–H bond respectively, and the lowest are the allyl and benzyl ligands that can accept the π density into their π systems. In the V(III) hydrazine linked system the hydride ligands give clearly the strongest $M–H_2$ interaction but the other ligands are less well differentiated. This trend was seen in later experimental investigations on the silica based materials that altered the ancillary ligand bound to the Ti(III) to methyl and allyl; and XPS showed that the Ti(III) bound to methyl was the most electron rich followed by allyl and then benzyl.[75]

The steric effects of the ligands do not seem to play a major role in determining the maximum number of H_2 units that can bind to the metal centres. For example, the silica based systems' BSRs with less sterically hindered hydride and methyl ancillary ligands bound fewer H_2 units than those with allyl or benzyl ancillary ligands, and in the Cr(II) hydrazine linked systems all of the BSRs bound the same number of H_2 units. In the V(III) system there is a small effect as the BSR with two hydride ancillary ligands can bind one more H_2 unit than the others.

The trend of rising hydrogen binding enthalpy with increasing hydrogen coverage seen experimentally, and with the computational models of the experimental systems, is not seen with all of the analogues with altered ancillary ligands. This would perhaps suggest that, especially for the silica based system where the binding sites are isolated, that the rising enthalpies would not be observed for all ligands. This initial supposition[82] was contradicted, however, by later experimental work on the silica based materials[75] that showed rising H_2 binding enthalpies with H_2 coverage with the ancillary ligand altered to methyl and allyl. Experimentally rising enthalpies with H_2 coverage have been observed for all the hydrazine linked materials,[77-80] however, with these materials where the metals are separated by at most two atoms M–M effects may be contributing

to the rising enthalpies and these effects are not modelled in the single metal BSRs. These cooperative effects will be investigated by probing the binding of H_2 to dimeric BSRs in a later chapter.

Altering the Metal

For all of the studied systems the metal was varied across the first row early transition metals maintaining its oxidation state. This was done with the various ancillary ligands probed in the different systems to see what effect altering the metal would potentially have if attempted on the experimental systems. Calculations were carried out on the early transition metals as they are considered to be likely candidates for H_2 storage materials due to their low relative atomic mass.

Silica Based Systems[82]

For the silica based BSRs the metal was altered from Ti(III) to V(III) and Cr(III). This increases the number of d electrons on the metal from one to two and three respectively. This was done with the benzyl, methyl and hydride ancillary ligands only and not allyl as it was considered to be similar to benzyl. Altering the metal did not alter the order of the M(III)–H_2 interaction energies (method 3) as the ancillary ligand was varied (Figure 28).
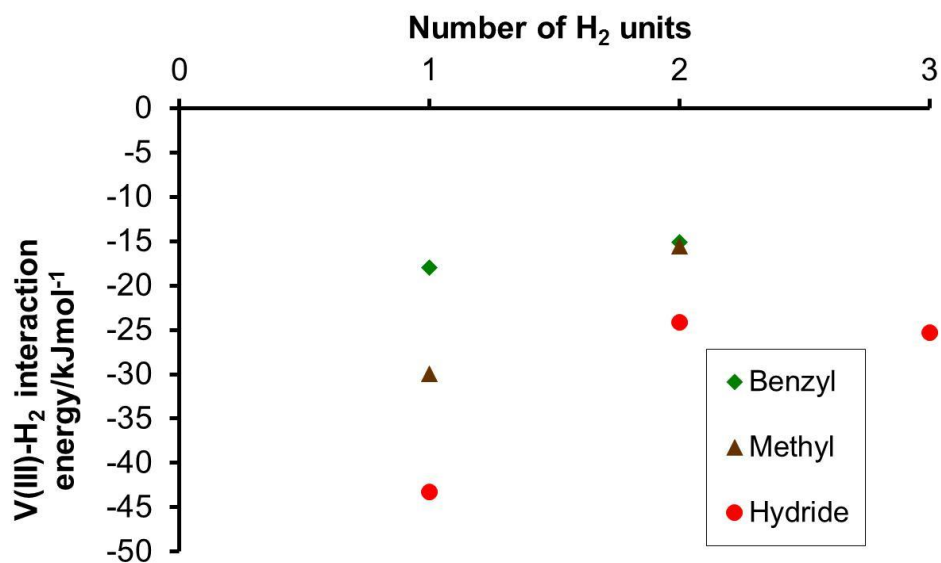
Figure 28: The V(III)–H_2 interaction energy (method 3) as a function of the number of H_2 units bound for the BSR of the silica based system with one varied ancillary ligand.
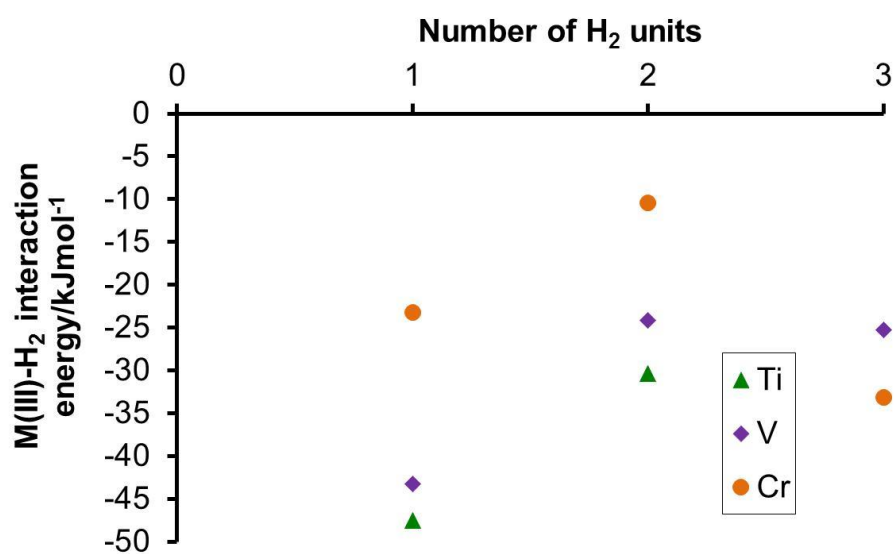
Figure 29: The M(III)–H_2 interaction energy (method 3) as a function of the number of H_2 units bound for the BSR of the silica based system with one hydride ancillary ligand and different metals.
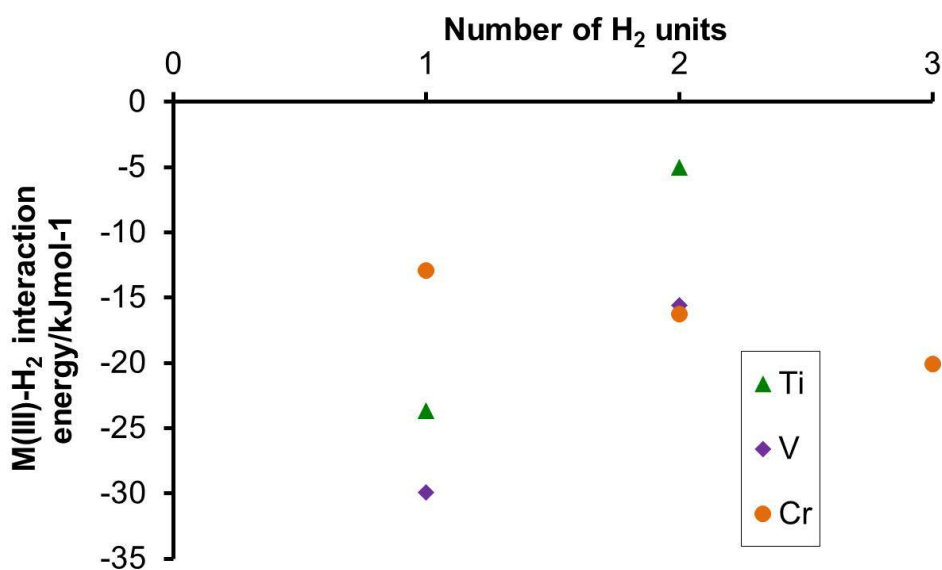
Figure 30: The M(III)–H$_2$ interaction energy (method 3) as a function of the number of H$_2$ units bound for the BSR of the silica based system with one methyl ancillary ligand and different metals.

Figures 29 and 30 show how the M(III)–H$_2$ interaction energy (method 3) of the silica based BSRs, with one hydride or methyl ancillary ligand respectively, varies with metal atom and with the number of bound H$_2$ units. Clearly the variation in the M(III)–H$_2$ interaction energy as a function of metal is not independent of the ancillary ligand.

The Hydrazine Linked V(III) System[83]

For the hydrazine linked V(III) BSRs the metal was altered from V(III) to Ti(III) and Cr(III). Graphs showing the change in the M(III)–H$_2$ interaction energy (method 4) as the metal is changed are shown in figures 31 – 36. The non-hydrazine based ancillary ligands (THF, hydride, two hydride ligands, 3-dimethylallyl and (trimethylsilyl)methyl and hydrazine based only ligands) are not altered in this set of calculations.
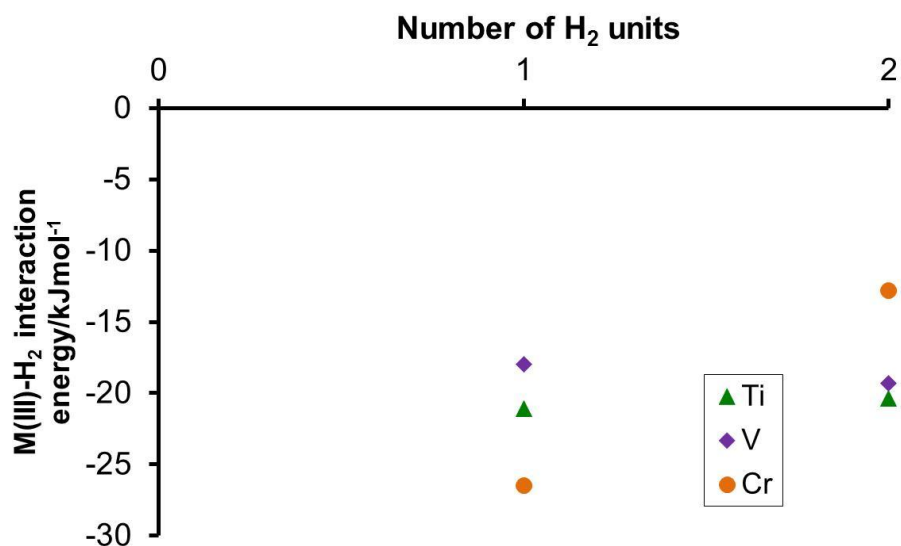
Figure 31: The M(III)–H₂ interaction energy (method 4) as a function of the number of H$_2$ units bound for four coordinate hydrazine linked BSRs with a THF ancillary ligand and different metals.
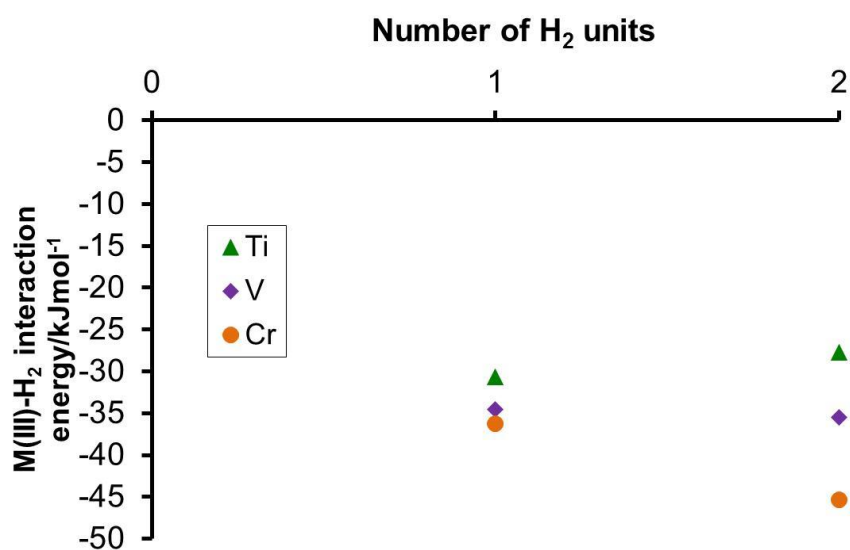
Figure 32: The M(III)–H₂ interaction energy (method 4) as a function of the number of H$_2$ units bound for four coordinate hydrazine linked BSRs with a hydride ancillary ligand and different metals.
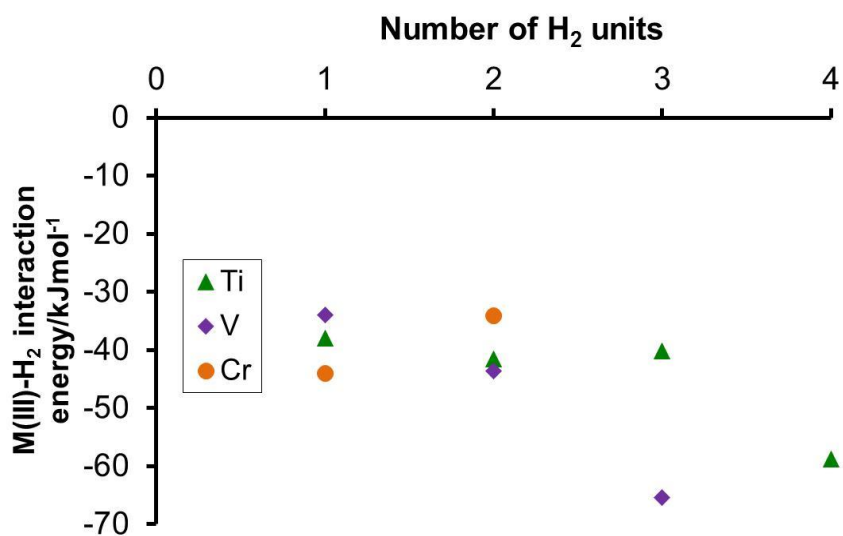
Figure 33: The M(III)–H_2 interaction energy (method 4) as a function of the number of H_2 units bound for four coordinate hydrazine linked BSRs with two hydride ancillary ligands and different metals.
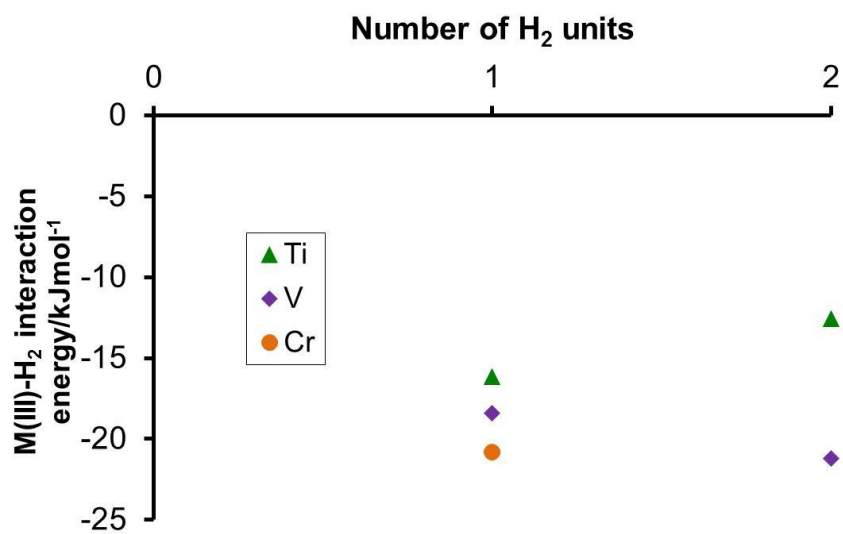
Figure 34: The M(III)–H_2 interaction energy (method 4) as a function of the number of H_2 units bound for four coordinate hydrazine linked BSRs with a 3-dimethylallyl ancillary ligand and different metals.
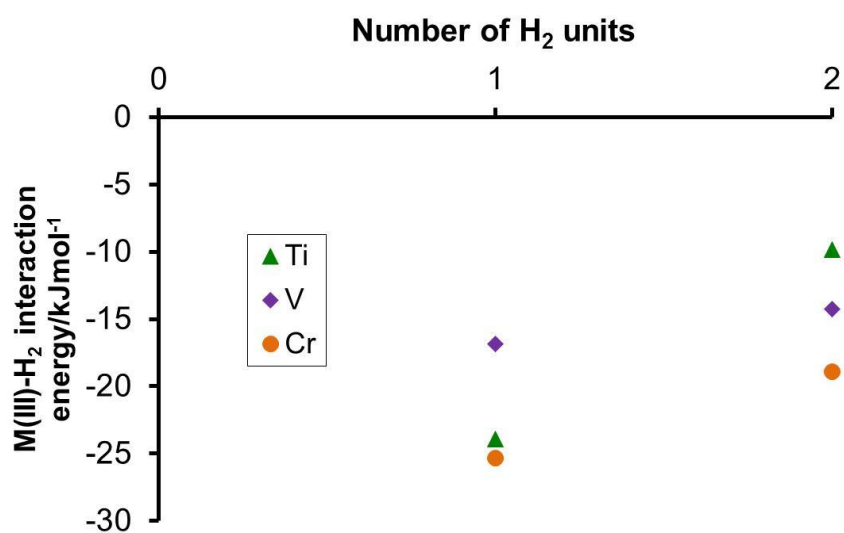
Figure 35: The M(III)–H$_2$ interaction energy (method 4) as a function of the number of H$_2$ units bound for four coordinate hydrazine linked BSRs with a (trimethylsilyl)methyl ancillary ligand and different metals.
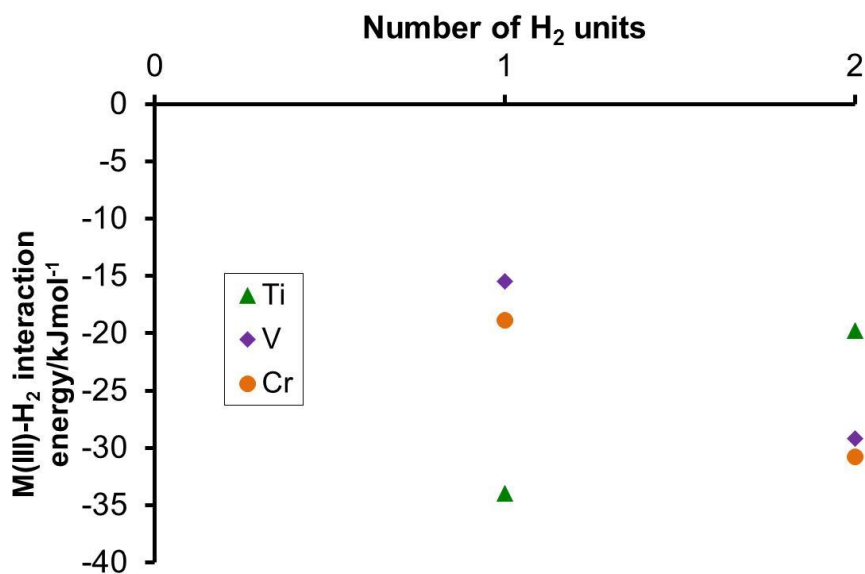
Figure 36: The M(III)–H$_2$ interaction energy (method 4) as a function of the number of H$_2$ units bound for four coordinate hydrazine linked BSRs with only hydrazine based ligands and different metals.

The change in the $M(III)–H_2$ interaction energy (method 4) upon altering the metal and keeping the ancillary ligand constant is generally smaller than when the ancillary ligand is changed and the metal is held constant. The order of the $M(III)–H_2$ interaction energies as the metal is changed is, again, not independent of the ancillary ligands bound to the metal. The metal seems to determine how many H_2 units can be bound when the ligands do not cause any steric hindrance. For example, when there are two hydride ligands bound to a four coordinate metal centre, changing from Ti(III) to V(III) and then to Cr(III) leads to a reduction in the number of H_2 units that can be bound, from four to three to two respectively (Figure 33).

The Hydrazine Linked Cr(II) System[84]

For the Cr(II) hydrazine linked systems the metal was altered to Ti(II), V(II) and Mn(II). The Mn(II) was found to not bind any H_2 units. This result would predict that an experimental H_2 storage material produced with Mn(II) would be very poor at storing H_2. Experimental work,[79] published after this computational work was completed, on Mn(II) did find that it is a much poorer hydrogen storage material than the Cr(II) analogue binding only a maximum of 0.59 H_2/Mn though not as poor as this computational result suggests. There is the same trend as for the M(III) hydrazine linked materials to fewer bound H_2 units as the periodic table is crossed. Figure 37 shows this for hydride ancillary ligands, as the number of H_2 units bound to the BSRs reduces as the metal is altered, with Ti(II), V(II) and Cr(II) binding three, two and one H_2 units respectively. This is also the case for the bis[(trimethylsilyl)methyl] ancillary ligand (Figure 38) where only one H_2 unit may be bound to Cr(II) but two to Ti(II) and V(II).
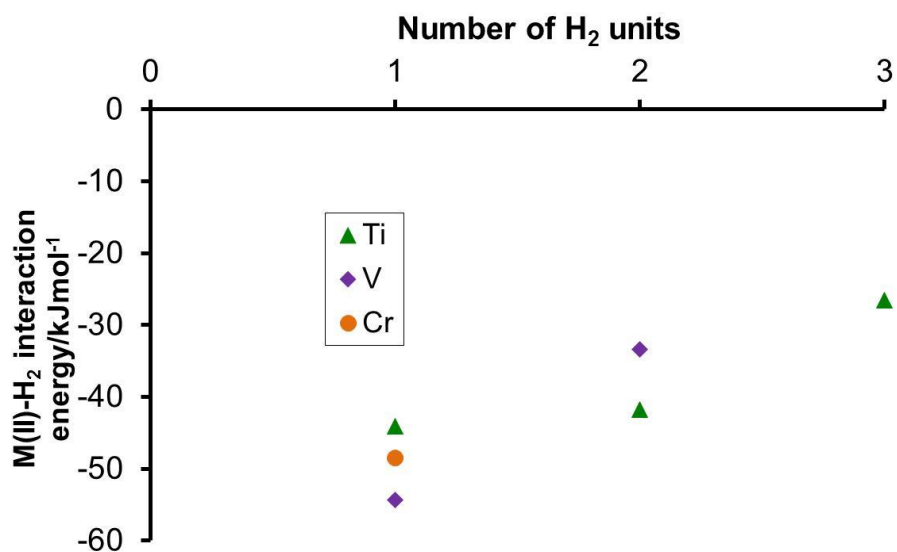
Figure 37: The M(II)–H$_2$ interaction energy (method 3) as a function of the number of H$_2$ units bound for four coordinate hydrazine linked BSRs with a hydride ancillary ligand and different metals.
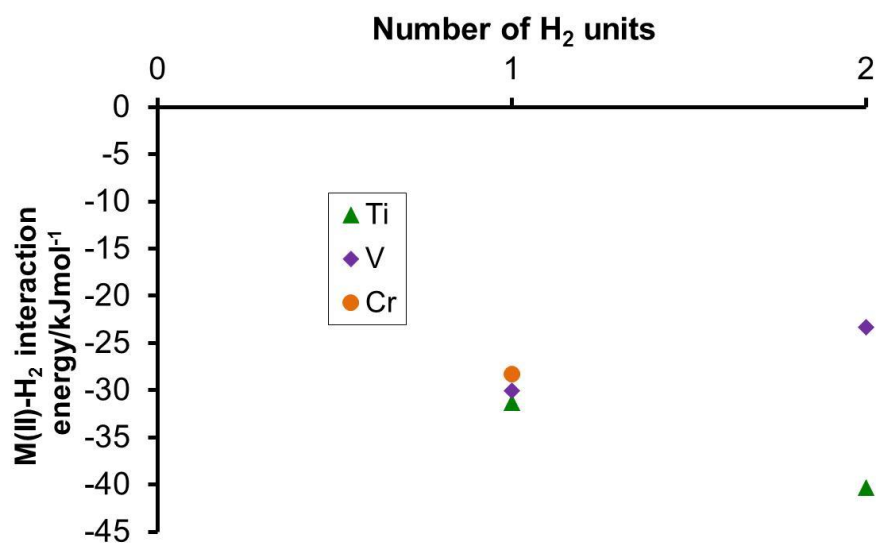
Figure 38: The M(II)–H$_2$ interaction energy (method 3) as a function of the number of H$_2$ units bound for four coordinate hydrazine linked BSRs with a bis[(trimethylsilyl) methyl] ancillary ligand and different metals.

Figures 37 and 38 show the M(II)–H_2 interaction energies (method 3) to be within 10 kJmol^{-1} of each other when one H_2 unit is bound showing again how altering the metal has less of an effect on the M–H_2 interaction energy than altering the ancillary ligand. The order of the M–H_2 interaction energies of the metals is again not independent of the ancillary ligand.

In summary, in all systems the metal did not affect the value of the M–H_2 interaction energy as much as the ancillary ligand and as such the order of the M–H_2 interaction energies as a function of metal was not independent of the ligand used. This may be due to the metal not affecting the amount of σ-donation versus π-back-donation of the Kubas interaction between the H_2 molecule and the metal as much as the ancillary ligands bound to the metal. This trend was previously noted by Kubas.[33]

For the hydrazine linked systems altering the metal across the periodic table reduces the number of H_2 units that can be bound especially with ligands that have a low steric hindrance. With the silica based systems and the benzyl ligand of the experimental model the number of H_2 units that can be bound reduces as the metal is altered across the periodic table. This agrees with later experimental results on the silica based systems which generally showed that altering the metal from Ti to V to Cr reduced the performance of the hydrogen storage material and would imply fewer H_2 molecules could be bound to each metal centre.[74] However, computationally for the silica based systems when the ancillary ligand is either hydride or methyl the number of H_2 units that can be bound as the metal is altered across the periodic table increases, and reduces for the BSRs with one and two ancillary ligands respectively. This effect may be due to the method of fixing the silica based BSRs as this meant that the BSR with one ancillary ligand was more constricted in its movement than the BSR with two ancillary ligands and this resulted in more imaginary frequencies of a higher wavenumber. All values are shown in appendix 1.

Partial Charges

Silica Based Systems[82]

The partial charges on the metal centres were also probed as the number of H_2 units bound to the metal centres was increased. For the silica based systems[82] for all of the BSRs with all of the different metal and ligand combinations the partial charge on the metal generally decreases as the number of H_2 units bound increases. For example, figure 39 shows the partial charge on the metal in the Ti(III) BSR with one benzyl ligand. All partial charge values are shown in appendix 2. Although the absolute values of the partial charges vary considerably as a function of analysis method and code/basis set, all approaches agree that as more H_2 are bound the Ti gains electron density, as was observed by Zhang and co-workers. in their study of Ti-substituted boranes (the partial charge on the Ti in B_5H_5Ti reduced from +1.24 with no H_2 molecules bound down to -0.82 with five bound H_2 molecules).[64] The reduction in partial charge suggests that the interaction is overall a donation from the H_2 molecule(s) to the Ti, consistent with the increase in H–H bond length and reduction in stretching frequency, as electron density is removed from the H_2 σ-bonding orbital.
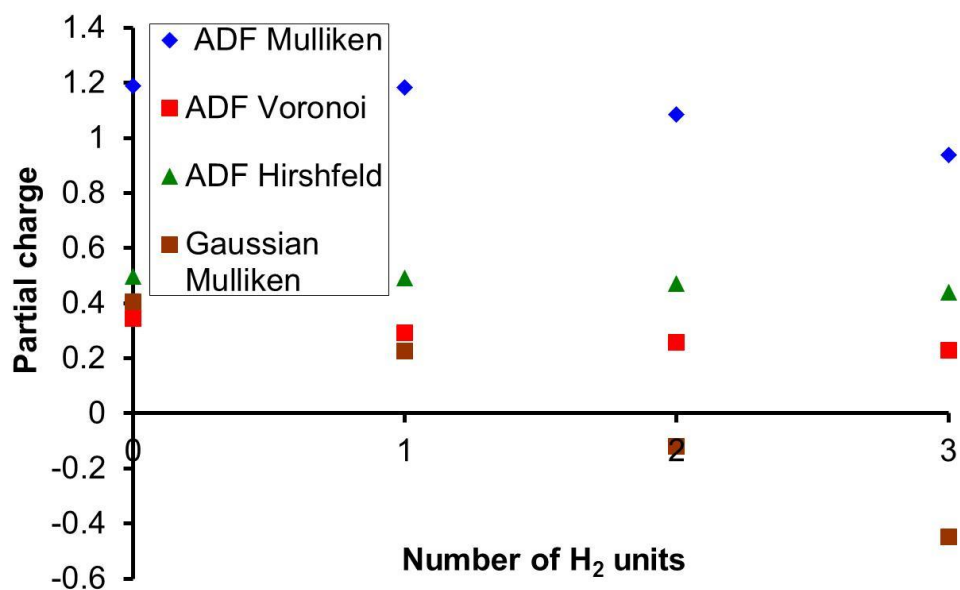
Figure 39: The partial charge on the Ti(III) of the silica based BSR with one benzyl ancillary ligand as a function of the number of H_2 units bound calculated using different programs and scales. The difference in the ADF and Gaussian Mulliken values stems mainly from the use of different basis sets.

The Hydrazine Linked V(III) System[83]

For the V(III) hydrazine linked system the trend in the partial charge on the metal as the number of H_2 units bound is increased is hard to observe for the computational representation of the experimental system, as few H_2 units could be bound. However, altering the ancillary ligand to two hydride ligands and the metal to Ti(III) meant that four H_2 units could be bound, and the trend that the metal generally becomes less positive the more H_2 units are bound is easily observable (Figure 40). This again suggests that the interaction is an overall donation from the H_2 molecule to the metal. All partial charge values are shown in appendix 2.
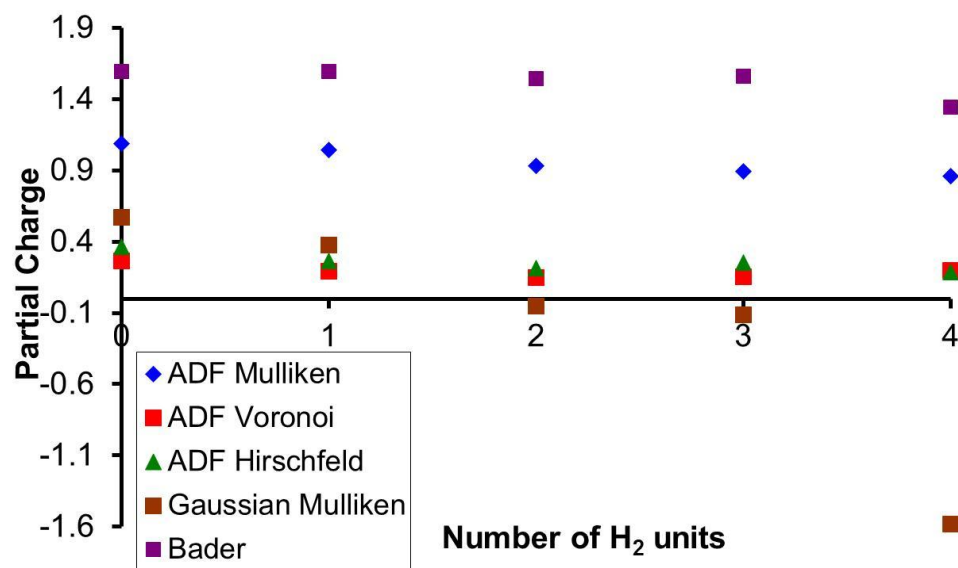
Figure 40: The partial charge on the Ti(III) in a four coordinate hydrazine linked BSR with two hydride ancillary ligands as a function of the number of H_2 units bound.

The Hydrazine Linked Cr(II) System[84]

For the Cr(II) hydrazine linked system the overall interaction between the metal and the H_2 seems to be a donation from the H_2 to the metal as out of all of the combinations of ancillary ligands and methods of calculating the partial charge, in 15 cases the partial charge on the metal reduces as more H_2 units are bound and in only five cases the partial charge increases (Table 4). For example, the partial charge on the Cr(II) in the four coordinate BSR with a hydride ancillary ligand is shown in figure 41.

Ancillary ligand	No. of H₂ bound	Method of partial charge calculation				
		Mulliken	Voronoi	Hirshfeld	Gaussian Mulliken	Bader
(Trimethylsilyl)methyl	0	0.668	0.352	0.404	0.704	1.151
	1	0.598	0.319	0.400	-0.202	1.137
Hydride	0	0.658	0.351	0.317	0.387	1.099
	1	0.616	0.327	0.338	-0.046	1.102
2 Hydride	0	0.572	0.370	0.294	0.124	1.027
	1	0.559	0.345	0.282	0.013	1.032
Hydrazine based	0	0.689	0.332	0.384	0.444	1.140
	1	0.663	0.324	0.391	-0.329	1.173

Table 4: Partial charge on the Cr(II) for the four coordinate hydrazine linked BSRs with various different ancillary ligands, number of H_2 units bound and methods of calculating the partial charge. The highlighted values show where the partial charge is rising as a function of the number of H_2 units bound.
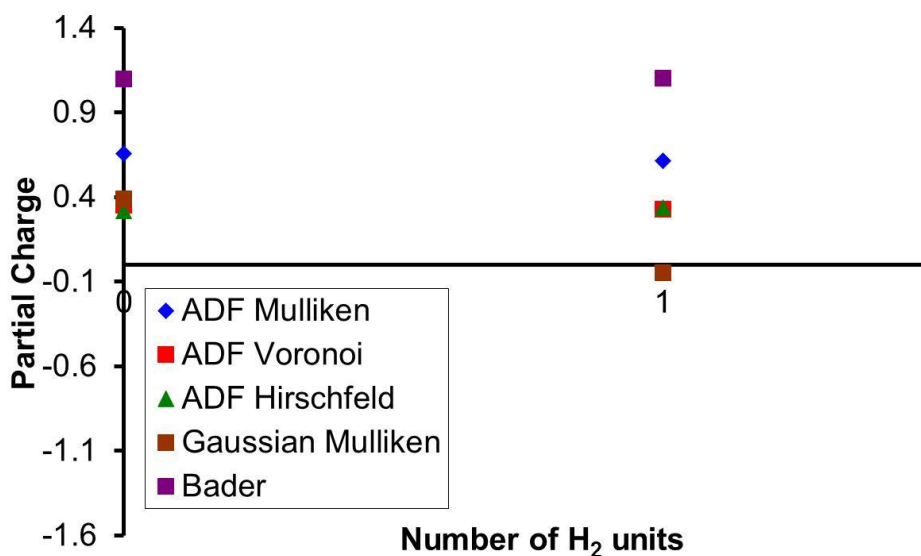
Figure 41: The partial charge on the Cr(II) in a four coordinate hydrazine linked BSR with a hydride ancillary ligand as a function of the number of H_2 units bound.

For the Ti(II) and V(II) hydrazine linked systems[84] the partial charge neither decreases nor increases significantly in most cases, suggesting a balance between the two synergic components of the Kubas bond. Examples for four

coordinate BSRs with Ti or V with a hydride ligand are shown in figures 42 and 43 respectively. All partial charge values are shown in appendix 2.
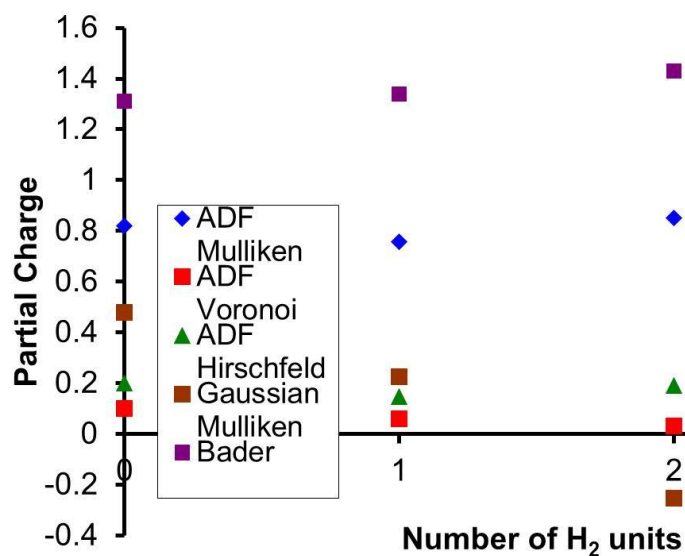
Figure 42: The partial charge on the Ti(II) in a four coordinate hydrazine linked BSR with a hydride ancillary ligand as a function of the number of H_2 units bound.
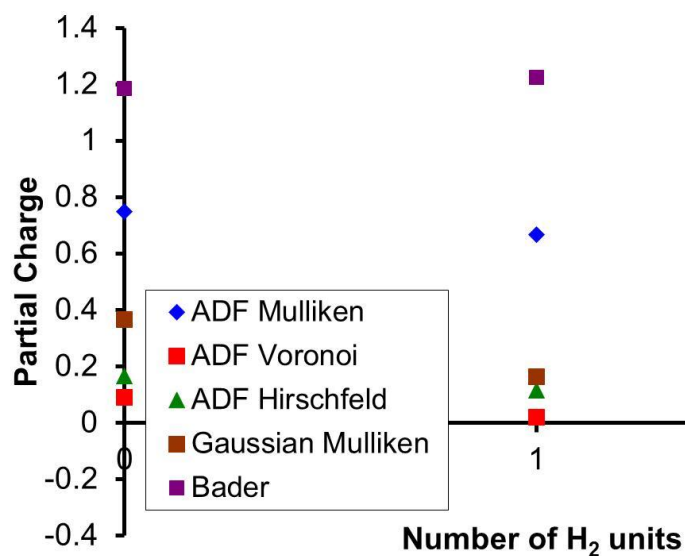
Figure 43: The partial charge on the V(II) in a four coordinate hydrazine linked BSR with a hydride ancillary ligand as a function of the number of H_2 units bound.

		Bis[(trimethylsilyl)methyl]		Hydride	
Metal	Orbital	No H_2 bound	1 H_2 bound	No H_2 bound	1 H_2 bound
Ti	LUMO	-1.50	-1.27	-1.31	-1.28
	HOMO	-2.27	-2.34	-2.15	-2.24
	HOMO-1	-2.34	-2.50	-2.23	-2.52
V	LUMO	-1.41	-1.18	-1.31	-1.28
	HOMO	-2.66	-2.54	-2.40	-2.54
	HOMO-1	-2.70	-2.84	-2.70	-2.84
	HOMO-2	-2.85	-2.92	-2.86	-2.92
Cr	LUMO	-1.10	-1.23	-1.09	-1.31
	HOMO	-2.87	-2.95	-2.86	-2.76
	HOMO-1	-3.60	-3.85	-3.57	-3.19
	HOMO-2	-3.70	-3.73	-3.77	-3.58
	HOMO-3	-3.78	-3.80	-3.88	-3.93

Table 5: Energies of predominantly d-based molecular orbitals for M(II) four coordinate hydrazine linked BSRs with either bis[(trimethylsilyl)methyl] or hydride ancillary ligands, as a function of metal and number of bound H_2 units.

An increase in the π-back-bonding component of the Kubas interaction might be expected in M(II) *vs* M(III), and also that the effect would be smallest for Cr(II), due to the stabilisation of the 3d orbitals across the periodic table. This is illustrated in Table 5; the occupied orbitals that interact with the H_2 molecule are generally the two lowest d-based orbitals for all of the metals, and those for Cr are much lower in energy than those of Ti or V. The more stable the d-based MOs, the less they will interact with the LUMO of the H_2 molecule (+0.72 eV) and the smaller the π-back-donation component of the M–H_2 bond.

In summary, for the early transition metals Ti(III), V(III), Cr(III) and Cr(II) the interaction with the H_2 molecule appears to be a σ dominated Kubas interaction whereas for Ti(II) and V(II) it is a balanced synergic bond. Ti(II) and V(II) are more electron rich compare to the M(III) centres and thus can take part in π-back-donation more readily. This pattern does not follow for Cr(II) due to the lowering in energy of the d orbitals across the periodic table.

M(II) vs M(III)[83, 84]

Comparing the four coordinate hydrazine linked BSRs with metals in the +3 oxidation state (method 4) to the analogous BSRs with metals in the +2 oxidation state (method 3) the M–H_2 interaction energies are generally higher when the metal is in the +2 oxidation state (Table 6). This could be due to the +2 oxidation state BSRs being more able to π-back-donate electrons to the H_2 unit. However, often the BSR with the metal in the +2 oxidation state can bind fewer H_2 units than the analogous BSR with the metal in the +3 oxidation state (Table 7). Experimentally the oxidation state of the metal was varied in the silica based systems and it was concluded that the materials generally performed better with metals in the +2 oxidation state over the +3 oxidation state in terms of a higher hydrogen binding enthalpy and an increase in the number of H_2 units binding per metal centre.[74] These computational results agree with a higher hydrogen binding enthalpy but not with an increase in the number of H_2 units bound for the M(II) binding sites over the M(III) binding sites. However, as experimentally the adsorption curves have not reached saturation[74] perhaps at higher pressures once the curves have reached saturation the M(II) material would bind less H_2 than the M(III) material and the greater binding of hydrogen at lower pressures is due to the higher binding enthalpy of the M(II) material.

M–H_2 interaction energies/kJmol^{-1} of binding the 1st H_2						
Ancillary Ligand	Ti^{3+}	V^{3+}	Cr^{3+}	Ti^{2+}	V^{2+}	Cr^{2+}
Silyl	-23.89	-16.84	-25.37	-31.32	-30.09	-28.33
Hydrazine	-33.95	-15.48	-18.86	-46.22	-37.33	-37.75
Hydride	-30.71	-34.51	-36.29	-44.11	-54.33	-48.52
2 Hydrides	-37.95	-34.02	-44.05	-59.69	-61.16	-68.78

Table 6: The M–H_2 interaction energies of binding the first H_2 unit for +2 (method 3) and +3 (method 4) oxidation state four coordinate hydrazine linked BSRs with varied ancillary ligands.

Maximum number of H_2 bound						
Ancillary Ligand	Ti^{3+}	V^{3+}	Cr^{3+}	Ti^{2+}	V^{2+}	Cr^{2+}
Silyl	2	2	2	3	2	1
Hydrazine	2	2	2	2	2	1
Hydride	2	2	2	3	2	1
2 Hydrides	4	3	2	3	2	1

Table 7: The maximum number of H_2 units bound for +2 and +3 oxidation state four coordinate hydrazine linked BSRs with varied ancillary ligands.

Reasons for the Experimentally Observed Increasing H_2 Binding Enthalpy with Increasing H_2 Coverage

In this section, explanations are proposed for the rising enthalpies with increasing hydrogen coverage seen experimentally in the silica based and hydrazine linked systems. The transition metal binding sites in the silica based system are at least a nanometre away from each other[73] so interactions between them are unlikely and, therefore, the explanation is based on local frontier orbital effects whereas, the metals in the hydrazine linked systems have at most two nitrogen atoms between them and the explanation is based on an interaction between the metals. In the silica based experimental systems it is thought that multiple H_2 molecules bind to each metal centre and that the increased binding enthalpy could therefore be explained by the consecutive binding of the H_2 at one metal centre becoming more favourable. In some of the experimental hydrazine linked systems it is thought that only one H_2 molecule binds to each metal and therefore the rising hydrogen binding enthalpy is thought to be due to the binding of H_2 at one metal centre affecting the binding of H_2 at another.

Silica Based Systems[82]

For the H_2 molecule to interact with the BSRs in a favourable manner there has to be good overlap between their respective frontier molecular orbitals, which should be of similar energy. The BSR needs a high HOMO and low

LUMO to interact with the high energy LUMO (0.72 eV) and low energy HOMO (-10.36 eV) of the H_2 molecule respectively. Molecular orbital (MO) analyses were carried out on the silica systems. Figures 44, 45 and 46 present valence molecular orbital energy level diagrams for Ti, V and Cr respectively for the silica based BSR with one hydride ancillary ligand. Indicated on these diagrams are the orbitals responsible for binding a given incoming H_2 (to produce the structure immediately to the right). These orbitals were located as follows. The M–H_2 σ-bonding and π-bonding orbitals in the BSR with the H_2 bound were identified, and the metal d character of these orbitals established. Those frontier MOs in the BSR without the H_2 bound which have the appropriate d character are then taken as the interacting frontier orbitals. If there is more than one orbital with the correct d character then an unweighted average of the orbitals' energies is taken as the energy of the interacting HOMO or LUMO.
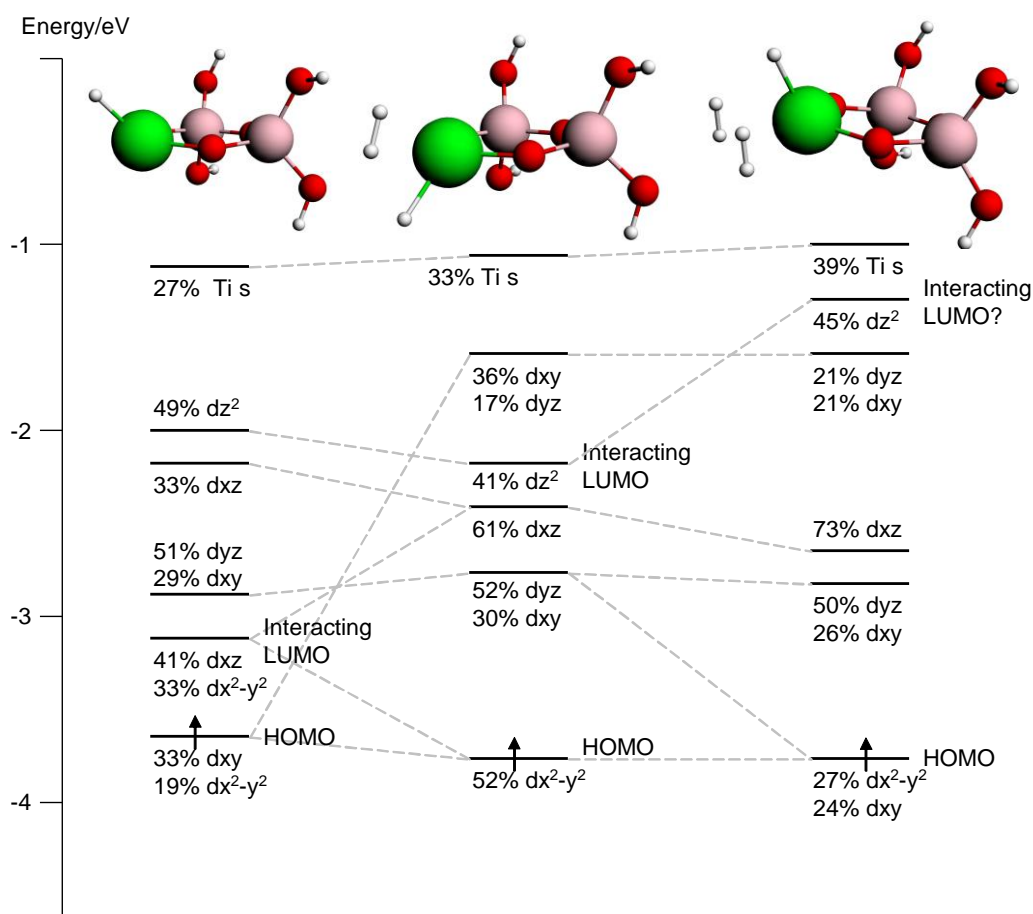
Figure 44: Molecular orbital diagram of the silica based Ti(III) BSR with one hydride ancillary ligand and zero, one and two H_2 units bound.

Energy/eV

0

-1

31% V s   25% V s   31% V s

22% V s

-2

37% dz^2

39% dx^2-y^2

63% dx^2-y^2

30% dxz

24% dxy   Interacting
                LUMO

Interacting
LUMO

36% dz^2
20% dxz

40% dz^2 Interacting
                LUMO

48% dz^2 Interacting
                LUMO

50% dxz

-3

42% dxz   Interacting
                LUMO

48% dxz
26% dz^2

58% dyz
20% dxy   Interacting
                LUMO

45% dyz
31% dxy

50% dyz
27% dxy

55% dxy
23% dyz

34% dx^2-y^2
27% dxy
35% dx^2-y^2 Interacting
23% dxy   HOMO

41% d_{xy} Interacting
27% d_{yz} HOMO

51% dyz
20% dxy

-4

39% dx^2-y^2 Interacting
                        HOMO

Figure 45: Molecular orbital diagram of the silica based V(III) BSR with one hydride ancillary ligand and zero, one, two and three H_2 units bound.

Figure 46: Molecular orbital diagram of the silica based Cr(III) BSR with one hydride ancillary ligand and zero, one, two and three H_2 units bound.

Through this analysis it was found that for a given ancillary ligand the M(III)–H_2 interaction energies track the energies of the HOMOs and LUMOs of the BSRs. For example, the Ti(III)–H_2 interaction energy (method 3) decreases on going from one to two bound H_2 units (-47.54 to -30.42 kJmol^{-1}) (Figure 25, Appendix 1) for the BSR with one hydride ancillary ligand. In the corresponding molecular orbital diagram (Figure 44) with no bound H_2, the HOMO (-3.67 eV) and LUMO (-3.15 eV) which bind to the incoming H_2 molecule are more favourable in energy (higher and lower respectively) for binding than the HOMO (-3.78 eV) and LUMO (-2.13 eV) when one H_2 unit is bound. A third H_2 molecule does not bind. This may well be because the $3d_z^2$-based LUMO of BSR$(H_2)_2$, which would interact with the incoming H_2 molecule, is high in energy (-1.27 eV).

The V(III)–H$_2$ and Cr(III)–H$_2$ interaction energies (method 3) increase on moving from two bound H$_2$ units to three for the BSR with 1 hydride ligand (V(III) -24.16 to -25.30 kJmol^{-1}, Cr(III) -10.45 to -33.14 kJmol^{-1}) (Figure 29, Appendix 1). This may be explained by the corresponding molecular orbital diagrams (Figures 45 and 46). For V(III) and Cr(III) the interacting HOMO energy rises by 0.35 eV and 1.07 eV respectively and the average energy of all the interacting LUMOs falls by 0.15 eV and 0.2 eV respectively on going from one to two bound H$_2$. Thus the orbitals become more favourable in energy to interact with the HOMO and LUMO of the incoming third H$_2$ molecule and the M(III)–H$_2$ interaction energies increase (more so for Cr than V as the HOMO energy change is larger in the d^3 system).

If the above explanation for the rising enthalpies with increasing hydrogen coverage is to explain the same experimental trend, the HOMO and LUMO energies of the computational model for the experimental (benzyl) system should also track the Ti(III)–H$_2$ interaction energies. However, for the computational model of the experimental system, the Ti(III)–H$_2$ interaction energies are smaller than for the compounds with hydride ancillary ligands, as are the changes in the interaction energies as a function of the number of bound H$_2$ (Appendix 1). We might, therefore, expect the changes in the interacting orbital energies to be smaller for the benzyl systems than is the case for the BSRs with hydride ligands. Figures 47 and 48 show the molecular orbital energy level diagrams of the two BSRs of the experimental system and comparison of these with figure 44, an analogous diagram with hydride ligands, shows this to be the case. Further comparison of figures 47 and 44 reveals another factor which should lead to the orbital energy changes being smaller in the benzyl case. The interacting LUMOs (those orbitals taking part in the σ-donation component of the Kubas interaction) are significantly less metal-based in the benzyl systems than for the hydride. Thus, the interacting LUMO in the BSRs with one hydride ligand is 74, 41 and 45% Ti d-based respectively with zero, one and two bound H$_2$. By contrast, the analogous orbitals for the benzyl BSR contain only 33, 25 and 21 % Ti d character. This reduction in metal d character from hydride to benzyl should

reduce the changes in orbital energy as H_2 are bound, as more of the orbital is localised away from the metal/H_2 interaction region.
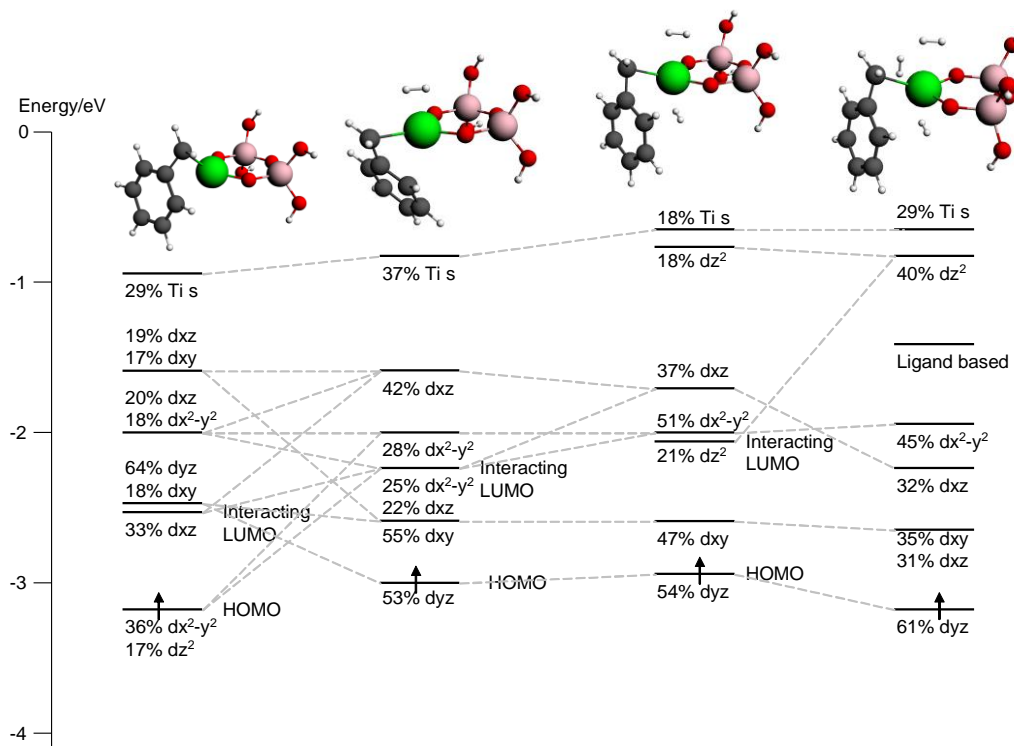
Figure 47: Molecular orbital diagram of a silica based Ti(III) BSR with one benzyl ancillary ligand and zero, one, two and three H_2 units bound.
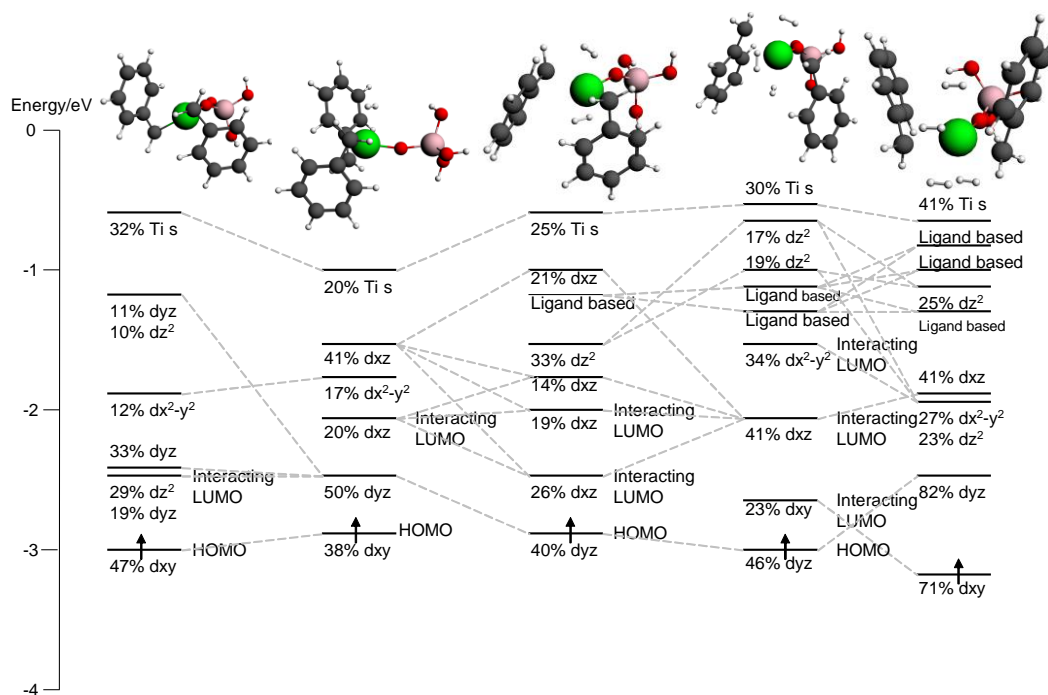
Figure 48: Molecular orbital diagram of a silica based Ti(III) BSR with two benzyl ancillary ligands and zero, one, two, three and four H_2 units bound.

Comparison of the molecular orbital diagrams (Figures 47 and 48) and the M–H_2 interaction energies (Figure 10, Appendix 1) of the computational models of the experimental system indicates that in some cases the changes in interacting MO energies correlate with the interaction energies, but not in others. For example, on going from one to two bound H_2 for the BSR with two benzyl ligands, the HOMO energy rises by 0.05 eV and the average interacting LUMO energy lowers by 0.08 eV. This closer energy match with the incoming H_2 levels makes it more favourable to bind the next H_2 molecule, and this agrees with the increase in the Ti(III)–H_2 interaction energy (method 2) from -19.69 to -21.80 kJmol^{-1} when binding two and three H_2 units respectively. However, for the BSR with 1 benzyl ligand both the HOMO and LUMO energies rise by 0.09 eV. Thus in this case the interacting energy levels show no favourability in energy for binding the next H_2, which does not agree with the increase in the Ti(III)–H_2 interaction energy (method 2) from -6.13 to -11.91 when binding two and three H_2 units respectively. However, the error in the energies of the interacting levels

does not allow the formation of firm conclusions as, for the reasons discussed earlier, the changes in the energy are small.

From this molecular orbital analysis it is suggested that the rising enthalpies with increasing coverage seen experimentally may be due to the binding of one H_2 molecule affecting the frontier orbital of the binding site locally such that they become closer to those of the H_2 molecule and thus that the binding is more favourable resulting in a stronger M(III)–H_2 interaction. This is clearly seen in the results from the BSRs with one hydride ancillary ligand but is less clear from the model of the experimental system due to the small changes in the molecular orbital energies in this case.

Hydrazine Linked Systems[85]

In order to see whether the rising enthalpies with increasing H_2 coverage could be caused by metal to metal (M–M) interactions such that the binding of H_2 at one metal centre affects the binding of H_2 at another metal centre the computational model of the binding sites needed to be extended from mono-metallic BSRs to those with multiple metal centres. It was thought initially that it would be possible to model the binding sites as molecules with multiple metal centres linked together. However, large versions of these BSRs with up to five metals proved to be computationally intractable (Figure 49). Therefore, dimers with two linked metal binding sites were modelled.
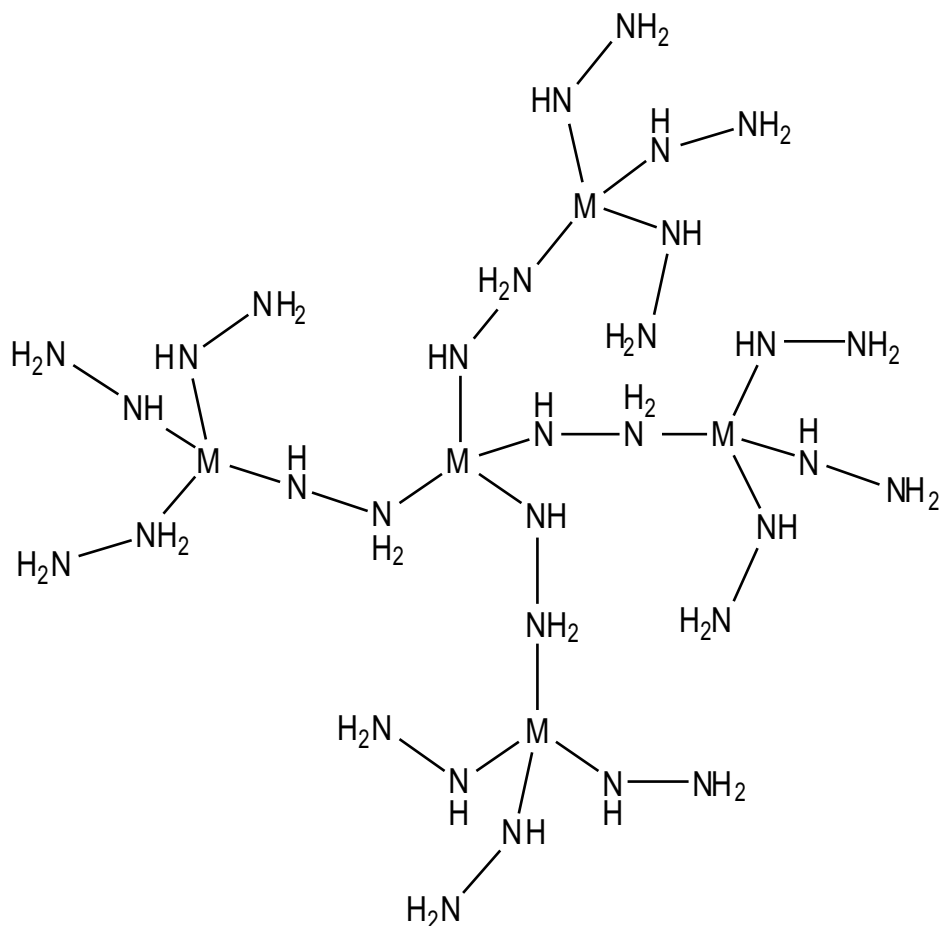
Figure 49: Schematic representation of an extended hydrazine linked BSR with five metal atoms.

From experimental findings[77] it is thought that the NH–NH$_2$ ligand can link the metal centres in either an η^2 fashion with each metal bound to one of the nitrogen atoms or that it can act as an μ^2 bridging ligand with the NH end of the ligand bound to both metals, and that a maximum of two ligands would link the two metals. The metals considered are Ti, V and Cr in both +3 and +2 oxidation states and Mn in the +2 oxidation state in order to link to experiment and previous computational studies, and only hydrazine-based ligands are probed. An exception is Ti where also a hydride ancillary ligand on each Ti is considered though this hydride ligand was not allowed to act as a bridging ligand and span the metal centres. An ancillary hydride ligand was considered as hydride ligands have shown higher adsorption enthalpies than π-accepting ligands.[82-84] The initial aim was to find the lowest energy dimers and hence the most likely method of

linking the metals in the solid. During geometry optimisation of these structures it became clear that some of the structures were at a lower energy than others and that some of the M(III) dimers had lower energy structures with three hydrazine ligands linking the two metal centres. This would leave one of the metal centres as five coordinate and the other as four coordinate. These dimers were also considered as possible representations of the experimental systems. All of these initial structures are shown in appendix 3. The most energetically favourable dimers and those within 20 kJmol^{-1} were selected for H_2 binding studies, and are shown schematically in Figures 50 and 51.
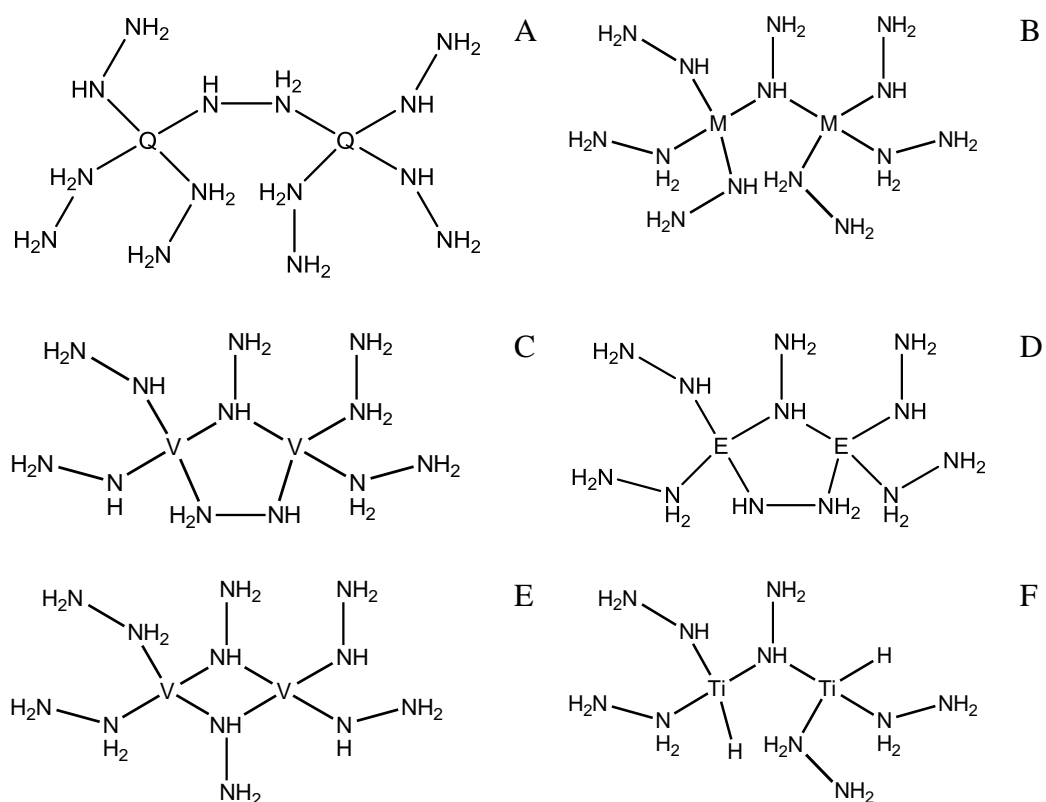
Figure 50: Schematic representations of the dimers with metals in the +2 oxidation state that were selected for H_2 binding studies. A – E are dimers one, two, five, six and eight with only hydrazine based ligands. "M" indicates that a low energy dimer was obtained for all four metals Ti, V, Cr and Mn, "E" indicates all three metals Ti, V and Cr, "Q" indicates Cr and Mn, while a specific metal symbol indicates that the structure was of low energy only for that metal. F is dimer two with Ti and one hydride ancillary ligand per metal. All dimers were initially calculated for all metals except only Ti was studied with hydride ancillary ligands.
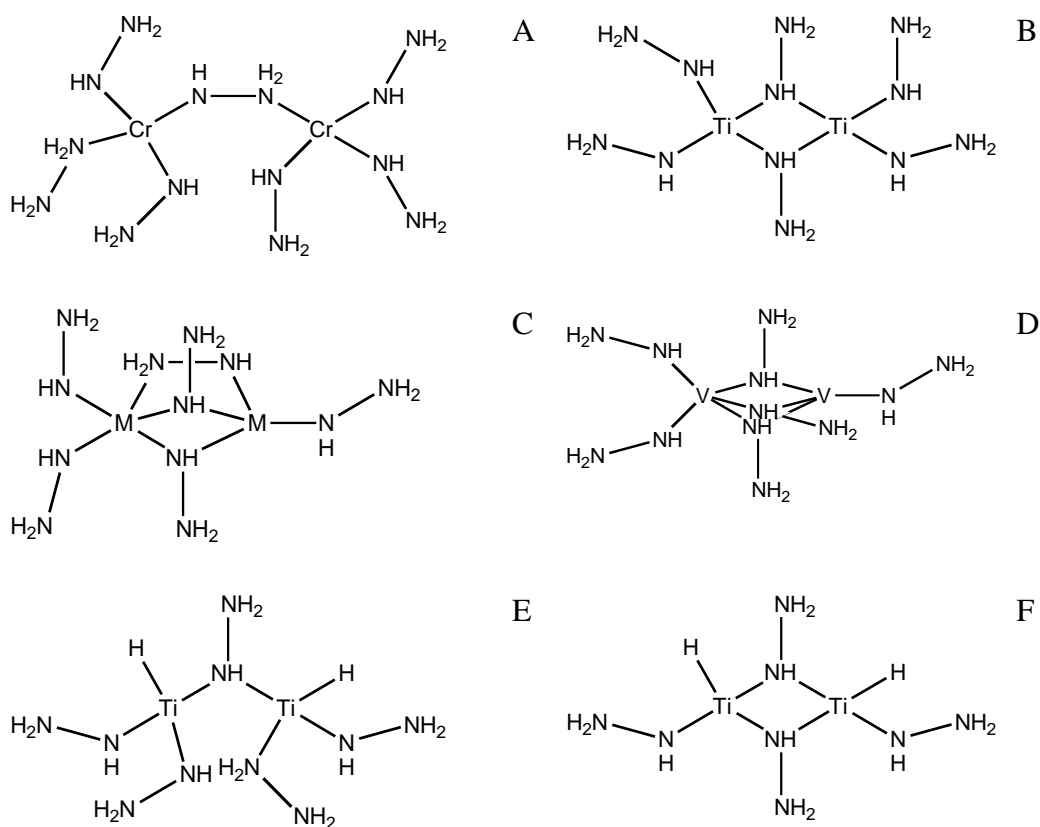
Figure 51: Schematic representations of the dimers with metals in the +3 oxidation state that were selected for H_2 binding studies. A – D are dimers one, seven, 12 and 14 with only hydrazine based ligands. "M" here indicates that a low energy dimer was obtained for two metals V and Cr, while a specific metal symbol indicates that the structure was of low energy only for that metal. E and F are dimers 2 and 7 with Ti and one hydride ancillary ligand per metal. All dimers were initially calculated for all metals except only Ti was studied with hydride ancillary ligands.

The lowest energy dimer for all of the studied M(II) systems is dimer two (D2) (Figure 50 B and F, Table 8) where the two metal centres are bridged by one hydrazide ligand in an μ^2 fashion through its 'NH' nitrogen atom. This is a much more open structure compared with the lowest energy structures of the M(III) centres where for Ti the metal centres are bridged by two hydrazides in an μ^2 fashion (D7 Figure 51 B and F, Table 9) and for V and Cr where the metal

114

centres are linked by three hydrazides, two of which bridge in an μ^2 fashion and one of which links in an η^2 fashion (D12 Figure 51 C, Table 9).

Dimer	Relative energy/kJmol^{-1}				
	Ti(II)	V(II)	Cr(II)	Mn(II)	Ti(II)H
2	0	0	0	0	0
6	14.14	0.59	3.99		
8		11.95			
5		14.31			
1			9.80	12.02	

Table 8: Relative energy of the H_2 free dimers with metals in the +2 oxidation state with respect to the lowest energy dimer for each metal. Only dimers within 20 kJmol^{-1} of the lowest energy dimer are included. Ti(II)H=dimer with hydride ancillary ligands.

Dimer	Relative energy/kJmol^{-1}			
	Ti(III)	V(III)	Cr(III)	Ti(III)H
7	0			0
12		0	0	
14		4.94		
1			14.16	
2				6.57

Table 9: Relative energy of the H_2 free dimers with metals in the +3 oxidation state with respect to the lowest energy dimer for each metal. Only dimers within 20 kJmol^{-1} of the lowest energy dimer are included. Ti(III)H=dimer with hydride ancillary ligands.

Before probing whether M–M interactions may be responsible for the experimentally observed rising H_2 binding enthalpy with increasing coverage, the results with the dimers were compared with those of the analogous mono-metallic BSRs. Comparison of the M–H_2 interaction energies of the lowest energy dimers[85] (method 3) with those of the four coordinate mono-metallic BSRs for the M(II)[84] (method 3) and M(III)[83] (method 4) systems (Appendix 1) does not reveal a strong correlation. There are cases where the interaction energies are extremely similar, for example with two H_2 bound to Ti(III) the values are -18.15 kJmol^{-1} and -19.80 kJmol^{-1} for the dimer and mono-metallic BSR respectively and cases where the energies are rather more different, for

example with two H_2 bound to V(II) the respective values are -32.40 kJmol[-1] and -8.93 kJmol[-1]

As discussed earlier, a rise in the M–H_2 interaction energy as more H_2 molecules are bound has been seen in the experimental systems.[77, 78] For the dimers the change in the interaction energy as more H_2 are bound depends on the metal and its oxidation state, and there are cases of it lowering, rising and staying approximately the same (Appendix 1). However, the experimental systems studied feature Cr(II) and V(III) and, with the lowest energy dimers for these metals, M–H_2 interaction energy (method 3) rises are seen. For Cr(II) D2 the M–H_2 interaction energy with 1 H_2 unit bound to one metal is -28.13 kJmol[-1] but with 1 H_2 unit bound to each metal it rises to -32.09 kJmol[-1]. For V(III) the analogous M–H_2 interaction energies are -9.97 kJmol[-1] and -18.28 kJmol[-1] respectively, but the M–H_2 interaction with two H_2 bound to one metal and one on the other metal is -16.97 kJmol[-1] as an average for all three H_2 units, showing a slight decrease. However, this decrease is not significant considering how close the value is to that where one H_2 unit is bound to each metal.

The Kubas interaction has been identified in the dimer models. In all the systems studied the H–H bond length increases from its computational free value of 0.752 Å to 0.770 – 0.831 Å, with a simultaneous reduction in its stretching frequency of 4317 cm^{-1} to 4012 – 3052 cm^{-1} (Appendix 1). Molecular orbitals showing the σ-donation and π-back-donation components of the Kubas interaction between the H_2 and the metal are presented for V(II) D2 with one bound H_2 in Figure 52. The density at the BCP of the H–H bond of the bound H_2 units for the classically Kubas systems is between 0.202 – 0.219 e bohr[-3] (Table 3).[83] For the dimers the values are between 0.207 – 0.247 e bohr[-3] (Appendix 1) showing that some of the interactions are of a similar strength to the classically Kubas systems and some are weaker (a higher H–H BCP density implies a stronger H–H bond, and hence weaker Kubas binding).
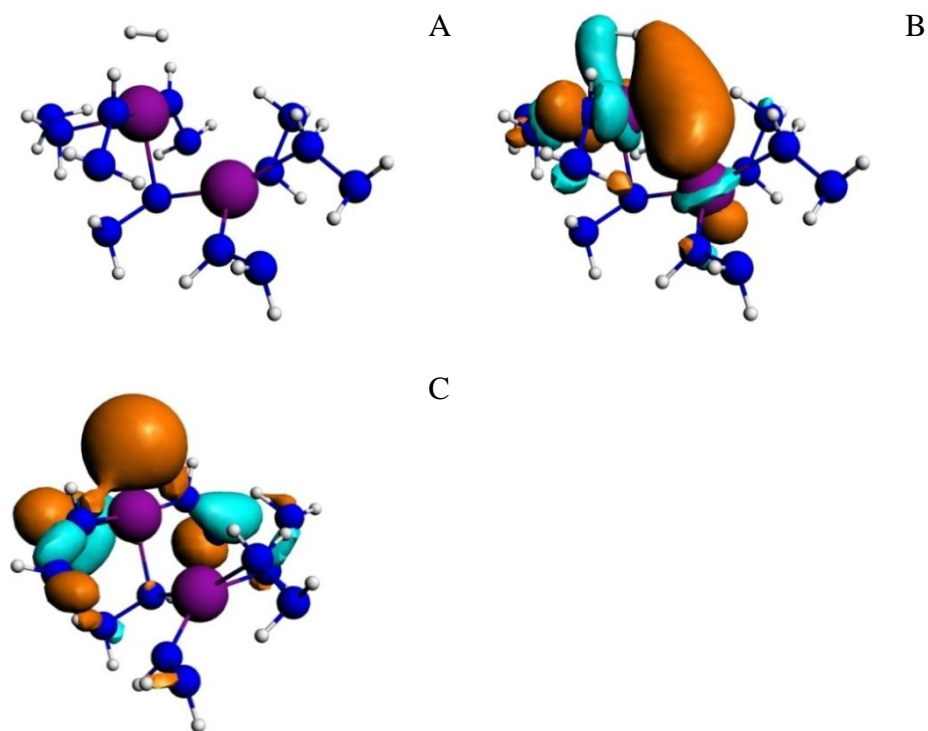
Figure 52: Three dimensional molecular orbitals of V(III) D2 with one H_2 unit bound showing; A, (bare molecule), B, HOMO-3 (π-back-donation) and, C, HOMO-61 (σ-donation).

The values of the H–H stretching frequency, bond length and BCP electron density are similar to those of the mono-metallic BSRs (Appendix 1).[83, 84] However, the range of the values is broader for the dimers indicating that introducing just one other binding site increases the variety in the interactions that occur. Extrapolating, the amorphous bulk solid may well have a greater range of Kubas interaction strengths.

In the four coordinate mono-metallic analogues, analysis of the partial charges on the metal centres suggested that the overall interaction of the H_2 with the metal is generally a σ-donation for the metals in the +3 oxidation state and for Cr(II) while for Ti(II) and V(II) there is a more balanced interaction.[83, 84] Here there tends generally to be a decrease in the partial charge on the metal directly bound to H_2 as one H_2 is bound for metals in the +3 oxidation state and a balance for all metals in the +2 oxidation state; for Ti examples see figures 53

and 54, with all values collected in appendix 2. This generally agrees with the results from the mono-metallic systems but the trends are less pronounced, presumably due to the perturbation of one H_2 molecule having a smaller effect on a larger system. The Cr(II) now also seems to favour a balanced interaction. Its preference for σ-donation, compared with Ti(II) and V(II) which favoured a balanced interaction in the mono-metallic analogues, was attributed to the fact that the metal d orbitals stabilise across the periodic table such that for chromium the highest occupied molecular orbital (HOMO) was lower and of less favourable energy for π-back-donation to the H_2.[84] Here, the interaction between the two metal centres broadens the range of frontier orbital energies and raises the HOMO energies of the dimers compared to the single metal BSRs (Table 10). Thus, the Cr(II) dimer has a higher HOMO that is more able to π-back donate to the H_2. This suggests that in the bulk there would be bands of frontier orbitals, many of which would be high enough in energy to take part effectively in π-back-donation.
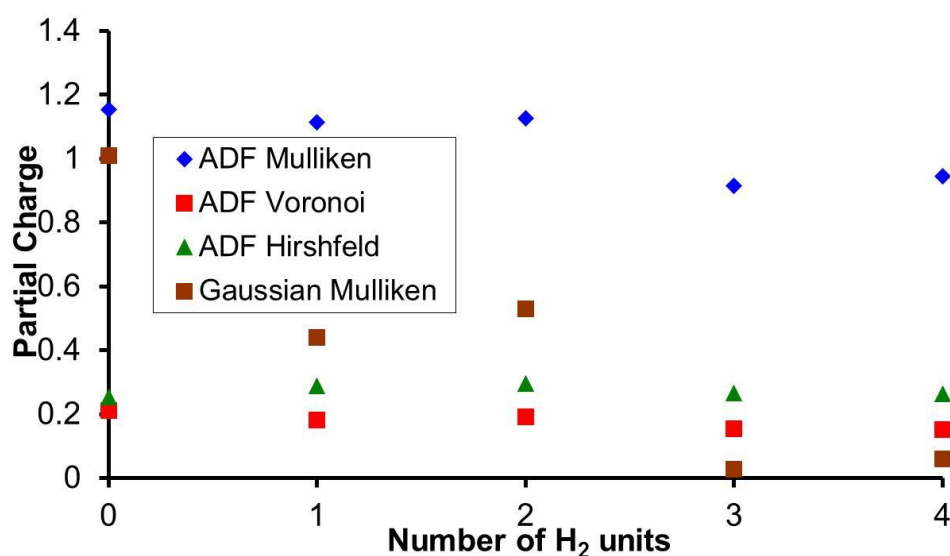
Figure 53: The partial charge on the Ti(III) that binds directly to the first H_2 unit for D7 with hydride ancillary ligands as a function of the number of H_2 units bound.
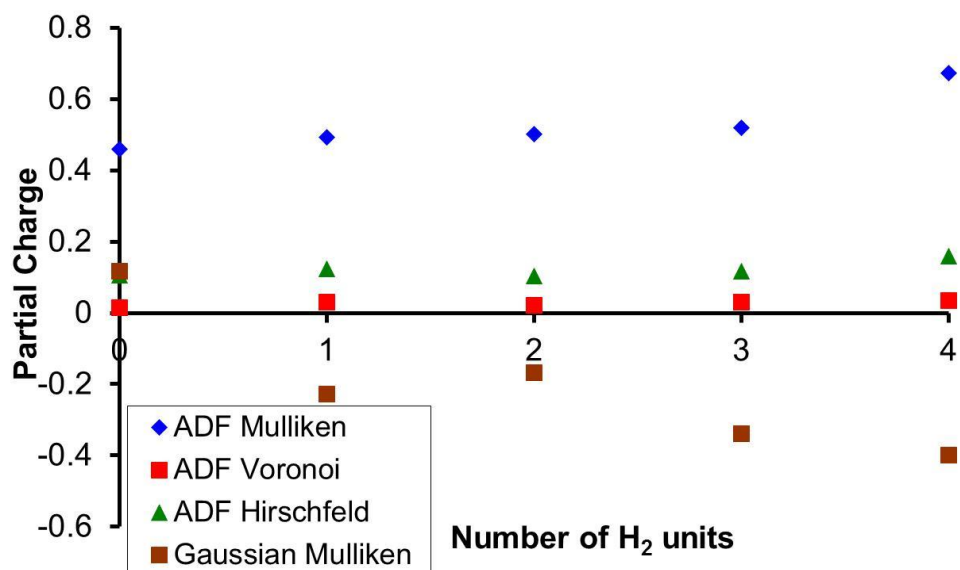
Figure 54: The partial charge on the Ti(II) that binds directly to the first H_2 unit for D2 with hydride ancillary ligands as a function of the number of H_2 units bound.

| Metal | Orbital | Orbital Energy/eV | |
		Dimer	Mono-metallic
Ti	LUMO	-1.396	-1.221
	HOMO	-1.821	-2.132
	HOMO-1	-2.208	-2.406
	HOMO-2	-2.366	
	HOMO-3	-2.696	
V	LUMO	-1.539	-1.145
	HOMO	-1.908	-2.401
	HOMO-1	-2.088	-2.585
	HOMO-2	-2.150	-2.678
	HOMO-3	-2.501	
	HOMO-4	-2.653	
	HOMO-5	-3.057	
Cr	LUMO	-1.593	-1.264
	HOMO	-2.675	-2.801
	HOMO-1	-2.963	-3.053
	HOMO-2	-3.159	-3.421
	HOMO-3	-3.397	-3.618
	HOMO-4	-3.501	
	HOMO-5	-3.546	
	HOMO-6	-3.666	
	HOMO-7	-3.866	

Table 10: Energies of predominantly d-based molecular orbital for the lowest energy M(II) dimers and four coordinate mono-metallic BSRs[84] with no H_2 units bound.

The partial charge on the metal not directly bound to the H_2 also alters upon H_2 binding but there is not a strong trend in these changes across the studied systems (Appendix 2).

In the mono-metallic hydrazine linked BSRs it is observed that altering the metal across the periodic table reduces the number of H_2 units that can be bound to the metal centre as the number of empty d orbitals for the H_2 unit to donate into decreases.[83, 84] This is also observed in the dimeric models (Appendix 1). In general, fewer H_2 units per metal centre could be bound to the dimer models compared to the mono-metallic analogues and this could be due to the reduced flexibility and increased steric hindrance of the dimeric systems. However, in the case of Mn(II) in the mono-metallic BSRs no H_2 units could be bound whereas with the analogous dimer one H_2 unit could be bound as two hydride ligands. The binding of one H_2 unit per two metal centres as two hydride ligands for the Mn(II) systems does, though, compare favourably with the experimental evidence for the Mn(II) hydrazine linked hydrogen storage material that can bind a maximum of only 0.59 H_2/Mn, especially since the desorption isotherms show a small amount of irreversibility.[79] This irreversibility could be caused by some hydrogen binding as hydride ligands.

The results on the dimers corresponded reasonably well with those of the analogous mono-metallic systems and therefore the systems were probed to see whether 3d-based metal-metal (M–M) interactions affect the binding of the H_2. In order to do this the M–H_2 interaction energies (method 3) were calculated when the metal to which the H_2 is not directly bound was altered to either Al(III) in the case of the M(III) systems or Ca(II) in the case of M(II). In this way the valence d orbitals were removed but the size of the metal atom remained approximately the same. In most cases this alteration had little effect on the M-H_2 interaction energies suggesting that in such cases the M–H_2 interaction is a local interaction (Tables 11 and 12). However, in a few cases it significantly reduced the M–H_2 interaction energy suggesting that the second metal is significant in the bonding of the H_2. Further analysis reveals that the second

120

metal affects the M–H$_2$ interaction only when a M–M interaction is present in the orbital that is π-back-donating to the H$_2$, and where the second metal contributes atomic orbitals of the same type as the first metal. For example, with D6 and Ti(II) the molecular orbital involving the most π-back-donation to the H$_2$, HOMO-2, also displays a M–M interaction (Figure 55 B), and includes contributions of 20.08% d_{xy} and 16.15% $d_{x^2-y^2}$ from the Ti bound directly to the H$_2$ and 7.32% $d_{x^2-y^2}$ and 7.22% d_{xy} from the second Ti. The corresponding orbital showing the most π-back-donation in the case where the second Ti is replaced with Ca, HOMO-1, does not have a contribution from the Ca atom or a M–M interaction (Figure 56 B). Similarly with D8 and V(II) there is a molecular orbital, HOMO-5, showing a strong π-back donation component to the H$_2$ as well as a strong M–M interaction, and the orbital contributions include 27.96% d_{xz} and 6.29% $d_{x^2-y^2}$ from the V bound directly to the H$_2$ and 12.38% d_{z^2} and 11.52% d_{xz} from the second V (Figure 57 B). With more d electrons in the V system than the Ti, the situation is more complicated as there are also three other orbitals showing π-back-donation to the H$_2$, but these either do not have a M–M bonding component and/or the second V does not contribute the same type of functions as the V bound directly to the H$_2$.

It would be expected that the alteration of the Mn(II) not directly bound to H$_2$ would alter significantly the M–H$_2$ interaction energy as the dimeric Mn(II) model could bind a H$_2$ unit whilst the analogous mono-metallic model could not. However for the Mn(II) dimeric system there is not a significant change in the M–H$_2$ interaction. This negative result suggests that the 3d orbitals are not affecting the M–H$_2$ interaction in this case. For Mn(II) the interaction with the hydrogen is purely a σ-donation as the hydrogen is binding as two hydride ligands and therefore perhaps all that is required is a larger molecule over which the electron density donated by the hydride ligands can be delocalised in order for there to be an improvement in the number of H$_2$ units that can be bound.

Dimer	M–H$_2$ interaction energies/kJmol^{-1}					M–H$_2$ interaction energies with Ca/kJmol^{-1}					Change in M–H$_2$ interaction energies/kJmol^{-1}				
	Ti(II)	V(II)	Cr(II)	Mn(II)	Ti(II)H	Ti(II)	V(II)	Cr(II)	Mn(II)	Ti(II)H	Ti(II)	V(II)	Cr(II)	Mn(II)	Ti(II)H
2	-42.33	-44.30	-28.13	-463.93	-40.10	-40.22	-46.30	-29.36	-465.02	-42.85	+2.11	-2.00	-1.23	-1.09	-2.75
6	-43.85	-63.36	-33.68			-28.02	-61.80	-36.05			+15.83	+1.56	-2.37		
8		-65.05					-42.77					+22.28			
5		-32.15					-30.63								
1			-37.5					-37.29					+0.21		

Table 11: The M(II)–H$_2$ interaction energies (method 3) of binding the first H$_2$ unit with and without the other metal as Ca, and the change between the two. Ti(II)H=dimer with hydride ancillary ligands. The values highlighted in red indicate where altering the metal had a significant effect on the M(II)–H$_2$ interaction energy.

Dimer	M–H$_2$ interaction energies/kJmol^{-1}				M–H$_2$ interaction energies with Al/kJmol^{-1}				Change in M–H$_2$ interaction energies/kJmol^{-1}			
	Ti(III)	V(III)	Cr(III)	Ti(III)H	Ti(III)	V(III)	Cr(III)	Ti(III)H	Ti(III)	V(III)	Cr(III)	Ti(III)H
7	-12.03			-47.83	-8.07			-38.73	+3.96			+9.10
12		-9.97	-16.83			-12.64	-17.78			-2.67	-0.95	
14		-26.54				-27.39				-0.85		
1			-17.08				-17.77				-0.69	
2				-15.37				-11.36				+4.01

Table 12: The M(III)–H$_2$ interaction energies (method 3) of binding the first H$_2$ unit with and without the other metal as Al, and the change between the two. Ti(III)H=dimer with hydride ancillary ligands. The values highlighted in red indicate where altering the metal had a significant effect on the M(III)–H$_2$ interaction energy.
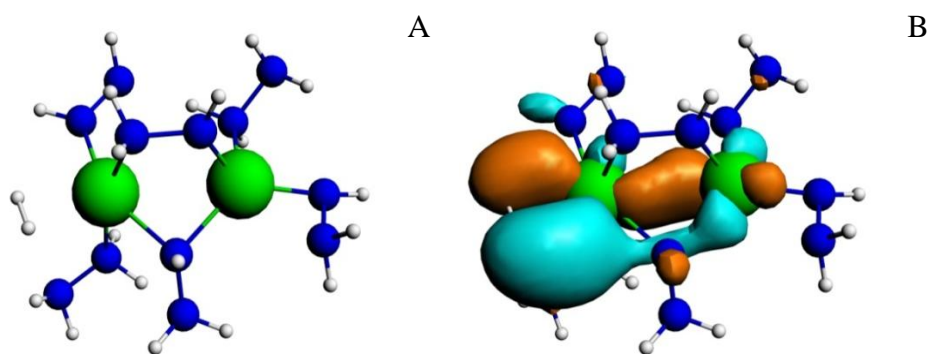
Figure 55: Three dimensional molecular orbitals of Ti(II) D6 with one H_2 unit bound showing; A, (bare molecule) and, B, HOMO-2 (π-back-donation).
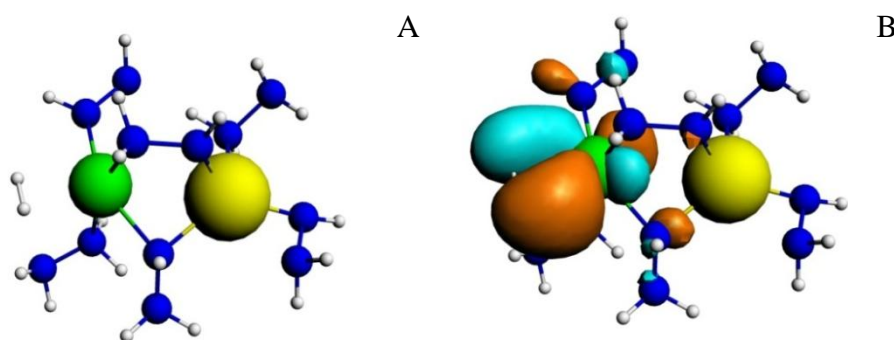
Figure 56: Three dimensional molecular orbitals of Ti(II)/Ca(II) D6 with one H_2 unit bound showing; A, (bare molecule) and, B, HOMO-1 (π-back-donation).
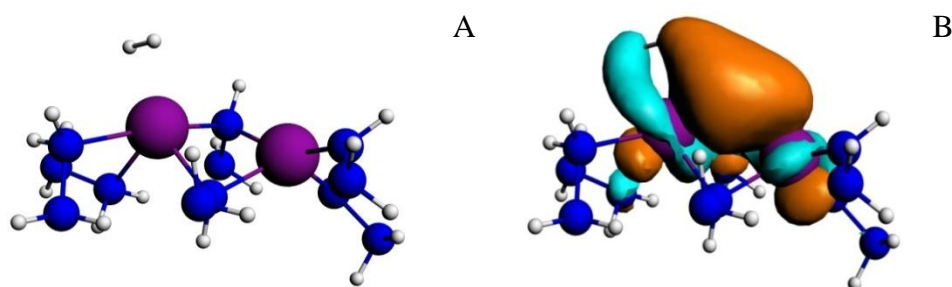

Figure 57: Three dimensional molecular orbitals of V(II) D8 with one H_2 unit bound showing; A, (bare molecule) and, B, HOMO-5 (π-back-donation).

Of the M(III) systems there is only one example of M–M bonding affecting the binding of the first H_2 and that is Ti(III) D7 with hydride ancillary ligands. Here the M–H_2 interaction is dominated by σ-donation from the H_2 as

there is not an orbital showing strong π-back donation (Figure 58) and the partial charge on the metal directly bound to the H_2 becomes more negative (ADF Mulliken 1.153 to 1.113, Voronoi 0.211 to 0.182, Hirshfeld 0.254 to 0.288 and Gaussian Mulliken 1.010 0.439) (Appendix 2). Before the second Ti is substituted for Al there are two orbitals showing a strong M–M interaction, HOMO and HOMO-1, that are not present afterwards (Figure 58 B and C and Figure 59). The greater delocalisation of the electron density when the Ti is present, aided by a M–M interaction, may be stabilising the mainly σ Kubas interaction in this case. This is in contrast to Ti(II) D6 and V(II) D8 where the partial charges of the metal binding directly to the first H_2 unit before and after binding suggest that the interaction has a greater π-back-donation component as they generally become more positive (Table 13, Appendix 2).
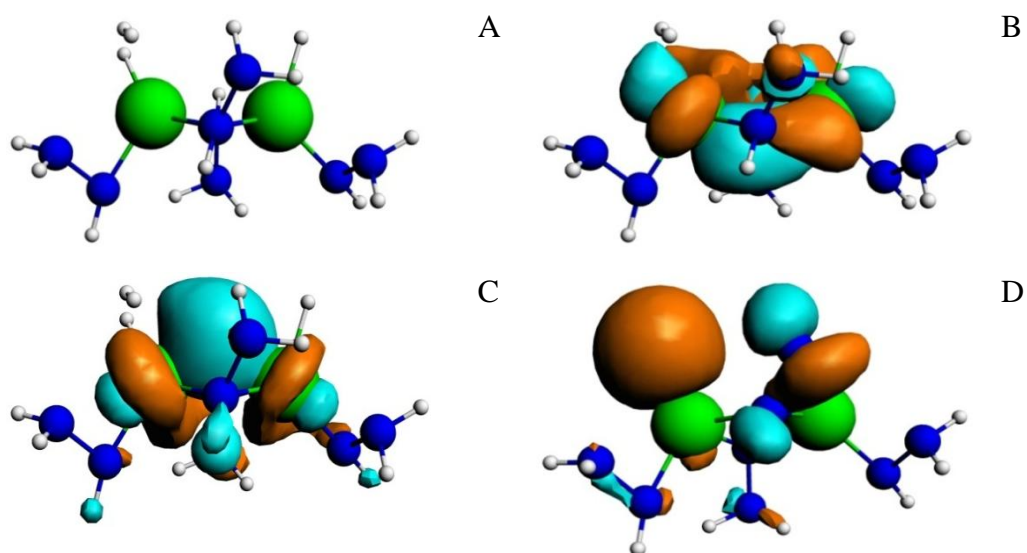
Figure 58: Three dimensional molecular orbitals of Ti(III) D7 with hydride ancillary ligands and one H_2 unit bound showing; A, (bare molecule), B, HOMO, C, HOMO-1 and, D, HOMO-33 (σ-donation).
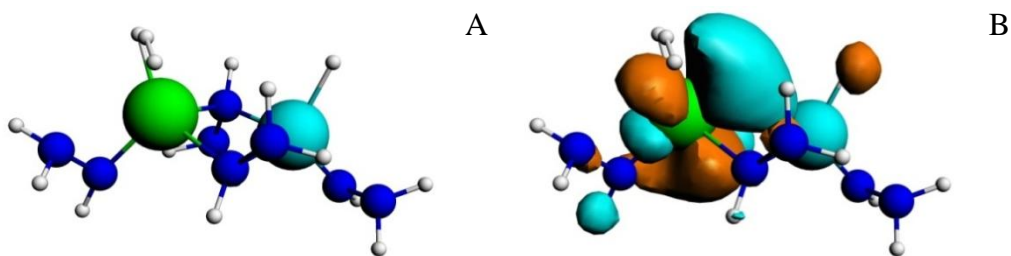
Figure 59: Three dimensional molecular orbitals of Ti(III)/Al(III) D7 with hydride ancillary ligands and one H_2 unit bound showing; A, (bare molecule) and, B, HOMO.

	V(II) D8		Ti(II) D6	
No. H_2 bound	0	1	0	1
ADF Voronoi	-0.062	-0.036	0.034	0.058
ADF Hirshfeld	0.098	0.120	0.134	0.192
ADF Mulliken	0.475	0.622	0.690	0.843
Gaussian Mulliken	0.293	0.268	0.644	0.162
Bader	0.930	0.131	1.238	1.384

Table 13: The partial charge on the metal directly bound to the H_2 unit for V(II) D8 and Ti(II) D6.

Orbitals showing some sort of M–M interaction may be observed in dimers where altering the second metal does not affect the M–H_2 interaction (*e.g.* Figure 60) but these do not show a π-back-donating component to the H_2 and/or the second metal is not contributing the same type orbitals as the metal bound directly to the H_2.
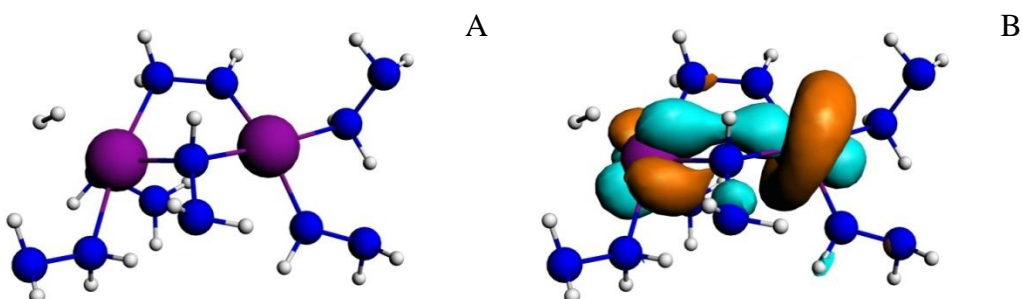
Figure 60: Three dimensional molecular orbitals of V(II) D6 with one H_2 unit bound showing; A, (bare molecule) and, B, HOMO-3.

The M–M distance tends to lengthen as more H_2 units are bound (Tables 14 and 15) and this is probably due to the increased coordination. Whether or not the second metal affects the M–H_2 interaction does not seem to depend on the M–M distance and so is not a proximity effect.

	M–M bond length with no H_2 bound/Å				M–M bond length with H_2 bound/Å			
Dimer	Ti(II)	V(II)	Cr(II)	Ti(II)H	Ti(II)	V(II)	Cr(II)	Ti(II)H
2	2.865	3.008	3.335	2.628	3.094	2.947	3.072	2.704
6	3.012	3.063	3.160		3.063	3.344	3.294	
8		2.759				2.875		
5		3.026				2.976		
1			4.033				4.218	

Table 14: The M–M distance with zero and one H_2 unit bound for the M(II) dimers. Ti(II)H=dimer with hydride ancillary ligands. The highlighted values indicate where the M–M distance shortens upon binding H_2.

	M–M bond length with no H_2 bound/Å				M–M bond length with H_2 bound/Å			
Dimer	Ti(III)	V(III)	Cr(III)	Ti(III)H	Ti(III)	V(III)	Cr(III)	Ti(III)H
7	2.723			2.773	2.732			2.748
12		2.760	2.948			2.845	3.003	
14		2.668				2.730		
1			4.619				4.434	
2				2.900				2.975

Table 15: The M–M distance with zero and one H_2 unit bound for the M(III) dimers. Ti(III)H=dimer with hydride ancillary ligands. The highlighted value indicates where the M–M distance shortens upon binding H_2.

In conclusion, the above evidence for the participation of adjacent metals in the same orbitals could account for the experimentally observed metallic properties of the hydrazine linked materials[79] and, as the presence of two transition metals has been shown to strengthen the M–H_2 interaction in some cases, this could also contribute to the rising adsorption enthalpies with increasing H_2 coverage seen experimentally. The binding of H_2 at one centre could affect the ease of binding at another centre through the interaction of the metals. Indeed, for Cr(II) and V(III), (the metals used in the experimental systems) for the lowest energy dimers the average M–H_2 interaction energy (method 3) is higher when there is one H_2 bound to each metal rather than when

only one H_2 is bound to one metal (Cr(II) -28.13 to -32.09 kJmol^{-1} and V(III) -9.97 to -18.28 kJmol^{-1}, Appendix 1). The experimentally observed metallic properties of the bulk structure[79] suggests a band structure. The binding of H_2 could alter slightly the energy levels of the bands to make H_2 binding more favourable.

Neither explanation of the rising hydrogen binding enthalpies with increased coverage for either material is proven absolutely. The computational model is very much a simplification of the complex amorphous experimental systems and therefore the explanations should be taken with due caution. With few experimental measurements many explanations for the unusual rising enthalpies are possible. In the hydrazine linked materials the adsorption and desorption of the H_2 is controlled by altering the pressure and therefore it has been suggested by the experimentalists that there is a pressure induced deformation of the structure, which alters it favourably for H_2 binding and when the pressure is relaxed that, the material reverts to a position less favourable for H_2 binding.[85] High pressure and a large amorphous structure cannot be modelled with the molecular approach adopted here and so this suggestion is also possible.

Late First Row Transition Metal Hydrazine Linked Systems[86]

The experimentalists' research[73-75, 77-80] has focused on the early transition metals as they are considered the most promising for H_2 storage due to their low molecular weight. However, it is also of interest to probe the effect of altering the metal in the hydrazine linked materials to later transition metals, as they have the potential to form more stable hydrazine linked materials. Specifically, it is proposed that hydrazine linked materials with Ni(II), Cu(II) and Cu(I) binding sites could be produced from the known homoleptic alkyls and aryls of the metals,[145-147] in a similar fashion to the Cr(II) hydrazine linked materials. It was therefore decided to apply the computational model used for the early transition metal hydrazine linked materials to these proposed systems and model the binding sites as molecules. Only hydrazine based ligands were used and the oxidation state was determined by altering the number of bound hydrazide ligands. There is no experimental research to benchmark the computational

results against and so a range of coordination numbers for all of the metals were initially probed to find the lowest energy coordination for each metal.

Coordination No.	Relative Energy/kJmol^{-1}		
	Cu(I)	Cu(II)	Ni(II)
2	0	0	0
3	/	-25.58	-79.35
4		-62.07	-113.41
5		-56.81	-137.53
6			-193.54

Table 16: Relative energies of the Cu and Ni BSRs with no bound H$_2$, compared with the two coordinate BSR, corrected for the differences in the number of hydrazine based ligands. /=structure did not optimise, shaded squares = no calculation was submitted on this structure.

For Ni(II) the octahedral six coordinate BSR is the most stable (Table 16). This BSR does not have a vacant coordination site to bind H$_2$. For Cu(II) the four coordinate BSR is the most stable but it was not possible to bind H$_2$ to this BSR. The implication for experiment is that, assuming hydrazide gels incorporate Ni(II) or Cu(II) centres with their most stable molecular coordination number, they would be poor hydrogen storage materials.

For Cu(I) the two coordinate BSR was the only one that could be converged (Table 16) and a maximum of two H$_2$ units were found to bind to it (Appendix 1 Figure 61 C) giving it a theoretical storage capacity of 4.27 %wt.[86] The M–H$_2$ interaction energy (method 3) of the first H$_2$ unit, -114.10 kJ mol^{-1}, is higher than those of four coordinate Ti(II) (-46.22 kJ mol^{-1}), V(II) (-37.33 kJ mol^{-1}) and Cr(II) (-37.75 kJ mol^{-1}) BSRs with only hydrazine based ligands (Appendix 1). However, the H–H bond has not broken suggesting that H$_2$ binding should be an easily reversible process. The experimental Cr(II) hydrazine linked material,[77] even with a M–H$_2$ interaction energy of over -40 kJmol^{-1}, only achieved a storage capacity of 3.2 %wt at 298 K without saturation at 170 bar. Therefore, even though the initial M–H$_2$ interaction energy is much higher than the ideal hydrogen storage enthalpy for room temperature applications (20 – 30 kJmol^{-1}) a higher M–H$_2$ interaction (~over -40 kJmol^{-1})

may be desirable in materials of this type, where the amount of hydrogen stored depends on the pressure applied, such that higher H_2 capacities are achieved at lower pressures (less than 170 bar).
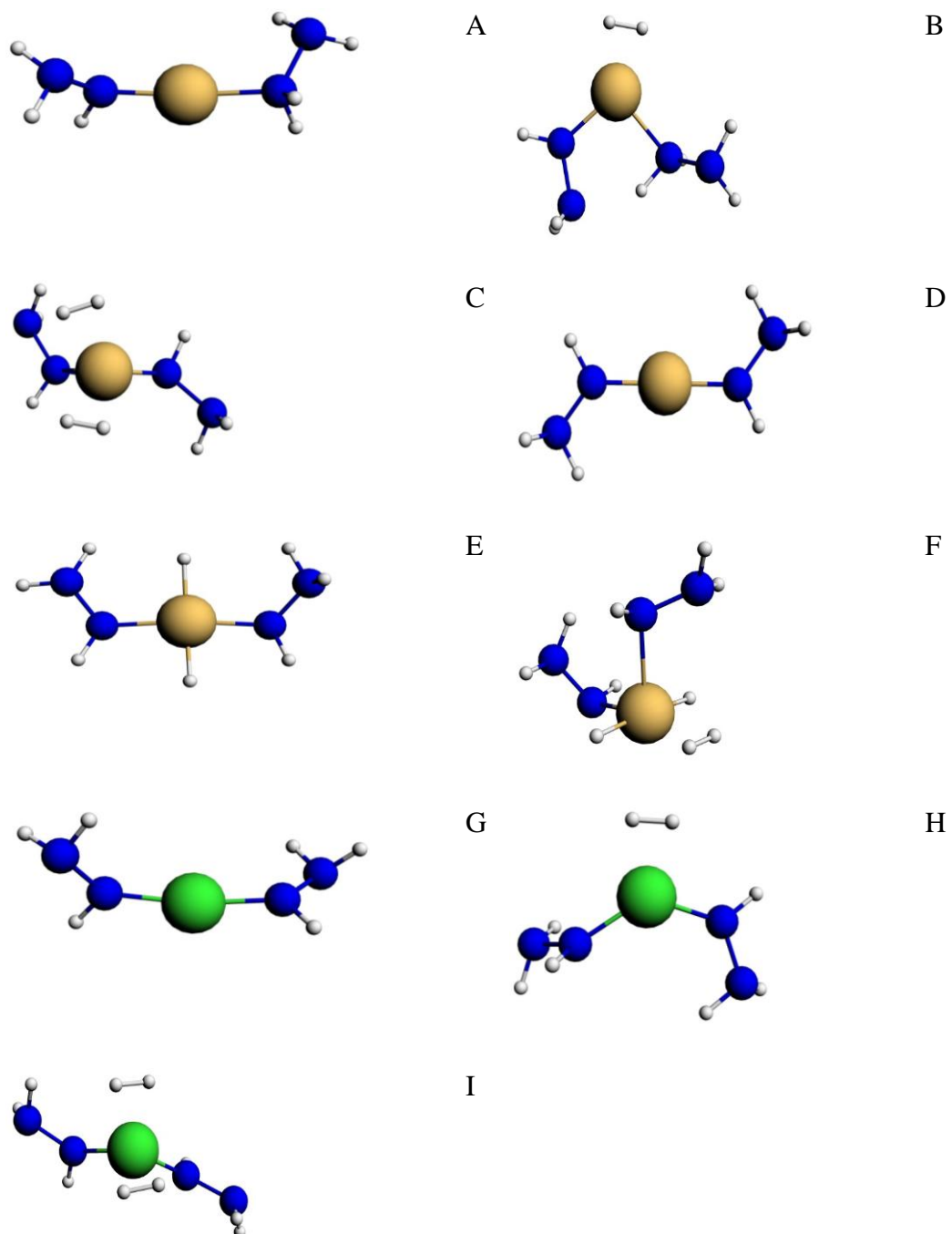
Figure 61: Ball and stick representations of hydrazine linked BSRs of Cu(I) with, A, zero, B, one and, C, two H_2 units bound; Cu(II) with, D, zero, E, one and, F, two H_2 units bound; Ni(II) with, G, zero, H, one and, I, two H_2 units bound. Key: H white, N blue, Cu pink, Ni green.

The bulk of the gel, surrounding the binding site, may permit metal coordination geometries other than the most stable found for isolated molecules. If this were the case and two coordinate binding sites were generated for Ni(II) and Cu(II), then this would alter the hydrogen storage properties of the materials. For example, the two coordinate Cu(II) BSRs bind up to two H_2 units with the first as two hydride ligands (Figure 61 F). Extrapolation to the bulk implies that half of the H_2 would be irreversibly bound so this is not encouraging. However, the Ni(II) two coordinate BSR binds up to two H_2 units in a similar fashion to the Cu(I) BSR (Figure 61 I) with a M–H_2 interaction energy of about -60 kJmol^{-1} (Appendix 1), giving a theoretical storage capacity of 6.76 %wt; potentially useful for H_2 storage.[86]

The H_2 molecule binds in a similar manner to the other studied hydrazine linked systems, i.e. through the Kubas interaction. Here, the H_2 bond length upon binding to the two coordinate Ni(II) and Cu(I) is between 0.808 – 0.877 Å with stretching frequency values between 3460 – 2720 cm^{-1} (Appendix 1). Molecular orbitals are present featuring the two synergic components of the Kubas interaction, the π-back donation (Figure 62 A) and the σ-donation (Figure 62 B).
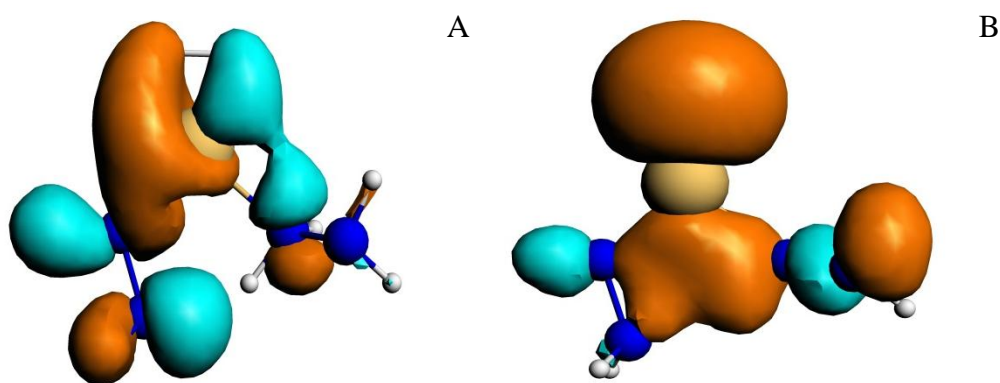
Figure 62: Three dimensional molecular orbitals of the Cu(I) BSR with one H_2 unit bound showing, A, HOMO-2 (π-back-donation) and, B, HOMO-26 (σ-donation).

From the QTAIM analysis the density at the BCP of the H_2 unit lies between $0.195 - 0.223$ e bohr^{-3} for the Ni(II) and Cu(I) BSRs (Appendix 1). This range is comparable to that of the BCP density of the H_2 unit in the classically Kubas systems[83] of between $0.202 - 0.219$ e bohr^{-3} (Table 3). This is in contrast to the early transition metal systems in which the BCP was higher than that of the classically Kubas systems suggesting a stronger H–H bond and thus a weaker Kubas interaction between the metal and the H_2. This is consistent with the stronger M–H_2 interactions found for Ni and Cu.

Considering the partial charge on the formally Cu(I) centre, figure 63 indicates that it either does not alter significantly or becomes slightly more positive as more H_2 units are bound, depending on the charge analysis method employed. This suggests that the M–H_2 interaction is a balance between the two synergic Kubas components or perhaps that the interaction has a slight excess of π-back-donation. This has been seen by Eckert and co-workers with extra framework Cu(I) binding hydrogen in zeolites.[45] π-back-donation could be even more substantial for Ni(II), for which almost all measures of the metal's partial charge become more positive as more H_2 units are bound (Figure 64). This contrasts with the early transition metals where there is either a balance between the two synergic components of the Kubas interaction, or slightly stronger σ-donation.
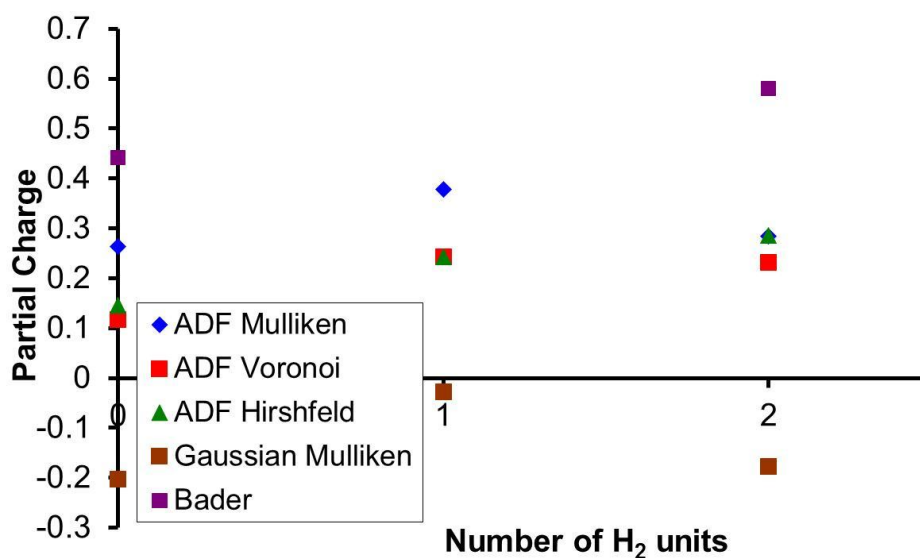
Figure 63: The partial charge on the Cu(I) in a two coordinate hydrazine linked BSR with only hydrazine based ligands as a function of the number of H_2 units bound.
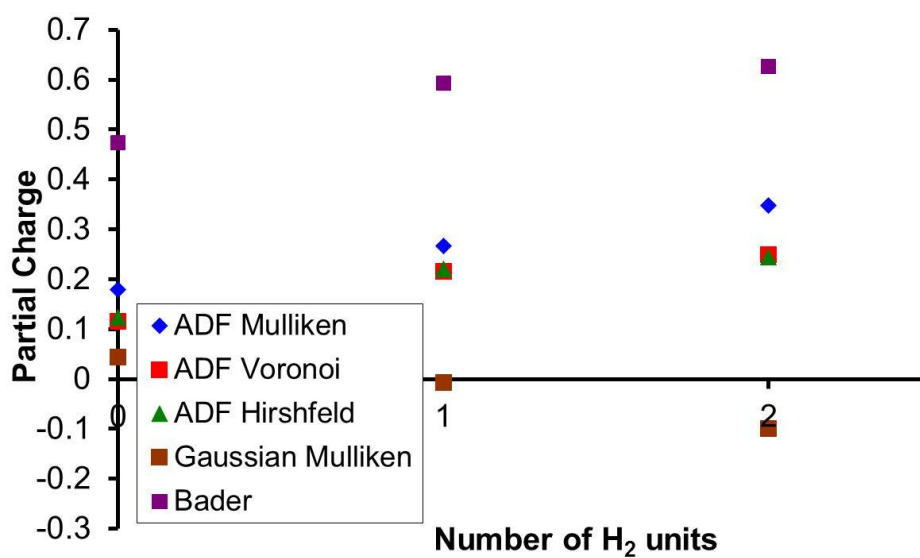
Figure 64: The partial charge on the Ni(II) in a two coordinate hydrazine linked BSR with only hydrazine based ligands as a function of the number of H_2 units bound.

The computational results suggested that the potentially experimentally realisable gels with Cu(I), Ni(II) or Cu(II) binding sites could be high capacity hydrogen storage materials. They could also be more stable and would also be cheaper than the early transition metal analogues and this work has encouraged the experimentalists to synthesise them.

Conclusions and Outlook

Computational models for molecular representations of the metal binding sites in the hydrazine linked and silica based hydrogen storage materials of the Antonelli group have been developed and the binding of H_2 to these representations has been studied. The results have been benchmarked against the available experimental data. Upon binding, the H–H bond is found to lengthen, its stretching frequency reduces, and the electron density and Laplacian of the electron density at the BCP decrease and become less negative respectively. These observations are consistent with a weakening of the H–H bond without breakage and suggest that the Kubas interaction describes the M–H_2 interaction in these materials. In all systems orbitals were present showing the two synergic components of the Kubas bond, the σ-donation from the H_2 molecule to the metal and the π-back-donation to the H_2 molecule from the metal. This corroborates the experimentalists' belief that the Kubas interaction accounts for the experimentally observed hydrogen binding enthalpies in the $20 - 50$ kJmol^{-1} range.

The partial charge on the metal as a function of the number of H_2 units bound was analysed using the Hirshfeld, Voronoi, Mulliken and Bader methods and generally it appeared that for early transition metals in the +3 oxidation state that the Kubas interaction between the metal and the H_2 is dominated by the σ-donation from the H_2 to the metal, such that the partial charge on the metal becomes less positive. For early transition metals in the +2 oxidation state the interaction is generally a balance between the σ-donation and the π-back-donation, such that the partial charge on the metal does not alter significantly. For late transition metals the Kubas interaction is generally dominated by the π-back-donation from the metal to the H_2 molecule such that the partial charge on the metal becomes more positive. This shows the ability of the H_2 molecule, when bonding through the Kubas interaction, to be stable on electron poor as well as electron rich centres. Moving from an electron poor to an electron rich centre the Kubas interaction becomes more π-back-donating in character.

The calculations were extended to alter the metal and the ancillary ligands of these BSRs in order to provide input to the experimental research. For all systems, altering the ancillary ligand to a poorer π-acceptor increased the strength of the M–H$_2$ interaction as more electron density was then available to π-back-donate to the H$_2$ molecule. Changing the metal did not affect the M–H$_2$ interaction energy as much as altering the ancillary ligand and any pattern in the M–H$_2$ interaction energies as a function of metal was not independent of the ancillary ligand. For the hydrazine linked systems moving across the periodic table from Ti to V to Cr to Mn reduces the number of H$_2$ units that could be bound, and for the silica systems it is generally harder to bind H$_2$ units to Cr centres. It appears that Cr and Mn would be a poor choices as the metal centre in hydrogen storage materials. Late first row transition metals Cu(I), Cu(II) and Ni(II) were also investigated due to their potential to form more stable hydrazine linked gels. These initial calculations suggest that they may form promising H$_2$ storage materials, especially Cu(I).

The experimentally observed rising enthalpies with increasing H$_2$ coverage were computationally reproduced in the silica based and V(III) mono-metallic hydrazine linked models, however a definitive explanation for them remains elusive. In the silica systems it is suggested that, as the binding sites are spread out over the silica material, it is a local effect. It is thought that the perturbation of the binding site's frontier molecular orbitals by one H$_2$ molecule alters them in such a way that their energies are closer to those of the H$_2$ molecule such that binding the next H$_2$ molecule is more favourable. Conversely with the hydrazine linked materials where the binding sites are very close to each other it is suggested that M–M interactions influence the binding of the H$_2$ such that the binding of the H$_2$ at one metal makes it more favourable for the H$_2$ to bind at another metal.

In order to extend the experimental research, inelastic neutron scattering at high pressures on the hydrazine gels would add further evidence for the presence of the Kubas interaction by searching for the rotational transitions of the Kubas bound H$_2$ molecules. The rising enthalpies with increasing H$_2$ coverage also require further investigation. For example, Antonelli's theory[78] that the

rising enthalpies are due to a pressure induced deformation may be investigated by a spectroscopic study as the pressure is altered to seek evidence for such a deformation. This could be complemented with further computational studies, perhaps involving molecular dynamics simulations of the structure without hydrogen at different pressures in order to plot the change in the structure as a function of pressure.

Although the hydrogen storage materials, that have been studied here computationally, are not suitable for practical applications, due to their unstable and at times pyrophoric nature, they do represent progress towards such a material. Compared to hydrogen storage materials that only physisorb hydrogen, they have higher hydrogen absorption enthalpies meaning that they retain more hydrogen at room temperature and this has been linked to the incorporation of transition metal binding sites. Methods of fine tuning the binding of the hydrogen, through the Kubas interaction, have been studied computationally. The binding of the hydrogen has been found to be increased by having ligands bound to the transition metals that are poor π-acceptors. This result was applied to the hydrazine linked materials by incorporating hydride ligands, which are poor π-acceptors, bound to the metal centres. The incorporation of the hydride ligands did indeed increase the hydrogen binding enthalpy of the materials. However, this result is general and may be applied to other systems where the activation of hydrogen through binding to transition metal centres is required such as in hydrogenation catalysts or the catalyst of any reaction requiring the breaking of the H–H bond such as those for the Haber process. The result may also be relevant to the activation of the C=C double bond on a transition metal centre as this bond interacts with a transition metal in a similar fashion to the H-H bond and so to the area of polymerisation catalysis, for example.

Ligand	No. H₂ bound	Value of average H–H bond length/Å						Value of H–H stretching frequency/cm⁻¹						Value of imaginary frequency/cm⁻¹					
		BSR with 1 ligand			BSR with 2 ligands			BSR with 1 ligand			BSR with 2 ligands			BSR with 1 ligand			BSR with 2 ligands		
		Ti^{3+}	V^{3+}	Cr^{3+}	Ti^{3+}	V^{3+}	Cr^{3+}	Ti^{3+}	V^{3+}	Cr^{3+}	Ti^{3+}	V^{3+}	Cr^{3+}	Ti^{3+}	V^{3+}	Cr^{3+}	Ti^{3+}	V^{3+}	Cr^{3+}
Hydride	1	0.827	0.812	0.782	0.815	0.834	0.764	3131	3364	3834	3313	3103	4120	0	0	153i, 56i	0	0	0
	2	0.788 0.779	0.793 0.788	0.797 0.796	0.813 0.807	0.827 0.814	/	3841 3687	3731 3645	3625 3611	3428 3340	3367 3187	/	0	27i, 7i	156i, 71i	0	0	0
	3	/	0.792 0.788 0.776	0.818 0.801 0.782	0.813 0.800 0.787	/	/	/	3923 3722 3661	3856 3555 3312	3707 3524 3351	/	/	/	38i, 22i	155i, 67i	0	/	/
	4	/	/	/	0.803 0.802 0.785 0.777	/	/	/	/	/	3893 3751 3514 3475	/	/	/	/	/	0	/	/
Methyl	1	0.807	0.796	0.769	0.810	0.796	0.781	3398	3599	4049	3353	3590	3845	0	26i	39i	0	13i	0
	2	0.783 0.776	0.784 0.774	0.774 0.769	0.781 0.780	0.783 0.777	0.785 0.780	3896 3769	3965 3788	4086 3962	3843 3790	3903 3803	3876 3805	18i	27i	39i	0	31i	18i
	3	/	/	0.790 0.784 0.778	0.790 0.778 0.773	0.801 0.783 0.780	0.806 0.797 0.790	/	/	3908 3811 3721	3962 3869 3641	3849 3806 3547	3726 3606 3480	/	/	36i, 9i	0	24i	/
	4	/	/	/	0.780 0.779 0.777 0.774	/	/	/	/	/	3924 3871 3853 3836	/	/	/	/	/	5i	/	/

		H–H bond lengths						Stretching frequencies						Imaginary frequencies					
Allyl	**1**	0.783			0.779			3793			3843			12i			0		
	2	0.782 0.777			0.794 0.776			3862 3782			3906 3621			9i			0		
	3	0.788 0.776 0.769			0.798 0.781 0.774			4049 3884 3686			3945 3789 3553			10i			21i		
	4	/			0.782 0.778 0.774 0.772			/			3955 3943 3868 3803			/			0		
Benzyl	**1**	0.787	0.790	0.770	0.792	0.785	0.773	3721	3685	4036	3635	3766	3967	22i	2i	0	13i	31i, 17i	22i
	2	0.773 0.772	0.780 0.776	/	0.786 0.777	0.781 0.781	/	3972 3959	3932 3852	/	3888 3730	3847 3832	/	24i	0	/	12i	0	24i
	3	0.784 0.776 0.768	/	/	0.788 0.786 0.780	0.786 0.786 0.781	/	4048 3883 3762	/	/	3827 3752 3669	3843 3770 3754	/	25i, 12i	/	/	0	0	25i, 12i
	4	/	/	/	0.776 0.776 0.775 0.773	/	/	/	/	/	3947 3912 3902 3893	/	/	/	/	/	0	/	/

Table 17A: All of the silica based BSRs with the values of their H–H bond lengths and stretching frequencies and imaginary frequencies.

/ = structure did not optimise

Shaded squares = no calculation was submitted on this structure

		M–H$_2$ interaction energies/kJmol^{-1}					
		BSR with 1 ligand			BSR with 2 ligands		
Ancillary ligand	No. H$_2$ bound	Ti^{3+}	V^{3+}	Cr^{3+}	Ti^{3+}	V^{3+}	Cr^{3+}
Hydride	1	-47.54	-43.28	-23.27	-50.77	-64.14	-9.10
	2	-30.42	-24.16	-10.45	-48.69	-67.10	/
	3	/	-25.30	-33.14	-47.35	/	/
	4	/	/	/	-44.13	/	/
Methyl	1	-23.67	-29.95	-12.94	-23.57	-40.24	-19.33
	2	-5.03	-15.59	-16.27	-16.88	-24.58	-15.46
	3	/	/	-20.11	-14.81	-31.54	-19.89
	4	/	/	/	-21.09	/	/
Allyl	1	-13.11			-12.48		
	2	-19.84			-19.34		
	3	-8.94			-12.82		
	4	/			-19.00		
Benzyl	1	-15.95	-18	nc	-25.62	nc	nc
	2	-0.07	-15.15	/	-14.37	nc	/
	3	-7.49	/	/	-17.86	nc	/
	4	/	/	/	-14.80	/	/

Table 18A: All of the silica based BSRs with the values of their M(III)–H$_2$ interaction energies (method 3).

/ = structure did not optimise.

Shaded squares = no calculation submitted on this structure.

nc = M(III)–H$_2$ interaction energy could not be calculated

		M–H$_2$ interaction energies/kJmol^{-1}	
		BSR with 1 ligand	BSR with 2 ligands
Ancillary ligand	No. H$_2$ bound	Ti^{3+}	Ti^{3+}
Hydride	1	-52.91	-56.38
	2	-33.15	-53.75
	3	/	-50.00
	4	/	-37.91
Methyl	1	-29.42	-30.17
	2	-7.56	-19.19
	3	/	-16.57
	4	/	-26.29
Allyl	1	-16.56	-15.46
	2	-23.10	-20.89
	3	-11.87	-15.02
	4	/	-19.73
Benzyl	1	-20.60	-20.35
	2	-4.95	-18.42
	3	-10.82	-20.64
	4	/	-19.73

Table 19A: The Ti(III) silica based BSRs with the values of their M(III)–H$_2$ interaction energies (method 2).

Ligand	No. of H$_2$ bound	H–H bond lengths/Å			H–H stretching frequencies/cm^{-1}			M–H$_2$ interaction energies/kJmol^{-1}			H–H BCP densities/ebohr^{-3}		
		Ti^{3+}	V^{3+}	Cr^{3+}	Ti^{3+}	V^{3+}	Cr^{3+}	Ti^{3+}	V^{3+}	Cr^{3+}	Ti^{3+}	V^{3+}	Cr^{3+}
THF	1	0.786	0.786	0.795	3723	3755	3624	-21.11	-17.99	-26.49	0.238	0.240	0.235
	2	0.786 0.787	0.785 0.787	0.770 0.789	3731 3714	3764 3726	4013 3715	-20.37	-19.30	-12.78	0.238 0.239	0.240 0.238	0.247 0.238
Hydrazine based	1	0.797	0.781	0.784	3524	3817	3779	-33.95	-15.48	-18.88	0.231	0.241	0.239
	2	0.782 0.781	0.791 0.799	0.791 0.805	3776 3764	3662 3524	3671 3477	-19.80	-29.18	-30.76	0.239 0.239	0.236 0.231	0.236 0.229
1,3-dimethylallyl	1	0.782	0.785	0.787	3798	3750	3734	-16.15	-18.43	-20.83	0.241	0.240	0.238
	2	0.774 0.782	0.790 0.788	/	3925 3792	3714 3703	/	-12.57	-21.20	/	0.245 0.240	0.238 0.238	/
(trimethylsilyl)methyl	1	0.788	0.783	0.792	3666	3780	3656	-23.89	-16.84	-25.32	0.237	0.240	0.236
	2	0.773 0.775	0.781 0.782	0.781 0.791	3913 3921	3848 3801	3839 3675	-9.86	-14.27	-18.90	0.244 0.244	0.242 0.241	0.242 0.237
Hydride	1	0.796	0.800	0.802	3560	3523	3513	-30.71	-34.51	-36.29	0.233	0.231	0.230
	2	0.788 0.793	0.814 0.789	0.822 0.804	3692 3624	3313 3693	3240 3484	-27.68	-35.46	-45.32	0.237 0.232	0.224 0.237	0.221 0.230
2 hydrides	1	0.805	0.801	0.809	3436	3525	3411	-37.95	-34.02	-44.05	0.229	0.231	0.226
	2	0.801 0.815	0.797 0.822	0.784 0.813	3481 3314	3581 3246	3783 3354	-41.50	-43.58	-34.10	0.230 0.224	0.233 0.220	0.238 0.224
	3	0.799 0.807 0.808	0.803 0.803 0.892	/	3520 3404 3421	3497 3476 2474	/	-40.19	-65.48	/	0.231 0.226 0.226	0.230 0.230 0.188	/
	4	0.804 0.834 0.837 1.812	/		3483 3072 3010 absent	/		N/A	/		0.229 0.214 0.212 absent	/	

Table 20A: All of the four coordinate M(III) hydrazine linked BSRs with the values of their H–H bond lengths, stretching frequencies and BCP densities and M(III)–H_2 interaction energies (method 4).

/ = structure did not optimise

Shaded squares = no calculation was submitted on this structure

Ligand	No. of H_2 bound	H–H bond lengths/Å			H–H stretching frequencies/cm^{-1}			M–H_2 interaction energies/$kJmol^{-1}$			H–H BCP densities/$ebohr^{-3}$		
		Ti^{3+}	V^{3+}	Cr^{3+}	Ti^{3+}	V^{3+}	Cr^{3+}	Ti^{3+}	V^{3+}	Cr^{3+}	Ti^{3+}	V^{3+}	Cr^{3+}
Hydrazine based	1	0.816	0.795	0.777	3245	3576	3888	-53.59	-32.01	-14.14	0.221	0.232	0.242
	2	0.775 0.791	0.781 0.786	0.767 2.403	3916 3630	3813 3745	4062 absent	-17.96	-17.50	N/A	0.245 0.235	0.241 0.239	0.247 absent
	3	0.794 0.784 0.774	0.783 0.788 0.791	0.816 0.823 0.875	3580 3735 3941	3797 3710 3620	3323 3220 2623	-20.32	-22.84	-72.72	0.233 0.238 0.245	0.240 0.238 0.234	0.223 0.219 0.194
1,3-dimethylallyl	1	0.808	0.785	0.783	3366	3729	3792	-44.27	-22.62	-19.46	0.226	0.237	0.239
	2	0.777 0.794	0.784 0.792	0.808 0.809	3849 3600	3779 3634	3420 3420	-21.78	-20.98	-39.61	0.242 0.234	0.241 0.236	0.228 0.228
	3	/	/	0.770 0.810 0.811	/	/	4008 3405 3373	/	/	-31.14	/	/	0.244 0.227 0.227
(trimethylsilyl)methyl	1	0.809	0.787	0.774	3355	3711	3939	-43.76	-22.56	-10.86	0.226	0.237	0.244
	2	0.777 0.789	0.783 0.789	0.784 0.807	3871 3667	3802 3683	3787 3457	-17.05	-21.21	-28.61	0.244 0.237	0.24 0.2360	0.240 0.229
	3	0.819 0.806 1.930	0.817 0.825 1.753	0.777 0.800 0.816	3264 3447 absent	3292 3206 absent	3901 3556 3314	N/A	N/A	-30.10	0.221 0.228 absent	0.225 0.219 absent	0.243 0.232 0.224

Hydride	1	0.836	0.814	0.767	3005	3312	4061	-70.66	-49.77	-3.77	0.212	0.223	0.248
	2	0.798 0.806	0.778 0.829	0.803 0.856	3530 3412	3868 3136	3486 2833	-37.52	-38.60	-63.99	0.231 0.227	0.242 0.216	0.228 0.204
	3	0.775 0.793 0.804	0.796 0.814 0.817	0.875 0.882 0.899	3905 3625 3436	3548 3338 3318	2652 2597 2414	-27.33	-46.04	-117.13	0.242 0.234 0.228	0.230 0.223 0.222	0.196 0.193 0.184
	4	0.791 0.814 0.821 1.990	0.828 0.830 0.847 1.633	/	3659 3345 3236 absent	3180 3143 2900 absent	/	N/A	N/A	/	0.234 0.223 0.219 absent	0.216 0.214 0.207 absent	/
2 hydrides	1	0.810	0.804	0.893	3368	3484	2491	-43.12	-36.17	-119.94	0.226	0.230	0.190
	2	0.798 0.812	0.803 0.828	0.809 0.814	3547 3349	3508 3170	3443 3362	-37.62	-49.07	-44.43	0.233 0.226	0.230 0.217	0.227 0.224
	3	0.797 0.806 0.813	0.789 0.797 0.818	0.799 0.814 0.824	3554 3439 3349	3713 3594 3292	3557 3368 3224	-38.83	-35.36	-40.42	0.232 0.229 0.225	0.237 0.233 0.221	0.231 0.232 0.220
	4	0.786 0.793 0.813 0.831	0.815 0.847 0.847 0.849	/	3739 3631 3342 3109	3296 2965 2952 2855	/	-41.28	-77.20	/	0.237 0.234 0.223 0.215	0.221 0.206 0.206 0.205	/
	5	0.812 0.822 0.834 0.841 1.843	/		3372 3230 3079 2975 absent	/		N/A	/		0.225 0.220 0.214 0.211 absent	/	

Table 21A: All of the three coordinate M(III) hydrazine linked BSRs with the values of their H–H bond lengths, stretching frequencies and BCP densities and M(III)–H_2 interaction energies (method 4).

/ = structure did not optimise

Shaded squares = no calculation was submitted on this structure

		H–H bond lengths/Å			H–H stretching frequencies/cm⁻¹			M–H₂ interaction energies/kJmol⁻¹			H–H BCP densities/ebohr⁻³		
Ligand	No. of H_2 bound	Ti^{3+}	V^{3+}	Cr^{3+}	Ti^{3+}	V^{3+}	Cr^{3+}	Ti^{3+}	V^{3+}	Cr^{3+}	Ti^{3+}	V^{3+}	Cr^{3+}
THF	1	0.796	0.778	0.784	3527	3874	3779	-33.45	-11.89	-15.81	0.231	0.243	0.240
Hydrazine based	1	0.787	0.786	0.791	3671	3742	3673	-25.82	-20.43	-24.04	0.236	0.238	0.237
1,3-dimethylallyl	1	0.791	0.802	0.799	3638	3488	3549	-27.01	-37.25	-32.29	0.235	0.229	0.232
(trimethylsilyl)methyl	1	0.799	0.781	0.789	3508	3812	3691	-39.17	-16.04	-19.55	0.228	0.241	0.237
Hydride	1	0.802	0.800	0.799	3451	3512	3535	-39.06	-36.28	-34.73	0.228	0.230	0.231
2 hydrides	1	0.815	0.815	0.798	3272	3296	3566	-51.96	-52.09	-33.64	0.222	0.222	0.232
	2	0.795 0.809	0.835 0.879	/	3550 3557	3039 3529	/	-38.83	-94.69	/	0.233 0.224	0.212 0.191	/
	3	0.815 0.845 1.871	/		3315 2911 absent	/		N/A	/		0.222 0.209 absent	/	

Table 22A: All of the five coordinate M(III) hydrazine linked BSRS with the values of their H–H bond lengths, stretching frequencies and BCP densities and M(III)–H_2 interaction energies (method 4).

/ = structure did not optimise

Shaded squares = no calculation was submitted on this structure

		H–H bond lengths/Å			H–H stretching frequencies/cm^{-1}			M–H$_2$ interaction energies/kJmol^{-1}			H–H BCP densities/e bohr^{-3}		
Ligand	No. of H$_2$ bound	Ti^{2+}	V^{2+}	Cr^{2+}	Ti^{2+}	V^{2+}	Cr^{2+}	Ti^{2+}	V^{2+}	Cr^{2+}	Ti^{2+}	V^{2+}	Cr^{2+}
(trimethylsilyl)methyl	1	0.813	0.795	0.784	3278	3580	3783	-31.32	-30.09	-28.33	0.222	0.233	0.239
	2	0.803 0.805	0.790 0.809	/	3456 3364	3645 3372	/	-40.33	-23.34	/	0.227 0.225	0.234 0.225	/
	3	0.805 0.840 2.159	/		3404 2965 N/A	/		-217.32	/		0.225 0.206 N/A	/	
Hydride	1	0.810	0.837	0.811	3342	3004	3377	-44.11	-54.33	-48.52	0.224	0.211	0.225
	2	0.788 0.806	0.792 0.803	/	3700 3408	3632 3485	/	-41.78	-33.34	/	0.237 0.226	0.229 0.234	/
	3	0.794 0.798 0.800	/		3606 3535 3468	/		-26.58	/		0.234 0.230 0.229	/	
2 hydrides	1	0.810	0.816	0.818	3359	3296	3308	-59.69	-61.16	-68.78	0.224	0.223	0.223
	2	0.809 0.810	0.810 0.819	/	3383 3333	3380 3264	/	-42.16	-51.28	/	0.225 0.224	0.226 0.222	/
	3	0.802 0.816 0.822	/		3463 3276 3183	/		-35.57	/		0.229 0.222 0.217	/	
Hydrazine based	1	0.828	0.795	0.792	3062	3574	3636	-46.22	-37.33	-37.75	0.212	0.232	0.234
	2	0.792 0.809	0.782 0.808	/	3593 3333	3769 3386	/	-58.18	-8.93	/	0.224 0.234	0.239 0.227	/
THF	1	0.810	0.802		3304	3465		-31.43	-49.00		0.223	0.228	
	2	0.792 0.817	0.794 0.803		3595 3225	3590 3465		-45.78	-27.49		0.233 0.219	0.233 0.229	

Table 23A: All of the four coordinate M(II) hydrazine linked BSRs with the values of their H–H bond lengths, stretching frequencies and BCP densities and M(II)–H_2 interaction energies (method 3).

/ = structure did not optimise

Shaded squares = no calculation was submitted on this structure

Ligand	No. of H_2 bound	H–H bond lengths/Å			H–H stretching frequencies/cm^{-1}			M–H_2 interaction energies/kJmol^{-1}			H–H BCP densities/ebohr^{-3}		
		Ti^{2+}	V^{2+}	Cr^{2+}	Ti^{2+}	V^{2+}	Cr^{2+}	Ti^{2+}	V^{2+}	Cr^{2+}	Ti^{2+}	V^{2+}	Cr^{2+}
(trimethylsilyl)methyl	1	0.799	0.795	0.788	3481	3585	3728	-30.36	-40.33	-43.50	0.231	0.233	0.238
	2	0.793 0.830	0.789 0.805	/	3594 3054	3704 3429	/	-36.27	-36.14	/	0.234 0.214	0.237 0.227	/
	3	0.802 0.800 0.806	0.798 0.798 0.801		3498 3444 3376	3572 3556 3497		-34.90	-23.47		0.230 0.228 0.227	0.233 0.232 0.231	
	4	0.801 0.803 0.819 3.940	/		3480 3464 3263	/		-171.16	/		0.228 0.228 0.220	/	
Hydride	1	0.807	0.798	2.474	3347	3517	N/A	-34.71	-38.73	-542.36	0.225	0.230	N/A
	2	0.814 0.821	0.798 0.799	0.806 2.529	3299 3188	3547 3516	3455	-51.67	-38.13	-296.61	0.223 0.219	0.230 0.229	0.228
	3	0.802 0.815 0.817	0.794 0.803 0.811	/	3442 3273 3234	3612 3492 3359	/	nc	-41.67	/	0.226 0.222 0.221	0.233 0.229 0.224	/
	4	0.791	/		3643	/		-31	/		0.234	/	

		0.793 0.796 0.800		▨	3600 3571 3505		▨			▨	0.230 0.233 0.232		▨
2 hydrides	1	0.808	0.815	0.819	3376	3317	3284	-51.80	-64.95	-72.15	0.226	0.224	0.223
	2	0.801 0.825	0.799 0.824	0.773 0.810	3491 3148	3546 3183	3965 3406	-49.57	-48.32	-39.99	0.230 0.216	0.231 0.217	0.243 0.226
	3	0.803 0.805 0.830	0.804 0.808 0.819	/	3479 3447 3086	3477 3406 3249	/	-50.17	nc	/	0.229 0.228 0.213	0.228 0.225 0.220	/
	4	0.802 0.808 0.817 0.824	/	▨	3498 3386 3287 3163	/	▨	-46.30	/	▨	0.229 0.225 0.222 0.216	/	▨
Hydrazine based	1	0.829	0.796	0.783	3138	3545	3764	-52.18	nc	-20.78	0.215	0.232	0.238
	2	0.791 0.817	0.805 0.806	0.786 0.791	3611 3227	3430 3385	3737 3631	-23.04	-30.53	-33.49	0.235 0.220	0.227 0.226	0.237 0.233
	3	0.782 0.791 0.809	0.790 0.805 0.805	/	3780 3637 3352	3683 3447 3425	/	-30.64	-22.07	/	0.240 0.234 0.224	0.237 0.229 0.228	/
THF	1	0.807	0.813	0.779	3366	3296.45	3839	nc	-54.58	-19.02	0.226	0.223	0.241
	2	0.798 0.818	0.786 0.803	0.770 2.465	3478 3198	3718 3452	4001 N/A	-19.84	nc	-283.72	0.230 0.220	0.237 0.229	N/A
	3	0.780 0.790 0.805	0.789 0.799 0.803	/	3855 3636 3413	3711 3541 3468	/	-37.14	-23.66	/	0.243 0.234 0.227	0.238 0.233 0.230	/

Table 24A: All of the three coordinate M(II) hydrazine linked BSRS with the values of their H–H bond lengths, stretching frequencies and BCP densities and M(II)–H_2 interaction energies (method 3).

/ = structure did not optimise

Shaded squares = no calculation was submitted on this structure

Ligand	No. of H$_2$ bound	H–H bond lengths/Å			H–H stretching frequencies/cm^{-1}			M–H$_2$ interaction energies/kJmol^{-1}			H–H BCP densities/ebohr^{-3}		
		Ti^{2+}	V^{2+}	Cr^{2+}	Ti^{2+}	V^{2+}	Cr^{2+}	Ti^{2+}	V^{2+}	Cr^{2+}	Ti^{2+}	V^{2+}	Cr^{2+}
(trimethylsilyl)methyl	1	0.802	0.801	/	3422	3488	/	-28.28	-34.88	/	0.228	0.229	/
Hydride	1	0.813	0.790	/	3277	3663	/	-47.61	-15.5	/	0.221	0.236	/
2 hydrides	1	0.820	0.832	/	3224	3062	/	-64.72	-57.23	/	0.219	0.213	/
	2	0.809 0.815	/		3360 3281	/		-49.91	/		0.224 0.222	/	
Hydrazine based	1	0.814	0.797	/	3271	3536	/	-65.34	-18.42	/	0.220	0.231	/
THF	1	0.827	0.817	/	3083	3237	/	-56.77	-45.41	/	0.214	0.221	/

Table 25A: All of the five coordinate M(II) hydrazine linked BSRs with the values of their H–H bond lengths, stretching frequencies and BCP densities and M(II)–H$_2$ interaction energies (method 3).

/ = structure did not optimise

Shaded squares = no calculation was submitted on this structure

	H–H bond lengths/Å				H–H stretching frequencies/cm⁻¹				M–H₂ interaction energies/kJmol⁻¹				H–H BCP densities/e bohr⁻³			
No. of H₂ bound	Ti²⁺	V²⁺	Cr²⁺	Ti²⁺H	Ti²⁺	V²⁺	Cr²⁺	Ti²⁺H	Ti²⁺	V²⁺	Cr²⁺	Ti²⁺H	Ti²⁺	V²⁺	Cr²⁺	Ti²⁺H
1 & 0	0.817	0.809	0.786	0.803	3188	3431	3750	3439	-42.33	-44.3	-28.13	-40.10	0.218	0.227	0.238	0.228
1 & 1	0.817	0.790	0.789	0.807	3590	3655	3692	3381	-29.03	-34.85	-32.09	-38.71	0.233	0.235	0.223	0.226
		0.801	0.809	0.814	3406	3460	3368	3273					0.227	0.229	0.236	0.222
1 & 2	0.789	0.787	/	0.788	3635	3714	/	3694	-34.61	-36.49	/	-26.40	0.223	0.237	/	0.236
	0.810	0.801		0.810	3332	3485		3339	(nc)	(-34.71)		(-32.47)	0.234	0.229		0.225
	0.803	0.801		0.817	3405	3467		3221					0.227	0.229		0.219
2 & 2	0.771	0.784	/	0.789	3989	3764.	/	3653	-30.69	-32.40	/	-47.42	0.246	0.239	/	0.235
	0.791	0.784		0.800	3619	3747		3477					0.234	0.238		0.229
	0.794	0.799		0.818	3568	3529		3229					0.232	0.231		0.221
	0.823	0.801		0.831	3127	3475		3052					0.215	0.229		0.214

Table 26A: M(II) lowest energy dimers with the values of their H–H bond lengths, stretching frequencies and BCP densities and M(II)–H₂ interaction energies (method 3). The number of H₂ units bound shows the number bound to each of the metals separately. The M–H₂ interaction energies in brackets are the average energy of binding of all three H₂ units. The interaction energy not in brackets in the same box is the average energy of binding two H₂ units to one of the metals.

/=structure did not optimise

Ti²⁺H=dimer with hydride ancillary ligands.

nc=M(II)–H₂ interaction energy could not be calculated

Mn²⁺ lowest energy dimer H–H bond length = 1.948 Å and M–H₂ interaction energy = -468.93 kJmol⁻¹

	H–H bond lengths/Å				H–H stretching frequencies/cm^{-1}				M–H$_2$ interaction energies/kJmol^{-1}				H–H BCP densities/e bohr^{-3}			
No. of H$_2$ bound	Ti^{3+}	V^{3+}	Cr^{3+}	Ti^{3+}H	Ti^{3+}	V^{3+}	Cr^{3+}	Ti^{3+}H	Ti^{3+}	V^{3+}	Cr^{3+}	Ti^{3+}H	Ti^{3+}	V^{3+}	Cr^{3+}	Ti^{3+}H
1 & 0	0.773	0.771	0.779	0.772	3956	3971	3847	3969	-12.03	-9.97	-16.83	-47.83	0.246	0.245	0.242	0.207
1 & 1	0.782 0.791	0.771 0.779	0.774 0.775	0.808 0.810	3787 3603	3985 3852	3936 3936	3397 3369	-16.82	-18.28	-13.47	-31.2	0.240 0.233	0.246 0.242	0.244 0.244	0.226 0.225
1 & 2	0.769 0.775 0.782	0.770 0.779 0.780	/	0.781 0.797 0.805	4009 3899 3757	4012 3836 3817	/	3798 3535 3414	-14.50 (-14.20)	-14.16 (-16.97)	/	-24.44 (-26.42)	0.246 0.244 0.239	0.247 0.241 0.241	/	0.240 0.231 0.227
2 & 2	0.774 0.778 0.782 0.788	/	/	0.790 0.792 0.796 0.809	3911 3841 3769 3664	/	/	3646 3604 3522 3370	-18.15	/	/	-29.87	0.244 0.242 0.239 0.236	/	/	0.234 0.239 0.230 0.225

Table 27A: All of the M(III) lowest energy dimers with the values of their H–H bond lengths, stretching frequencies and BCP densities and M(III)–H$_2$ interaction energies (method 3). The number of H$_2$ units bound shows the number bound to each of the metals separately. The M(III)–H$_2$ interaction energies in brackets are the average energy of binding of all three H$_2$ units. The interaction energy not in brackets in the same box is the average energy of binding two H$_2$ units to one of the metals.

/=structure did not optimise

Ti^{3+}H=dimer with hydride ancillary ligands.

	H–H bond lengths/Å		H–H stretching frequencies/cm^{-1}		M–H$_2$ interaction energies/kJmol^{-1}		H–H BCP densities/e bohr^{-3}	
No. of H$_2$ bound	**1**	**2**	**1**	**2**	**1**	**2**	**1**	**2**
Cu(I)	0.877	0.808 0.821	2720	3460 3298	-114.10	-56.37	0.195	0.223 0.217
Cu(II)	3.103	0.809 3.099	N/A	3457 N/A	-502.22	/	N/A	0.224 N/A
Ni(II)	0.847	0.832 0.832	2996	3185 3146	-59.24	-60.36	0.206	0.212 0.212

Table 28A: All of the two coordinate late transition metal BSRs with the values of their H–H bond lengths, stretching frequencies and BCP densities and M–H$_2$ interaction energies (method 3).

/=structure did not optimise.

Ligand	No. H$_2$ bound	ADF Voronoi BSR with 1 ligand			BSR with 2 ligands			ADF Hirshfeld BSR with 1 ligand			BSR with 2 ligands			ADF Mulliken BSR with 1 ligand			BSR with 2 ligands		
		Ti^{3+}	V^{3+}	Cr^{3+}	Ti^{3+}	V^{3+}	Cr^{3+}	Ti^{3+}	V^{3+}	Cr^{3+}	Ti^{3+}	V^{3+}	Cr^{3+}	Ti^{3+}	V^{3+}	Cr^{3+}	Ti^{3+}	V^{3+}	Cr^{3+}
Hydride	0	0.416	0.346	0.601	0.360	0.339	0.588	0.536	0.432	0.565	0.460	0.435	0.516	1.168	1.055	1.024	1.052	0.944	0.867
	1	0.315	0.256	0.548	0.276	0.272	0.542	0.499	0.433	0.555	0.405	0.382	0.509	1.233	1.154	1.007	1.064	0.959	0.831
	2	0.275	0.197	0.496	0.235	0.223	/	0.444	0.396	0.559	0.355	0.331	/	1.108	1.090	1.043	1.026	0.932	/
	3	/	0.167	0.465	0.212	/	/	/	0.360	0.525	0.314	/	/	/	1.026	0.927	0.879	/	/
	4	/	/	/	0.213	/	/	/	/	/	0.353	/	/	/	/	/	0.833	/	/
Methyl	0	0.396	0.319	0.567	0.374	0.305	0.518	0.5553	0.462	0.603	0.552	0.469	0.571	1.224	1.085	1.030	1.145	1.000	0.862
	1	0.293	0.237	0.516	0.283	0.212	0.474	0.5257	0.454	0.590	0.539	0.438	0.555	1.263	1.154	0.992	1.210	1.041	0.799
	2	0.233	0.178	0.475	0.217	0.140	0.439	0.4936	0.420	0.57	0.491	0.388	0.563	1.198	1.096	0.948	1.151	1.028	0.782
	3	/	/	0.448	0.193	0.102	0.420	/	/	0.567	0.455	0.346	0.531	/	/	0.885	1.038	0.882	0.705
	4	/	/	/	0.171	/	/	/	/	/	0.423	/	/	/	/	/	0.779	/	/
Allyl	0	0.340			0.283			0.5127			0.451			1.227			1.067		
	1	0.281			0.247			0.4991			0.424			1.924			0.881		
	2	0.258			0.210			0.4673			0.430			1.126			0.906		
	3	0.220			0.172			0.4776			0.392			1.075			0.681		
	4	/			0.162			/			0.404			/			0.661		
Benzyl	0	0.343	0.291	nc	0.277	0.216	0.511	0.498	0.421	nc	0.434	0.367	0.549	1.188	1.073	nc	1.004	0.802	0.713
	1	0.292	0.223	0.506	0.245	nc	nc	0.493	0.400	0.571	0.414	nc	nc	1.184	1.051	0.900	0.886	nc	nc
	2	0.257	0.174	/	0.205	nc	/	0.470	0.384	/	0.394	nc	/	1.084	0.974	/	0.808	nc	/
	3	0.229	/	/	0.178	nc	/	0.438	/	/	0.386	nc	/	0.939	/	/	0.708	nc	/
	4	/	/	/	0.167	/	/	/	/	/	0.408	/	/	/	/	/	0.641	/	/

Table 29A: All of the the silica based BSRs with the values of the partial charges on the metal centre. The highlighted values show where the partial charge is rising as function of the number of H$_2$ units bound.

/ = structure did not optimise

Shaded squares = no calculation was submitted on this structure

nc = value not computationally accessible

| | | Gaussian Mulliken | | | | | |
| | | BSR with 1 ligand | | | BSR with 2 ligands | | |
Ancillary ligand	No. H_2 bound	Ti^{3+}	V^{3+}	Cr^{3+}	Ti^{3+}	V^{3+}	Cr^{3+}
Benzyl	0	0.405	0.486	0.148	1.424	1.089	0.709
	1	0.225	-0.027	-0.039	0.824	0.545	-0.039
	2	-0.120	-0.055	/	0.599	0.116	/
	3	-0.449	/	/	-0.296	-0.558	/
	4	/	/	/	-0.690	/	/
Hydride	0	0.456	0.313	0.333	0.401	0.352	
	1	0.337	0.239	0.128	0.148	0.153	
	2	0.123	-0.319	-0.102	-0.128	-0.162	/
	3	/	-0.355	-0.513	-0.414	/	/
	4	/	/	/	-0.450	/	/
Methyl	0	0.566	0.501	0.478	0.655	0.632	0.750
	1	0.385	0.302	0.287	0.607	0.639	-0.348
	2	-0.180	-0.208	0.008	0.211	0.427	0.614
	3	/	/	-0.481	0.151	0.133	-0.202
	4	/	/	/	-0.182	/	/
Allyl	0	0.385			-0.096		
	1	0.210			0.651		
	2	0.104			-0.049		
	3	-0.099			-0.536		
	4	/			-0.571		

Table 30A: All of the silica based BSRs with the values of the Gaussian Mulliken partial charge on the metal centre. The highlighted values show where the partial charge is rising as function of the number of H_2 units bound.

/ = structure did not optimise.

Shaded squares = no calculation submitted on this structure.

Ligand	No. of H₂ bound	ADF Voronoi			ADF Hirshfeld			ADF Mulliken			Gaussian Mulliken			Bader		
		Ti³⁺	V³⁺	Cr³⁺	Ti³⁺	V³⁺	Cr³⁺	Ti³⁺	V³⁺	Cr³⁺	Ti³⁺	V³⁺	Cr³⁺	Ti³⁺	V³⁺	Cr³⁺
THF	**0**	0.194	0.122	0.438	0.307	0.236	0.460	1.318	1.123	0.967	1.161	0.665	0.121	1.712	1.560	nc
	1	0.177	0.120	0.442	0.325	0.260	0.480	1.299	0.020	1.036	0.920	0.416	-0.096	1.737	1.603	1.497
	2	0.168	0.075	0.445	0.359	0.255	0.513	1.200	1.009	1.002	0.469	0.092	-0.229	1.746	1.545	1.495
Hydrazine based	**0**	0.204	0.132	0.451	0.365	0.245	0.466	1.257	1.016	0.984	0.742	0.715	0.230	1.663	1.481	1.383
	1	0.170	0.128	0.416	0.334	0.271	0.461	1.215	1.148	0.939	0.463	0.364	-0.235	1.691	1.583	1.441
	2	0.144	0.079	0.406	0.318	0.244	0.468	1.083	0.975	0.468	0.127	-0.388	-0.772	1.689	1.152	1.424
1,3-dimethylallyl	**0**	0.182	0.136	0.442	0.304	0.260	0.474	1.113	1.006	0.871	0.719	0.377	0.264	1.648	/	1.313
	1	0.157	0.100	0.413	0.317	0.262	0.471	1.020	1.044	0.849	0.324	0.254	-0.072	1.640	1.484	1.352
	2	0.158	0.136	/	0.329	0.351	/	0.961	1.349	/	0.103	-0.483	/	1.645	1.503	/
(trimethylsilyl)methyl	**0**	0.208	0.147	nc	0.357	0.288	nc	1.216	1.071	nc	0.628	0.102	0.203	1.653	1.536	1.347
	1	0.183	0.127	0.409	0.364	0.280	0.460	1.184	1.082	0.966	0.097	-0.017	0.096	1.671	1.529	1.384
	2	0.138	0.092	0.403	0.327	0.273	0.478	1.089	0.958	0.894	-0.018	-0.275	-0.450	/	1.536	1.363
Hydride	**0**	0.240	0.144	0.466	0.342	0.206	0.401	1.189	1.073	0.837	0.762	0.677	0.551	1.641	1.493	1.288
	1	0.186	0.122	0.447	0.305	0.225	0.4341	1.139	1.031	0.908	0.549	0.352	0.077	1.644	1.493	1.36
	2	0.141	0.102	0.413	0.290	0.222	0.421	1.070	0.976	0.8401	0.240	-0.242	-0.785	1.620	1.490	1.258
2 hydrides	**0**	0.262	0.199	0.501	0.362	0.266	0.4089	1.085	0.963	0.802	0.572	0.467	0.316	1.595	1.437	1.231
	1	0.190	0.144	0.458	0.262	0.232	0.3909	1.043	0.940	0.813	0.374	0.227	0.220	1.595	1.434	1.265
	2	0.149	0.094	0.426	0.212	0.177	0.3954	0.932	0.901	0.779	-0.054	0.007	-0.170	1.542	1.392	1.274
	3	0.152	0.073	/	0.254	0.173	/	0.890	0.743	/	-0.114	-0.448	/	1.557	1.340	/
	4	0.200	/		0.185	/		0.859	/		-1.582	/		1.342		

Table 31A: All of the four coordinate M(III) hydrazine linked BSRs with the values of the partial charges on the metal centre. The highlighted values show where the partial charge is rising as a function of the number of H₂ units bound.

/ = structure did not optimise.

Shaded squares = no calculation was submitted on this structure

nc = value not computationally accessible

Ligand	No. of H_2 bound	ADF Voronoi			ADF Hirshfeld			ADF Mulliken			Gaussian Mulliken			Bader		
		Ti^{2+}	V^{2+}	Cr^{2+}	Ti^{2+}	V^{2+}	Cr^{2+}	Ti^{2+}	V^{2+}	Cr^{2+}	Ti^{2+}	V^{2+}	Cr^{2+}	Ti^{2+}	V^{2+}	Cr^{2+}
(trimethylsilyl)methyl	0	0.116	0.046	0.352	0.272	0.178	0.404	0.845	0.679	0.668	0.533	0.812	0.704	1.294	1.192	1.151
	1	0.096	0.004	0.319	0.255	0.174	0.400	0.818	0.675	0.598	0.481	0.298	-0.202	-1.234	1.257	1.137
	2	0.051	-0.023	/	0.238	0.169	/	0.817	0.877	/	-0.093	-0.226	/	1.484	1.307	/
	3	0.129	/		0.190	/		0.752	/		1.111	/		1.324	/	
Hydride	0	0.101	0.091	0.351	0.200	0.165	0.317	0.820	0.748	0.658	0.478	0.365	0.387	1.312	1.186	1.099
	1	0.061	0.020	0.327	0.148	0.115	0.338	0.757	0.668	0.616	0.227	0.163	-0.046	1.339	1.223	1.102
	2	0.032	-0.029	/	0.192	0.131	/	0.850	0.757	/	-0.252	-0.177	/	1.429	1.258	
	3	0.041	/		0.206	/		0.731	/		-0.274	/		1.429	/	
2 hydrides	0	0.070	0.060	0.370	0.133	0.115	0.294	0.646	0.605	0.572	0.159	0.117	0.124	1.206	1.074	1.027
	1	0.085	0.089	0.345	0.161	0.138	0.282	0.748	0.679	0.559	0.086	-0.138	0.013	nc	1.205	1.032
	2	0.049	-0.006	/	0.134	0.071	/	0.627	0.623	/	-0.368	-0.455	/	1.331	1.198	/
	3	0.031	/		0.147	/		0.621	/		-0.729	/		1.321	/	
Hydrazine based	0	0.085	0.024	0.332	0.196	0.139	0.384	0.783	0.704	0.689	0.731	0.646	0.444	1.279	1.213	1.140
	1	0.090	0.011	0.324	0.224	0.176	0.391	0.892	0.833	0.663	0.892	0.181	-0.329	1.475	1.297	1.173
	2	0.054	-0.025	/	0.238	0.184	/	0.910	0.871	/	-0.090	-0.365	/	1.509	1.352	/
THF	0	/	0.035		/	0.163		/	0.764		0.746	0.652		1.396	1.261	
	1	0.074	0.041		0.213	0.173		0.933	0.831		0.933	0.120		1.458	1.313	
	2	0.067	-0.01		0.245	0.186		0.935	0.868		0.081	-0.365		1.540	1.369	

Table 32A: All of the four coordinate M(II) hydrazine linked BSRs with the values of the partial charges on the metal centre. The highlighted values show where the partial charge is rising as function of the number of H_2 units bound.

/ = structure did not optimise

Shaded squares = no calculation was submitted on this structure

nc = value not computationally accessible

No. of H₂ bound	ADF Voronoi				ADF Hirshfeld				ADF Mulliken				Gaussian Mulliken			
	Ti^{2+}	V^{2+}	Cr^{2+}	$Ti^{2+}H$	Ti^{2+}	V^{2+}	Cr^{2+}	$Ti^{2+}H$	Ti^{2+}	V^{2+}	Cr^{2+}	$Ti^{2+}H$	Ti^{2+}	V^{2+}	Cr^{2+}	$Ti^{2+}H$
0 & 0	0.093 0.089	0.021 0.048	0.354 0.366	0.015 0.125	0.262 0.187	0.142 0.155	0.419 0.407	0.106 0.200	0.805 0.746	0.712 0.792	0.750 0.715	0.459 0.905	0.219 0.686	0.248 0.493	0.286 0.380	0.116 0.170
1 & 0	0.092 0.051	0.012 **0.054**	0.344 0.333	**0.031** 0.125	0.244 0.183	0.140 **0.185**	0.387 0.401	**0.125** 0.214	0.223 0.734	**0.723** 0.765	**0.798** **0.771**	**0.492** 0.961	**1.035** **0.756**	0.399 0.479	0.188 **0.625**	-0.227 0.073
1 & 1	0.067 **0.071**	-0.012 -0.017	**0.355** **0.341**	0.022 0.106	**0.247** **0.227**	0.174 0.149	**0.429** **0.417**	0.104 0.184	**0.852** **0.875**	0.753 **0.821**	0.780 0.745	0.502 0.938	-0.182 0.513	0.020 0.124	-0.341 0.523	**-0.168** 0.140
1 & 2	0.054 0.069	-0.025 -0.021	/	**0.031** 0.093	**0.251** 0.226	**0.191** **0.150**	/	0.118 **0.219**	**0.895** 0.867	**0.907** **0.892**	/	**0.520** 0.857	**-0.399** 0.454	-0.348 0.048	/	-0.339 0.001
2 & 2	0.036 0.052	-0.025 **-0.015**	/	**0.035** 0.069	0.229 **0.241**	**0.193** **0.186**	/	**0.159** 0.218	0.729 0.864	0.805 0.848	/	**0.672** 0.754	**-0.219** 0.068	-0.503 **0.113**	/	**-0.398** **0.059**

Table 33A: M(II) lowest energy dimers with the values of the partial charges on both of the metal centres. The highlighted values are for the metal centres binding more H₂ units in that case. The values in bold shown where the partial charge is rising as a function of the number of H₂ units bound.

/=structure did not optimise

Ti²⁺H=dimer with hydride ancillary ligands.

| No. of H$_2$ bound | Bader | | | | | ADF Voronoi | ADF Hirshfeld | ADF Mulliken | Gaussian Mulliken |
	Ti^{2+}	V^{2+}	Cr^{2+}	Mn^{2+}	Ti^{2+}H	Mn^{2+}	Mn^{2+}	Mn^{2+}	Mn^{2+}
0 & 0	nc	1.163	1.150	1.224	nc	0.157	0.279	0.846	0.114
		1.269	1.195	1.238		0.138	0.247	0.847	0.104
1 & 0	nc	**1.177**	**1.179**	**1.289**	nc	**0.182**	0.176	**0.955**	-0.472
		1.312	**1.220**	**1.260**		**0.143**	**0.250**	**0.870**	**0.359**
1 & 1	1.397	**1.283**	**1.233**	/	1.198	/	/	/	/
	1.502	**1.340**	**1.229**		1.447				
1 & 2	nc	**1.340**	/	/	**1.231**	/	/	/	/
		1.346			**1.454**				
2 & 2	nc	1.332	/	/	**1.396**	/	/	/	/
		1.366			1.443				

Table 34A: All of the M(II) lowest energy dimers with the values of the Bader partial charges on both of the metal centres and the partial charge values of the Mn(II) lowest energy dimer. The highlighted values are for the metal centres binding more H$_2$ units in that case. The values in bold show where the partial charge is rising as a function of the number of H$_2$ units bound.

/=structure did not optimise

Ti^{2+}H=dimer with hydride ancillary ligands.

nc = value not computationally accessible

No. of H$_2$ bound	ADF Voronoi				ADF Hirshfeld				ADF Mulliken				Gaussian Mulliken			
	Ti^{3+}	V^{3+}	Cr^{3+}	Ti^{3+}H	Ti^{3+}	V^{3+}	Cr^{3+}	Ti^{3+}H	Ti^{3+}	V^{3+}	Cr^{3+}	Ti^{3+}H	Ti^{3+}	V^{3+}	Cr^{3+}	Ti^{3+}H
0 & 0	0.208	0.134	0.434	0.196	0.307	0.245	0.437	0.251	1.254	1.029	0.957	1.106	1.000	0.902	0.612	0.443
	0.187	0.135	0.442	0.211	0.294	0.233	0.457	0.254	1.152	1.099	1.048	1.153	1.030	0.260	0.797	1.010
1 & 0	0.189	**0.140**	**0.438**	**0.224**	**0.318**	**0.275**	**0.475**	**0.293**	1.178	**1.066**	0.898	**1.115**	0.521	0.510	0.269	**0.704**
	0.198	0.120	0.432	0.182	**0.304**	0.230	0.453	**0.288**	**1.249**	**1.113**	1.017	**1.113**	0.963	**0.714**	0.600	0.439
1 & 1	**0.203**	**0.149**	0.434	0.208	**0.351**	**0.282**	**0.477**	**0.313**	**1.217**	**1.108**	**0.926**	**1.127**	**0.689**	0.424	**0.926**	0.359
	0.146	**0.129**	0.432	**0.191**	0.280	**0.268**	**0.472**	**0.295**	1.056	1.107	0.981	**1.125**	0.588	**0.845**	**0.981**	**0.528**
1 & 2	0.159	0.100	/	0.182	0.324	0.273	/	0.271	1.059	1.037	/	1.114	0.244	0.205	/	**0.592**
	0.210	0.127		0.155	**0.351**	0.268		0.266	**1.256**	**1.146**		0.915	**0.709**	0.513		0.027
2 & 2	**0.165**	/	/	0.151	**0.331**	/	/	0.253	**1.134**	/	/	0.978	0.145	/	/	-0.104
	0.184			0.152	0.343			0.264	1.183			**0.944**	0.437			**0.059**

Table 35A: All of the M(III) lowest energy dimers with the values of the partial charges on both of the metal centres. The highlighted values are for the metal centres binding more H$_2$ units in that case. The values in bold show where the partial charge is rising as a function of the number of H$_2$ units bound.

/=structure did not optimise

Ti^{3+}H=dimer with hydride ancillary ligands.

No. of H_2 bound	Bader			
	Ti^{3+}	V^{3+}	Cr^{3+}	$Ti^{3+}H$
0 & 0	nc	nc	1.440 1.481	1.576 1.614
1 & 0	nc	1.525 1.558	1.413 1.466	**1.612** 1.576
1 & 1	1.708 1.626	1.548 **1.593**	1.407 **1.480**	nc
1 & 2	1.676 **1.713**	nc	/	**1.653** **1.598**
2 & 2	nc	/	/	1.619 **1.604**

Table 36A: All of the M(III) lowest energy dimers with the values of the Bader partial charges on both of the metal centres. The highlighted values are for the metal centres binding more H_2 units in that case. The values in bold show where the partial charge is rising as a function of the number of H_2 units bound.

/=structure did not optimise

$Ti^{3+}H$=dimer with hydride ancillary ligands

nc = value not computationally accessible

	ADF Voronoi			ADF Hirshfeld			ADF Mulliken			Gaussian Mulliken			Bader		
No. of H_2 bound	0	1	2	0	1	2	0	1	2	0	1	2	0	1	2
Cu(I)	0.117	0.243	0.232	0.146	0.243	0.286	0.264	0.379	0.284	-0.203	-0.028	-0.178	0.442	nc	0.581
Cu(II)	0.199	0.373	0.355	0.211	0.254	0.270	0.351	0.470	0.371	-0.216	-0.373	-0.653	0.591	0.733	0.675
Ni(II)	0.115	0.216	0.250	0.123	0.221	0.244	0.179	0.268	0.348	0.043	-0.007	-0.100	0.474	0.593	0.626

Table 37A: All of the two coordinate late transition metal BSRs with the values of the partial charges on the metal centre. The highlighted values show where the partial charge is rising as function of the number of H_2 units bound.

/=structure did not optimise.

nc = value not computationally accessible

No. of H_2 bound	Mulliken		Hirshfeld		Voronoi		Gaussian Mulliken		Bader	
	Ti 1	Ti 2	Ti 1	Ti 2	Ti 1	Ti 2	Ti 1	Ti 2	Ti 1	Ti 2
0	0.805	0.746	0.262	0.187	0.093	0.089	0.219	0.686	error	error
1	**1.035**	**0.756**	0.244	0.183	0.092	0.051	**0.223**	**0.734**	error	error
2	0.852	**0.875**	**0.247**	**0.227**	0.067	**0.071**	-0.182	0.513	1.397	1.502
3	**0.895**	0.867	**0.251**	0.226	0.054	0.069	-0.399	0.454	error	error
4	0.729	0.864	0.229	0.241	0.036	0.052	**-0.219**	0.068	error	error

Table 38A: Ti(II) D2 with the values of the partial charges on both of the metal centres. The highlighted values are for the metal centres binding more H_2 units in that case. The values in bold show where the partial charge is rising as a function of the number of H_2 units bound.

No. of H_2 bound	Mulliken		Hirshfeld		Voronoi		Gaussian Mulliken		Bader	
	Ti 1	Ti 2	Ti 1	Ti 2	Ti 1	Ti 2	Ti 1	Ti 2	Ti 1	Ti 2
0	1.022	0.690	0.246	0.134	0.146	0.034	0.810	0.644	1.495	1.238
1	0.970	**0.843**	**0.253**	**0.192**	**0.149**	**0.058**	**0.853**	0.162	1.493	**1.384**
2	nc	nc	nc	nc	nc	nc	0.566	0.160	1.475	1.370
3	0.969	**0.961**	0.250	**0.259**	0.084	0.079	0.361	-0.041	**1.556**	**1.440**
4	0.855	0.831	0.221	0.243	0.060	0.044	-0.148	**0.147**	1.491	**1.462**

Table 39A: Ti(II) D7 with the values of the partial charges on both of the metal centres. The highlighted values are for the metal centres binding more H_2 units in that case. The values in bold show where the partial charge is rising as a function of the number of H_2 units bound.

nc = value not computationally accessible.

No. of H₂ bound	Mulliken		Hirshfeld		Voronoi		Gaussian Mulliken		Bader	
	V 1	**V 2**	**V 1**	**V 2**	**V 1**	**V 2**	**V 1**	**V 2**	**V 1**	**V 2**
0	0.712	0.792	0.142	0.155	0.021	0.048	0.248	0.493	1.163	1.269
1	**0.723**	0.765	0.140	**0.185**	0.012	**0.054**	**0.399**	0.479	**1.177**	**1.312**
2	**0.753**	**0.821**	**0.174**	0.149	-0.012	-0.017	0.020	0.124	**1.283**	**1.340**
3	**0.907**	**0.892**	**0.191**	**0.150**	-0.025	-0.021	-0.348	0.048	**1.340**	**1.346**
4	0.805	0.848	**0.193**	**0.186**	-0.025	**-0.015**	-0.503	**0.113**	1.332	**1.366**

Table 40A: V(II) D2 with the values of the partial charges on both of the metal centres. The highlighted values are for the metal centres binding more H₂ units in that case. The values in bold show where the partial charge is rising as a function of the number of H₂ units bound.

No. of H₂ bound	Mulliken		Hirshfeld		Voronoi		Gaussian Mulliken		Bader	
	V 1	**V 2**	**V 1**	**V 2**	**V 1**	**V 2**	**V 1**	**V 2**	**V 1**	**V 2**
0	0.531	1.098	0.064	0.232	-0.059	0.126	0.136	0.549	0.991	1.507
1	-0.145	0.734	**0.121**	0.211	**-0.041**	0.097	**0.748**	**0.991**	**1.177**	1.434
2	**0.713**	**0.959**	**0.124**	**0.222**	-0.053	0.079	0.682	0.315	1.174	1.428
3	**0.754**	0.919	**0.147**	0.203	**-0.043**	0.044	**0.754**	**0.919**	error	error
4	**0.892**	0.823	**0.186**	0.176	**-0.020**	0.006	0.020	-0.094	error	error

Table 41A: V(II) D5 with the values of the partial charges on both of the metal centres. The highlighted values are for the metal centres binding more H₂ units in that case. The values in bold show where the partial charge is rising as a function of the number of H₂ units bound.
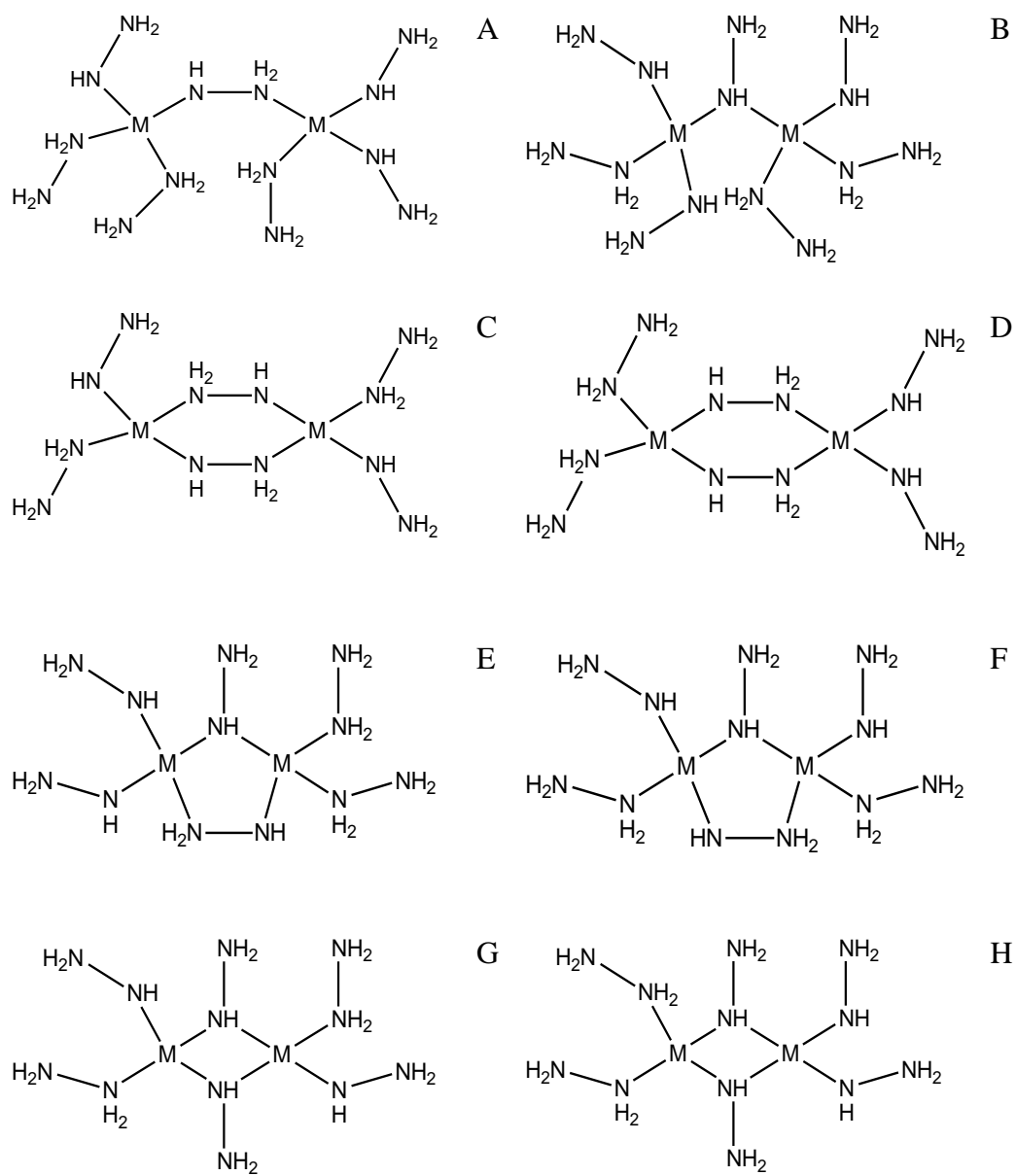
Figure 65A: Schematic representations of, A – H, dimers 1 – 8 where M= Ti^{2+}, V^{2+}, Cr^{2+} or Mn^{2+}.
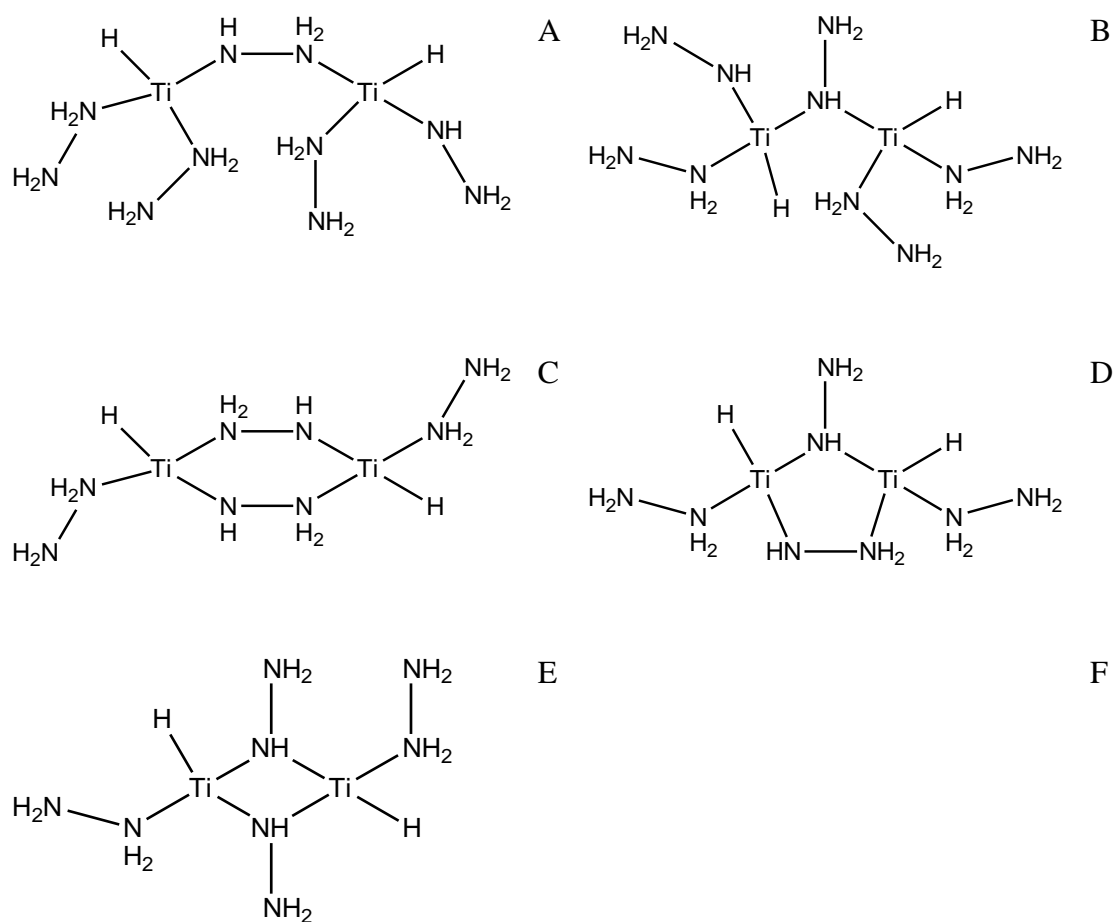
Figure 66A: Schematic representations of, A − E, dimers one, two, three, six and seven with Ti^{2+} and hydride ancillary ligands.
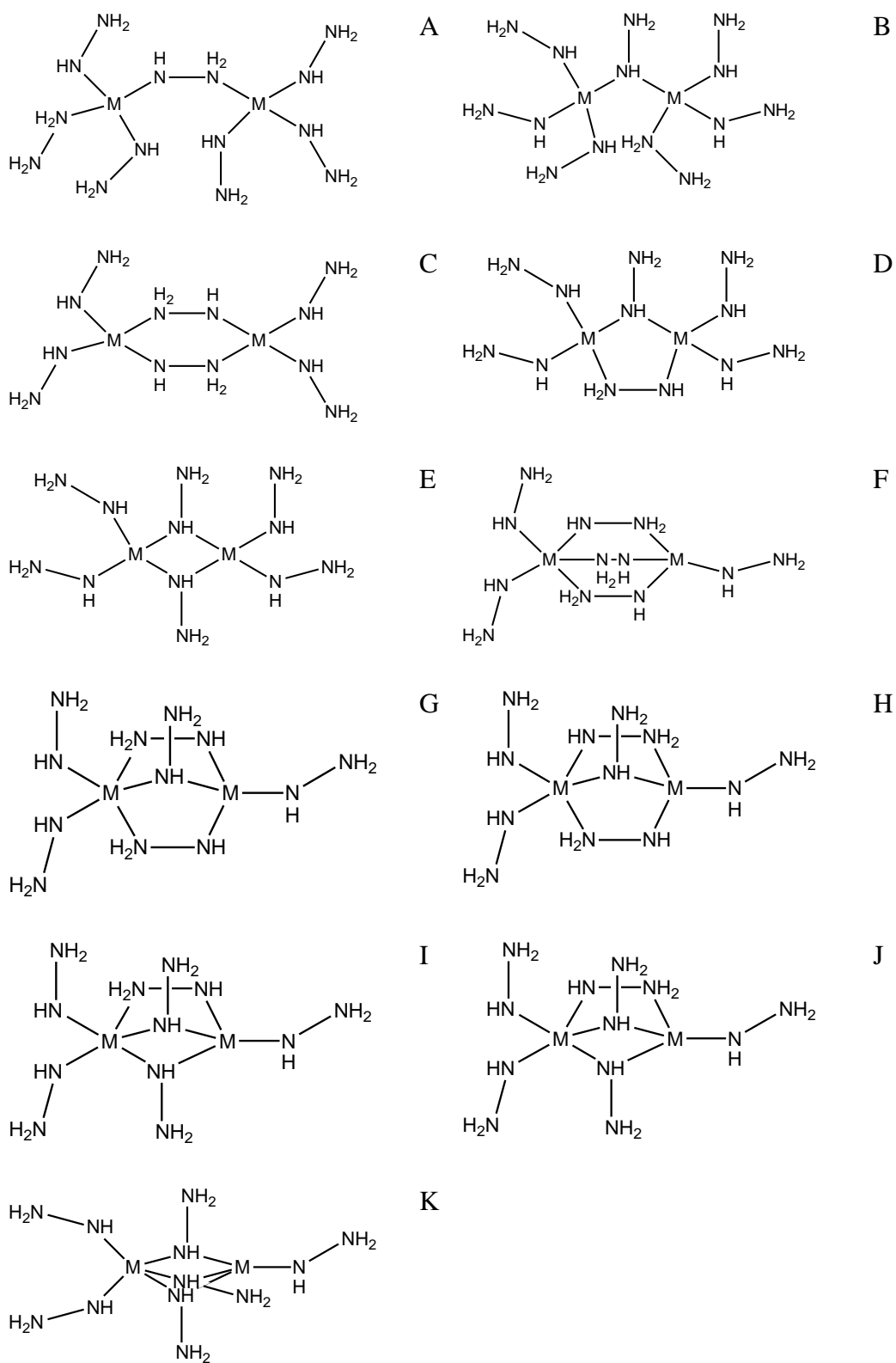
Figure 67A: Schematic representations of, A − K, dimers one, two, three, six, seven, 9, 10,11, 12, 13 and 14 where M= Ti^{3+}, V^{3+} or Cr^{3+}.
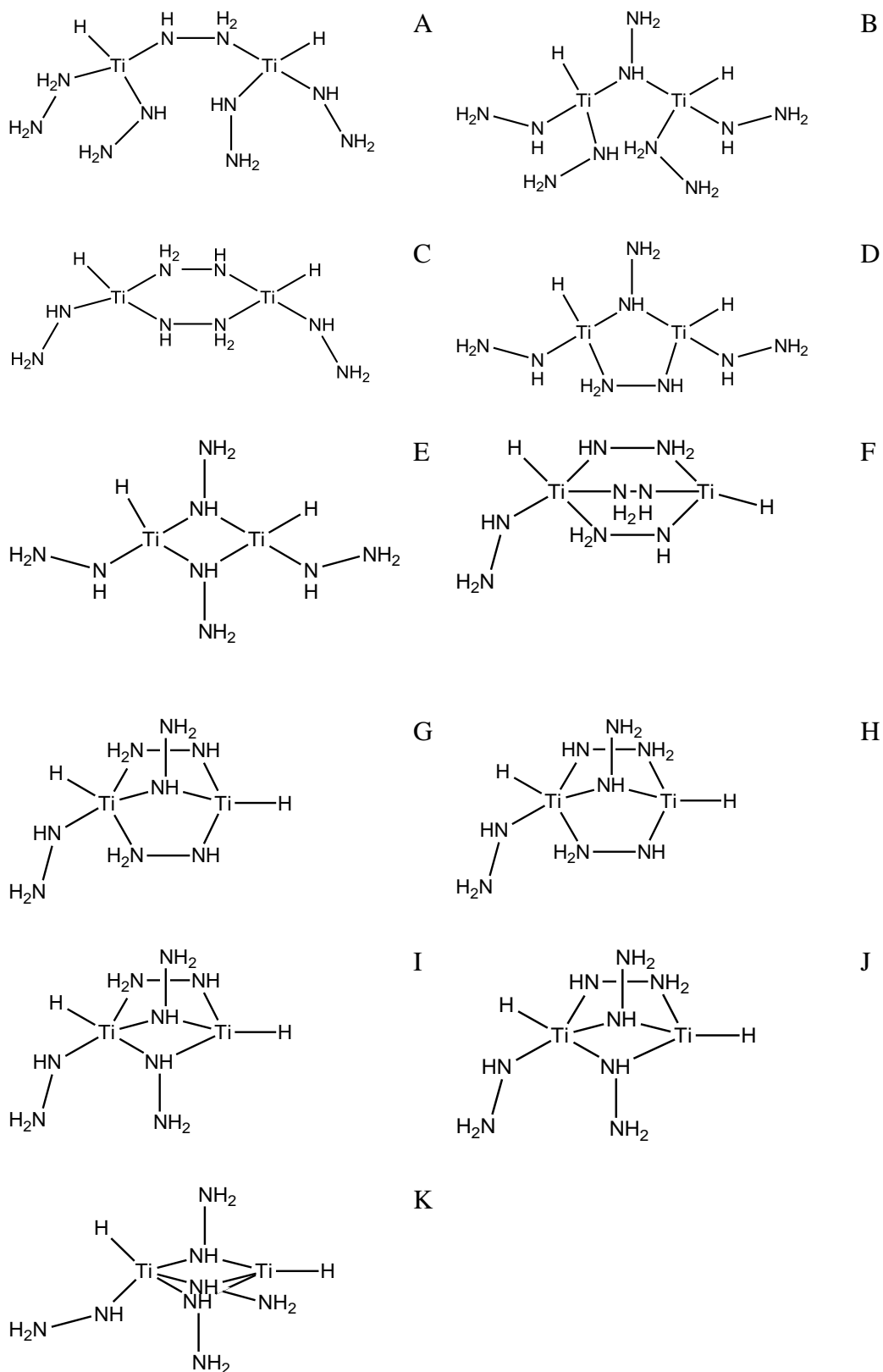
Figure 68A: Schematic representations of, A – K, dimers one, two , three, six, seven, 9, 10,11, 12, 13 and 14 with Ti^{3+} and hydride ancillary ligands.

References

1.   L. Schlapbach and A. Zuttel, *Nature*, 2001, **414**, 353.
2.   J. Rifkin, *The Third Industrial Revolution*, Palgrave Macmillan, 2011.
3.   G. Krajačić, R. Martins, A. Busuttil, N. Duić, M. da Graça Carvalho,.
4.   panorama, *Int. J. Hydrogen Energ.*, 2008, **33**, 1091.
5.   P. V. Kamat, *J. Phys. Chem. C*, 2007, **111**, 2834.
6.   N. Myers and J. Kent, *Proc. Natl. Acad. Sc. U.S.A.*, 2003, **100**, 4963.
7.   *China's motor vehicles top 233 mln*, English.news.cn, Editor:An, 17/07/2012.
8.   T. T. Conway, P. NOAA/ESRL, Trends in Atmospheric Carbon Dioxide, www.esrl.noaa.gov/gmd/ccgg/trends/, Accessed 15/06/2012.
9.   P. N. Pearson and M. R. Palmer, *Nature*, 2000, **406**, 695.
10.   Met Office, Met Office 2012 annual global temperature forecast, http://www.metoffice.gov.uk/news/releases/archive/2011/2012-global-temperature-forecast, Accessed 15/06/2012.
11.   M. E. Mann, R. S. Bradley and M. K. Hughes, *Nature*, 1998, **392**, 779.
12.   U.S. Department of Energy, Financial Incentives for Hydrogen and Fuel Cell   Projects, http://www1.eere.energy.gov/hydrogenandfuelcells/incentives.html, Accessed 15/06/2012.
13.   Fuel Cells 2000, Fuel Cell-Powered Forklifts in North America, http://www.fuelcells.org/wp-content/uploads/2012/02/forklifts.pdf, Accessed 15/06/2012.
14.   G. Schubak, 19th World Hydrogen Energy Conference, Toronto, Canada, 2012.
15.   S. Satyapal, 19th World Hydrogen Energy Conference, Toronto, Canada, 2012.
16.   I. Mansouri, 19th World Hydrogen Energy Conference, Toronto, Canada, 2012.
17.   B. Forget, 19th World Hydrogen Energy Conference, Toronto, Canada, 2012.
18.   J. Emsley, *Nature's Building Blocks: An A-Z Guide to the Elements*, Oxford University Press, 2nd Edition, 2011.
19.   T. Ito, 19th World Hydrogen Energy Conference, Toronto, Canada, 2012.
20.   K. L. Lim, H. Kazemian, Z. Yaakob, W. Ramli and W. Daud, 2010, **33**, 213.
21.   K. Hirose, 19th World Hydrogen Energy Conference, Toronoto, Canada, 2012.
22.   M. Kampitsch, 19th World Hydrogen Energy Conference, Toronto, Canada, 2012.
23.   Hydrogen, Fuel Cells and Infrastructure Technologies Program: Multi-Year Research, Development and Demonstration Plan: Planned Program Activities for 2005-2015. Section 3.3 Hydrogen Storage, 2007, http://www1.eere.energy.gov/hydrogenandfuelcells/mypp/pdfs/storage.pdf, Accessed 16/03, 2010.
24.   R. C. Lochan and M. Head-Gordon, *Phys. Chem. Chem. Phys.*, 2006, **8**, 1357.
25.   J. L. C. Rowsell and O. M. Yaghi, *Angew. Chem.-Int. Edit.*, 2005, **44**, 4670.
26.   A. W. C. van den Berg and C. O. Arean, *Chem. Commun.*, 2008, 668.

27.	O. K. Farha, A. O. Yazaydin, I. Eryazici, C. D. Malliakas, B. G. Hauser, M. G. Kanatzidis, S. T. Nguyen, R. Q. Snurr and J. T. Hupp, *Nat. Chem.*, 2010, **2**, 944.

28.	M. Dinca and J. R. Long, *Angew. Chem.-Int. Edit.*, 2008, **47**, 6766.

29.	T. K. A. Hoang and D. M. Antonelli, *Adv. Mater.*, 2009, **21**, 1787.

30.	S. I. Orimo, Y. Nakamori, J. R. Eliseo, A. Zuttel and C. M. Jensen, *Chem. Rev.*, 2007, **107**, 4111.

31.	J. Graetz and J. J. Reilly, *Scr. Mater.*, 2007, **56**, 835.

32.	L. F. Wang and R. T. Yang, *Energy Environ. Sci.*, 2008, **1**, 268.

33.	G. J. Kubas, *J. Organomet. Chem.*, 2001, **635**, 37.

34.	G. J. Kubas, *J. Organomet. Chem.*, 2009, **694**, 2648.

35.	J. S. Dewar, *Bull. Soc. Chim. Fr.*, 1951, **18**, C71.

36.	J. Chatt and L. A. Duncanson, *J. Chem. Soc.*, 1953, 2939.

37.	G. J. Kubas, R. R. Ryan, P. J. Vergamini and H. Wasserman, *Abstr. Pap. Am. Chem. Soc.*, 1983, **185**, 229.

38.	G. J. Kubas, R. R. Ryan, B. I. Swanson, P. J. Vergamini and H. J. Wasserman, *J. Am. Chem. Soc.*, 1984, **106**, 451.

39.	G. J. Kubas, *Chem. Rev.*, 2007, **107**, 4152.

40.	M. Dinca, A. Dailly, Y. Liu, C. M. Brown, D. A. Neumann and J. R. Long, *J. Am. Chem. Soc.*, 2006, **128**, 16876.

41.	J. G. Vitillo, L. Regli, S. Chavan, G. Ricchiardi, G. Spoto, P. D. C. Dietzel, S. Bordiga and A. Zecchina, *J. Am. Chem. Soc.*, 2008, **130**, 8386.

42.	J. S. Shi, J. Li and E. D. Wu, *Microporous Mesoporous Mat.*, 2012, **152**, 219.

43.	S. S. Kaye and J. R. Long, *J. Am. Chem. Soc.*, 2008, **130**, 806.

44.	A. B. Phillips, B. S. Shivaram and G. R. Myneni, *Int. J. Hydrog. Energy*, 2012, **37**, 1546.

45.	X. Solans-Monfort, M. Sodupe and J. Eckert, *J. Phys. Chem. C*, 2010, **114**, 13926.

46.	W. Zhou and T. Yildirim, *J. Phys. Chem. C*, 2008, **112**, 8132.

47.	Y. Y. Sun, Y. H. Kim and S. B. Zhang, *J. Am. Chem. Soc.*, 2007, **129**, 12606.

48.	W. Silva, T. N. Truong and F. Mondragon, *J. Alloy. Compd.*, 2011, **509**, 8501.

49.	M. I. Rojas and E. P. M. Leiva, *Phys. Rev. B*, 2007, **76**, 155415.

50.	G. Kim and S. H. Jhi, *J. Phys. Chem. C*, 2009, **113**, 20499.

51.	G. Kim, S. H. Jhi, S. Lim and N. Park, *Phys. Rev. B*, 2009, **79**, 155437.

52.	T. Yildirim and S. Ciraci, *Phys. Rev. Lett.*, 2005, **94**, 175501.

53.	S. A. Shevlin and Z. X. Guo, *J. Phys. Chem. C*, 2008, **112**, 17456.

54.	X. L. Zou, G. Zhou, W. H. Duan, K. Choi and J. Ihm, *J. Phys. Chem. C*, 2010, **114**, 13402.

55.	G. F. Wu, J. L. Wang, X. Y. Zhang and L. Y. Zhu, *J. Phys. Chem. C*, 2009, **113**, 7052.

56.	Y. F. Zhao, Y. H. Kim, A. C. Dillon, M. J. Heben and S. B. Zhang, *Phys. Rev. Lett.*, 2005, **94**, 155504.

57.	Q. Sun, Q. Wang, P. Jena and Y. Kawazoe, *J. Am. Chem. Soc.*, 2005, **127**, 14582.

58.	E. Durgun, S. Ciraci, W. Zhou and T. Yildirim, *Phys. Rev. Lett.*, 2006, **97**, 226102.

59. W. Zhou, T. Yildirim, E. Durgun and S. Ciraci, *Phys. Rev. B*, 2007, **76**, 085434.
60. N. He, T. Gao, Z. H. Zhang, X. F. Tian and H. L. Han, *Theochem-J. Mol. Struct.*, 2009, **916**, 147.
61. H. Lee, W. I. Choi and J. Ihm, *Phys. Rev. Lett.*, 2006, **97**, 056104.
62. M. C. Nguyen, H. Lee and J. Ihm, *Solid State Commun.*, 2008, **147**, 419.
63. H. Y. Zhu, Y. Z. Chen, S. Li, X. D. Yang and Y. N. Liu, *Int. J. Hydrog. Energy*, 2011, **36**, 11810.
64. C. G. Zhang, R. W. Zhang, Z. X. Wang, Z. Zhou, S. B. Zhang and Z. F. Chen, *Chem.-Eur. J.*, 2009, **15**, 5910.
65. M. Kosa, M. Krack, A. K. Cheetham and M. Parrinello, *J. Phys. Chem. C*, 2008, **112**, 16171.
66. L. Wang, K. Lee, Y. Y. Sun, M. Lucking, Z. F. Chen, J. J. Zhao and S. B. B. Zhang, *ACS Nano*, 2009, **3**, 2995.
67. A. B. Phillips and B. S. Shivaram, *Phys. Rev. Lett.*, 2008, **100**, 105505.
68. P. F. Weck, T. J. D. Kumar, E. Kim and N. Balakrishnan, *J. Chem. Phys.*, 2007, **126**, 094703.
69. A. Mavrandonakis, E. Klontzas, E. Tylianakis and G. E. Froudakis, *J. Am. Chem. Soc.*, 2009, **131**, 13410.
70. R. C. Lochan, R. Z. Khaliullin and M. Head-Gordon, *Inorg. Chem.*, 2008, **47**, 4032.
71. Y. Y. Sun, K. Lee, L. Wang, Y. H. Kim, W. Chen, Z. F. Chen and S. B. Zhang, *Phys. Rev. B*, 2010, **82**, 073401.
72. H. Lee, M. C. Nguyen and J. Ihm, *Solid State Commun.*, 2008, **146**, 431.
73. A. Hamaed, M. Trudeau and D. M. Antonelli, *J. Am. Chem. Soc.*, 2008, **130**, 6992.
74. A. Hamaed, H. Van Mai, T. K. A. Hoang, M. Trudeau and D. Antonelli, *J. Phys. Chem. C*, 2010, **114**, 8651.
75. A. Hamaed, T. K. A. Hoang, M. Trudeau and D. M. Antonelli, *J. Organomet. Chem.*, 2009, **694**, 2793.
76. T. K. A. Hoang, A. Hamaed, M. Trudeau and D. M. Antonelli, *J. Phys. Chem. C*, 2009, **113**, 17240.
77. A. Hamaed, T. K. A. Hoang, G. Moula, R. Aroca, M. L. Trudeau and D. M. Antonelli, *J. Am. Chem. Soc.*, 2011, **133**, 15434.
78. T. K. A. Hoang, M. I. Webb, H. V. Mai, A. Hamaed, C. J. Walsby, M. Trudeau and D. M. Antonelli, *J. Am. Chem. Soc.*, 2010, **132**, 11792.
79. T. K. A. Hoang, L. Morris, J. M. Rawson, M. L. Trudeau and D. M. Antonelli, *Chemistry of Materials*, 2012, **24**, 1629.
80. T. K. A. Hoang, A. Hamaed, G. Moula, R. Aroca, M. Trudeau and D. M. Antonelli, *J. Am. Chem. Soc.*, 2011, **133**, 4955.
81. B. R. Bender, G. J. Kubas, L. H. Jones, B. I. Swanson, J. Eckert, K. B. Capps and C. D. Hoff, *J. Am. Chem. Soc.*, 1997, **119**, 9179.
82. C. V. J. Skipper, A. Hamaed, D. M. Antonelli and N. Kaltsoyannis, *J. Am. Chem. Soc.*, 2010, **132**, 17296.
83. C. V. J. Skipper, T. K. A. Hoang, D. M. Antonelli, and N. Kaltsoyannis, *Chem. Eur. J.*, 2012, **18**, 1750.
84. C. V. J. Skipper, D. M. Antonelli and N. Kaltsoyannis, *Dalton Trans.*, 2012, **41**, 8513.
85. C. V. J. Skipper, D. M. Antonelli and N. Kaltsoyannis, *J. Phys. Chem. C*, 2012, **116**, 19134.

86. C. V. J. Skipper, D. M. Antonelli and N. Kaltsoyannis, *Enrgy Proced.*, 2012, **29**, 585.

87. C. J. Cramer, *Essentials of Computational Chemistry Theories and Models*, Wiley, 2005.

88. E. Wimmer, in *Density Functional Methods in Chemistry*, ed. J. A. Labanowski, J. , Springer-Verlag, 1991, ch. 2.

89. W. Y. Robert G. Parr, *Density - Functional Theory of Atoms and Molecules*, Oxford University Press, 1989.

90. P. Hohenberg and W. Kohn, *Phys. Rev. B*, 1964, **136**, B864.

91. W. Kohn and L. J. Sham, *Physical Review*, 1965, **140**, 1133.

92. J. P. Perdew, K. Burke and M. Ernzerhof, *Phys. Rev. Lett.*, 1996, **77**, 3865.

93. J. P. Perdew, K. Burke and M. Ernzerhof, *Phys. Rev. Lett.*, 1997, **78**, 1396.

94. S. H. Vosko, L. Wilk and M. Nusair, *Can. J. Phys.*, 1980, **58**, 1200.

95. A. D. Becke, *Phys. Rev. A*, 1988, **38**, 3098.

96. C. T. Lee, W. T. Yang and R. G. Parr, *Phys. Rev. B*, 1988, **37**, 785.

97. B. G. Johnson, P. M. W. Gill and J. A. Pople, *J. Chem. Phys.*, 1993, **98**, 5612.

98. T. V. Russo, R. L. Martin and P. J. Hay, *J. Chem. Phys.*, 1994, **101**, 7729.

99. P. J. Stephens, F. J. Devlin, C. F. Chabalowski and M. J. Frisch, *J. Phys. Chem.*, 1994, **98**, 11623.

100. A. D. Becke, *J. Chem. Phys.*, 1993, **98**, 1372.

101. S. Grimme, *J. Comput. Chem.*, 2006, **27**, 1787.

102. Gaussian 09, Revision A.02, M. J. Frisch, G. W. Trucks, H. B. Schlegel, G. E. Scuseria, M. A. Robb, J. R. Cheeseman, G. Scalmani, V. Barone, B. Mennucci, G. A. Petersson, H. Nakatsuji, M. Caricato, X. Li, H. P. Hratchian, A. F. Izmaylov, J. Bloino, G. Zheng, J. L. Sonnenberg, M. Hada, M. Ehara, K. Toyota, R. Fukuda, J. Hasegawa, M. Ishida, T. Nakajima, Y. Honda, O. Kitao, H. Nakai, T. Vreven, J. A. Montgomery, Jr., J. E. Peralta, F. Ogliaro, M. Bearpark, J. J. Heyd, E. Brothers, K. N. Kudin, V. N. Staroverov, R. Kobayashi, J. Normand, K. Raghavachari, A. Rendell, J. C. Burant, S. S. Iyengar, J. Tomasi, M. Cossi, N. Rega, J. M. Millam, M. Klene, J. E. Knox, J. B. Cross, V. Bakken, C. Adamo, J. Jaramillo, R. Gomperts, R. E. Stratmann, O. Yazyev, A. J. Austin, R. Cammi, C. Pomelli, J. W. Ochterski, R. L. Martin, K. Morokuma, V. G. Zakrzewski, G. A. Voth, P. Salvador, J. J. Dannenberg, S. Dapprich, A. D. Daniels, Ö. Farkas, J. B. Foresman, J. V. Ortiz, J. Cioslowski, and D. J. Fox, Gaussian, Inc., Wallingford CT, 2009.

103. R. C. Raffenetti, *J. Chem. Phys.*, 1973, **59**, 5936.

104. D. P. Chong, *Can. J. Chem.-Rev. Can. Chim.*, 1995, **73**, 79.

105. D. P. Chong, E. Van Lenthe, S. Van Gisbergen and E. J. Baerends, *J. Comput. Chem.*, 2004, **25**, 1030.

106. G. D. Zeiss, W. R. Scott, N. Suzuki, D. P. Chong and S. R. Langhoff, *Mol. Phys.*, 1979, **37**, 1543.

107. E. Van Lenthe and E. J. Baerends, *J. Comput. Chem.*, 2003, **24**, 1142.

108. M. Guell, J. M. Luis, M. Sola and M. Swart, *J. Phys. Chem. A*, 2008, **112**, 6384.

109. T. Clark, J. Chandrasekhar, G. W. Spitznagel and P. V. Schleyer, *J. Comput. Chem.*, 1983, **4**, 294.

110. M. J. Frisch, J. A. Pople and J. S. Binkley, *J. Chem. Phys.*, 1984, **80**, 3265.
111. P. J. Hay, *J. Chem. Phys.*, 1977, **66**, 4377.
112. R. Krishnan, J. S. Binkley, R. Seeger and J. A. Pople, *J. Chem. Phys.*, 1980, **72**, 650.
113. A. D. McLean and G. S. Chandler, *J. Chem. Phys.*, 1980, **72**, 5639.
114. K. Raghavachari and G. W. Trucks, *J. Chem. Phys.*, 1989, **91**, 1062.
115. A. J. Wachters, *J. Chem. Phys.*, 1970, **52**, 1033.
116. C. F. Matta and R. J. Boyd, in *The Quantum Theory of Atoms in Molecules*, eds. C. F. Matta and R. J. Boyd, Wiley, 2007, ch. 1, pp. 1-33.
117. R. F. W. Bader, *Atoms in Molecules: A Quantum Theory*, Oxford University Press, 1990.
118. R. F. W. Bader and K. E. Laidig, *Theochem-Journal of Molecular Structure*, 1991, **80**, 75.
119. H. A. Sparkes, A. B. Chaplin, A. S. Weller and J. A. K. Howard, *Acta Crystallogr. Sect. B-Struct. Sci.*, 2010, **66**, 503.
120. L. J. Farrugia and H. M. Senn, *J. Phys. Chem. A*, 2010, **114**, 13418.
121. C. F. Guerra, J. W. Handgraaf, E. J. Baerends and F. M. Bickelhaupt, *J. Comput. Chem.*, 2004, **25**, 189.
122. R. S. Mulliken, *J. Chem. Phys.*, 1955, **23**, 1833.
123. R. S. Mulliken, *J. Chem. Phys.*, 1955, **23**, 1841.
124. R. S. Mulliken, *J. Chem. Phys.*, 1955, **23**, 2338.
125. R. S. Mulliken, *J. Chem. Phys.*, 1955, **23**, 2343.
126. F. L. Hirshfeld, *Theor. Chim. Acta*, 1977, **44**, 129.
127. F. M. Bickelhaupt, N. Hommes, C. F. Guerra and E. J. Baerends, *Organometallics*, 1996, **15**, 2923.
128. C. V. J. Skipper, Chemistry MSci, University College London, 2009.
129. J. Cha, C. H. Choi and N. Park, *Chemical Physics Letters*, 2011, **513**, 256.
130. Y. Y. Sun, Y. H. Kim, K. Lee, D. West and S. B. Zhang, *Phys. Chem. Chem. Phys.*, 2011, **13**, 5042.
131. A. K. Singh, A. Sadrzadeh and B. I. Yakobson, *J. Am. Chem. Soc.*, 2010, **132**, 14126.
132. M. Li, J. M. Li, Q. A. Sun and Y. Jia, *J. Appl. Phys.*, 2010, **108**, 064326.
133. ADF2009.01, SCM, Theoretical Chemistry, Vrije Universiteit, Amsterdam, The Netherlands, http://www.scm.com.
134. Gaussian 03, M. J. Frisch, G. W. Trucks, H. B. Schlegel, G. E. Scuseria, M. A. Robb, J. R. Cheeseman, J. A. Montgomery, Jr., T. Vreven, K. N. Kudin, J. C. Burant, J. M. Millam, S. S. Iyengar, J. Tomasi, V. Barone, B. Mennucci, M. Cossi, G. Scalmani, N. Rega, G. A. Petersson, H. Nakatsuji, M. Hada, M. Ehara, K. Toyota, R. Fukuda, J. Hasegawa, M. Ishida, T. Nakajima, Y. Honda, O. Kitao, H. Nakai, M. Klene, X. Li, J. E. Knox, H. P. Hratchian, J. B. Cross, V. Bakken, C. Adamo, J. Jaramillo, R. Gomperts, R. E. Stratmann, O. Yazyev, A. J. Austin, R. Cammi, C. Pomelli, J. W. Ochterski, P. Y. Ayala, K. Morokuma, G. A. Voth, P. Salvador, J. J. Dannenberg, V. G. Zakrzewski, S. Dapprich, A. D. Daniels, M. C. Strain, O. Farkas, D. K. Malick, A. D. Rabuck, K. Raghavachari, J. B. Foresman, J. V. Ortiz, Q. Cui, A. G. Baboul, S. Clifford, J. Cioslowski, B. B. Stefanov, G. Liu, A. Liashenko, P. Piskorz, I. Komaromi, R. L. Martin, D. J. Fox, T. Keith, M. A. Al-Laham, C. Y.

Peng, A. Nanayakkara, M. Challacombe, P. M. W. Gill, B. Johnson, W. Chen, M. W. Wong, C. Gonzalez, and J. A. Pople, Gaussian, Inc., Wallingford CT, 2004.

135. AIMALL Revision 11.04.03, T. A. Keith, TK Gristmill Software, Overland Park KS, USA.

136. T. Ziegler and A. Rauk, *Theor. Chim. Acta*, 1977, **46**, 1.

137. T. Ziegler and A. Rauk, *Inorg. Chem.*, 1979, **18**, 1558.

138. T. Ziegler and A. Rauk, *Inorg. Chem.*, 1979, **18**, 1755.

139. T. Ziegler, Rauk A., in *Rev. comput. Chem.*, ed. K. B. Lipkowitz, Boyd, D. B., Wiley, New York, 2000, vol. 15, pp. 1.

140. G. E. Gadd, R. K. Upmacis, M. Poliakoff and J. J. Turner, *J. Am. Chem. Soc.*, 1986, **108**, 2547.

141. R. K. Upmacis, M. Poliakoff and J. J. Turner, *J. Am. Chem. Soc.*, 1986, **108**, 3645.

142. B. P. Stoicheff, *Can. J. Phys.*, 1957, **35**, 730.

143. C. F. Matta and R. J. Boyd, eds., *The Quantum Theory of Atoms In Molecules*, WILEY-VCH, Weinheim, 2007.

144. B. A. Dolgoplosk, E. I. Tinyakova, S. I. Beilin, G. N. Bondarenko, O. P. Parenago, N. N. Stefanovskaya, V. M. Frolov, O. K. Sharaev and V. A. Yakovlev, *Bulletin of the Academy of Sciences of the Ussr Division of Chemical Science*, 1977, **26**, 2315.

145. G. Wilke, M. Kroner and Bogdanov.B, *Angew. Chem.-Int. Edit.*, 1961, **73**, 755.

146. T. Tsuda, K. Watanabe, K. Miyata, H. Yamamoto and T. Saegusa, *Inorg. Chem.*, 1981, **20**, 2728.

147. M. F. Lappert and R. Pearce, *J. Chem. Soc.-Chem. Commun.*, 1973, 24.